Florida State University

College of Arts and Science

Investigation into Numerical Models of New High Temperature Superconductors

Kenneth Chad Sockwell

A Thesis submitted to the
Department of Scientific Computing
in partial fulfillment of the requirements for graduation with
Honors in the Major

Degree Awarded: Fall 2015

The members of the Defense Committee approve the thesis of Kenneth Chad Sockwell defended on April 24, 2015.

Dr. Max Gunzburger
Co-Thesis Director

Dr. Janet Peterson
Co-Thesis Director

Dr. Susan Blessing
Outside Committee Member

Declaration of Authorship

I, Kenneth Chad Sockwell, declare that this thesis titled, 'Investigation into Numerical Models of New High Temperature Superconductors ' and the work presented in it are my own. I confirm that:

- This work was done wholly or mainly while in candidature for a research degree at this University.
- Where any part of this thesis has previously been submitted for a degree or any other qualification at this University or any other institution, this has been clearly stated.
- Where I have consulted the published work of others, this is always clearly attributed.
- Where I have quoted from the work of others, the source is always given. With the exception of such quotations, this thesis is entirely my own work.
- I have acknowledged all main sources of help.
- Where the thesis is based on work done by myself jointly with others, I have made clear exactly what was done by others and what I have contributed myself.

Signed: _____

Date: _____

FLORIDA STATE UNIVERSITY

Department of Scientific Computing

Honor's Thesis

Investigation into Numerical Models of New High Temperature Superconductors

by Kenneth Chad Sockwell

Abstract

Recent discoveries of new high temperature superconductors initiated investigations to harness these new materials' properties. Unfortunately, many new high temperature superconductors come with odd properties such as multi-band interactions and anisotropic behavior, as is the case for Magnesium Diboride. In this research, Ginzburg Landau model variants are modified to try to simulate these materials more realistically at a mesoscopic scale. In particular an Anisotropic Two-Band Time Dependent Ginzburg Landau with inter-band coupling effects is formed to describe Magnesium Diboride. The influence of the coupling parameter η on the critical current is also investigated using a series of numerical studies.

Acknowledgements

I would like to acknowledge and thank my co-advisors Dr. Peterson and Dr. Gunzburger. You both have helped me greatly in starting my career in research and giving me the confidence to be successful. Thank you for the hours of insightful discussion, guidance through my research, the hours spent reviewing my work, and teaching me how to become a success in academia. Thank you, Dr. Burkardt for helping me in all my programming endeavors, and for always having the time to sit down with me and throughly explain things that I couldn't understand myself. I would also like to thank Dr. Blessing for teaching me the values of hard work and justifying that hard work with public presentation. Finally I would like to think my family for lovingly supporting me through school.

Contents

List of Figures

List of Tables

Abbreviations

FEM	Finite Element Methed
GL	Ginzburg Landau
TDGL	Time Dependent Ginzburg Landau
2BTDGL	Two Band Time Dependent Ginzburg Landau

Dedicated to Mom and Phil

Chapter 1

Superconductivity

1.1 Introduction

Superconductivity has sparked great interest in the study of physics over the last century. Many great scientists have pondered on how to understand this interesting phenomenon, as well as harness it. Superconductivity is a state in which a conductor has zero electrical resistance and exhibits the Meissner effect. This amazing property opened a new door for physics when it was discovered in 1911[1]. A material with zero electrical resistance can carry energy much more efficiently than a conventional conductor, due to the near disappearance of joule heating. This property of zero resistance also leads to some interesting magnetic properties. A material in the superconducting state while in a magnetic field completely expels any field lines from penetrating the sample. Thus superconductors also possess perfect diamagnetism, known as the Meissner Effect.

There is actually a division amongst superconducting materials in regard to the Meissner effect, Type I and Type II superconductors. If the magnetic field surrounding a superconductor reaches a critical strength, the superconductor generally exhibits one of two behaviors. Type I superconductors completely lose their superconducting properties once this magnetic strength is reached, returning to the normal state of the material. On the other hand, Type II superconductors remain in the superconducting state but are penetrated by magnetic flux vortices, slightly reducing the superconducting current in the material. There is a second, stronger critical magnetic field strength that returns Type II superconductors to their normal or non-superconducting state. Unfortunately, these properties generally only exist when a substance is cooled near absolute zero. Once the temperature in the sample reaches a critical temperature, the sample loses its superconducting properties. More recently, high temperature superconductors have been discovered that may lead to more feasible technology using superconductors,

taking advantage of their powerful properties.

Many models have been derived to understand superconductivity in hopes to harness it as well as discover new physics. One of these models, the BCS model, is derived from the microscopic effects of coupled electrons or Cooper pairs. Another model, the Ginzburg-Landau model, is a mesoscopic model and has the same scale resolution as the magnetic vortices in Type II superconductors. The Ginzburg-Landau model possesses the correct scaling to model such magnetic properties. The Ginzburg-Landau theory was developed by Ginzburg and Landau between the years of 1937 and 1950 [2] and verified by Gor'kov in 1959[3].

Numerical studies of the Ginzburg-Landau model have been done over the last few decades. Generally these numerical studies are aimed at studying the nucleation and behaviors of the magnetic vortices in Type II superconductors. Du *et al*. were some of the first to do numerical simulations of the Ginzburg-Landau model using the Finite Elements Method [4, 5]. They first proved the existence and uniqueness of an approximate solution of the Ginzburg-Landau equations, then computed numerical simulation of superconducting samples. Many scientists and mathematicians have extended the Ginzburg-Landau model to handle more complex situations, such as time dependence [6, 7], anisotropy [8, 9], normal inclusions [8, 10], non-isothermal model[11, 12], random thermal fluctuations [8, 13], and since the discovery of new Two Band superconductors, a two band Ginzburg-Landau model [14].

Repetitious discoveries of new high temperature superconductors have sparked a keen interest in the subject. Higher temperature superconductors make superconducting technology much more feasible. This is because low temperature superconductors need to be cooled by expensive liquid helium to keep the sample super cooled. Some of there new high temperature superconductors can be supercooled with much less expensive substances, such as liquid nitrogen. Unfortunately, these new high temperature superconductors typically come with odd properties, such as having two superconducting electron bands. Extensive numerical simulations using two band GL models, have not been published yet. These new models can capture the physics of new high temperature superconductors that the original model is not able to capture. Modeling these high temperature superconductors is the key to exploiting their miraculous properties and engineering new, more efficient technology.

1.1.1 Superconductivity and Its Mathematical Description

Superconductivity was first discovered in 1911 by H. Karmerlingh Onnes, a Dutch physicist. Onnes was investigating the properties of Mercury near absolute zero temperature, when he found some of these super cooled materials lost all electrical resistance when a

current was applied. Onnes noticed this behavior only exhibited itself when the sample was cooled below a material-dependent temperature, which he called the critical temperature, T_c [1]. Several compounds, ranging from simple metals to complex metallic and semi-metallic materials exhibit superconducting properties, but only at very low temperatures relative to ambient temperature around us. Some examples of superconducting compounds with low critical temperatures are aluminum with T_c= 1.175 K , lead with T_c= 7.196 K, and with high critical temperatures such as magnesium diboride with T_c = 39.0 K, and the complex compound Cs_2RbC_{60} with T_c= 33.0 K [1].

Superconductors also have a peculiar behavior when placed or supercooled in a magnetic field. A superconductor's critical temperature is lowered when placed in a magnetic field and it continues to decrease as the magnetic field strength rises. At some point the strength of the magnetic field completely destroys the superconducting properties in the sample. Each superconductor also has a critical magnetic field strength, H_c that interrupts superconductivity. Another interesting magnetic property of superconductors is the Meissner Effect. The Meissner effect was first discovered by H.W. Meissner and R. Ochsenfeld [15] and it is the Meissner effect that actually classifies a material as a superconductor [1]. When a material in the superconducting state is placed in a magnetic field, it completely cancels the magnetic field lines within the material of the surface. If the strength of the magnetic field rises above the critical magnetic field strength, H_c, then the magnetic field penetrates the sample and it returns to its normal state.

As mentioned above, there is a division amongst superconductors concerning the Meissner effect. Type I superconductors exhibit the Meissner effect fully, returning to their normal material state once $H > H_c$. Type II superconductors have two critical temperatures, H_{c1} and H_{c2}. The Type II superconducting sample expels the magnetic field from within its interior when $H < H_{c1}$. When $H > H_{c1}$ and $H < H_{c2}$, the sample is penetrated by magnetic flux tubes, or vortices. The sample material is in the normal state at the center of the vortices while the surrounding material continues to be in a superconducting state. When $H > H_{c2}$ then the sample completely returns to the normal state like the Type I superconductor. When a superconductor experiences the full Meissner effect it is in a state of perfect diamagnetism.

These new, mysterious properties sparked a keen interest in physicists and mathematicians. Since the discovery of the superconductivity, scientists have tried to capture this phenomenon using mathematical descriptions. One of the first models to do this was the London Theory, derived in 1935 by H. London and F. London as shown in [2]. The London brothers based their theory explaining the Meissner Effect in terms of Maxwell system on the boundary of the superconductor with a constant temperature under T_c. They proposed that the superconductor contained a supercurrent, $\boldsymbol{j}_s$, which flows without a potential difference being applied to the superconductor. The

supercurrent is related to the magnetic field strength $|\mathbf{H}|$, by:

$$\nabla \times \mathbf{H} = \frac{4\pi}{c}\boldsymbol{j}_s, \tag{1.1}$$

where c is the speed of light. The supercurrent can written in terms of the electron velocity $\boldsymbol{v(r)}$, the electron charge e, and the number of superconducting electrons per unit volume, n_e :

$$n_e e\boldsymbol{v(r)} = \boldsymbol{j}_s\boldsymbol{(r)} \tag{1.2}$$

From this the kinetic energy, E_K, of the current was shown to be:

$$E_K = \frac{1}{2}\int_\Omega m_s n_e |\boldsymbol{v(r)}|^2 d\boldsymbol{r} = \frac{1}{8\pi}\int_\Omega \lambda_L^2 |\nabla \times \mathbf{H}|^2 d\boldsymbol{r} \qquad \Omega \subset \mathbb{R}^3, \tag{1.3}$$

where m_e is the effective mass of the electron, and λ_L is the penetration depth, defined as

$$\lambda_L = \sqrt{\frac{m_s c^2}{4\pi n_e e}}. \tag{1.4}$$

The magnetic energy of the superconductor, E_M, is

$$E_M = \int_\Omega \frac{H^2}{8\pi} d\mathbf{r}\,. \tag{1.5}$$

From the kinetic and magnetic energies, the Londons constructed the free energy, F, of the superconducting system:

$$F = F_r + E_K + E_M, \tag{1.6}$$

where F_r is the energy of the electrons at rest in the system. Using the previous definitions of E_M and E_K leads to

$$F = F_r + \frac{1}{8\pi}\int_\Omega (H^2 + \lambda_L^2 |\nabla \times \mathbf{H}|^2)\, d\mathbf{r}\,. \tag{1.7}$$

Assuming F_r to be constant, then the free energy F, is minimized to satisfy the principle of least action. The minimizers of the free equation must satisfy:

$$\boldsymbol{H} + \lambda_L^2 \nabla \times \nabla \times \boldsymbol{H} = 0\,. \tag{1.8}$$

This is known as the London equation. Another important characteristic of the London Theory is the coherence length ξ_0. When E_K was formed for the free energy equation, it was assumed that $\boldsymbol{v(r)}$ varied slowly. This can be quantified as $\lambda_L \gg \xi_0$, where the coherence length, ξ_0, is the range of the correlation between electrons and is defined as

being of the order of:

$$\frac{\hbar v_f}{k_B T_0},$$

where $\hbar$ is the Plank constant, k_B is the Boltzmann constant, v_f the Fermi velocity. The London penetration depth, λ_L, and the coherence length, ξ_0, of an particular superconducting material can be used to redefine the previous Type I and Type II super conductors. When a superconducting material's penetration depth and coherence length satisfy $\lambda_L \ll \xi_0$ the superconductor is a Type I superconductor. If $\lambda_L \gg \xi_0$ for a superconducting material, then it is a Type II superconductor.

Soon after the London theory was formed, Landau formed a general second order phase transition theory [2]. This theory is based on the assumption that there was a complex order parameter, ψ that goes to zero as the phase transition happens. Then the free energy density can be expanded in terms of ψ, with coefficients that are functions of temperature T. The Helmholtz free energy,F, expanded in terms of constant ψ over volume Ω (in 3D, for 2D Ω is a surface) is then:

$$F = \int_\Omega f_n + \alpha(T)|\psi|^2 + \frac{\beta(T)}{2}|\psi|^4 + \dots, \tag{1.9}$$

where f_n is the free energy state of the normal state. Landau's general phase theory was only valid for temperatures near a critical value T_c, with values below T_c being correlated to the superconducting state. This lead to the coefficients being approximated as :

$$\alpha(T) \approx (T - T_c)\alpha_1 \qquad \beta(T) \approx \beta_0 \tag{1.10}$$

with $\alpha_1 > 0$ and $\beta_0 > 0$, both constant. In the context of superconductivity, $|\psi|^2$ is interpreted as the density of superconducting electrons in the sample. $|\psi|^2$ tends to 0 if $T > T_c$, corresponding to the normal state and it tends to -$\frac{\alpha}{\beta}$ if $T < T_c$, corresponding to the superconducting state. The next great stride in the understanding of superconductivity was when Landau and Ginzburg used Landau's general phase transition theory to model a superconductor in a magnetic field.

1.1.2 The Ginzburg-Landau Theory and its Verification

Landau and Ginzburg proposed a new phenomenological theory to describe superconductors in the presence of a magnetic field, 1950 [2]. They created a new Gibbs energy functional, $G(\psi, \mathbf{A})$, defined, in two dimensions as:

$$G(\psi, \mathbf{A}) = F_n + \int_\Omega \alpha|\psi|^2 + \frac{\beta}{2}|\psi|^4 + \frac{1}{2m_s}|(-i\hbar\nabla - \frac{e_s\mathbf{A}}{c})\psi|^2 + \frac{1}{8\pi}|\nabla\times\mathbf{A} - \mathbf{H}_e|^2 dV \tag{1.11}$$

$\mathbf{H}_e$ is the applied field, and ψ no longer needs to remain constant. m_s and e_s are the effective electron mass and charge respectively. F_n is the free energy of the normal state, and $\mathbf{A}$, is the vector potential defined as,

$$\mathbf{H} = \nabla \times \mathbf{A}\,. \tag{1.12}$$

Next calculus of variations was used to find the first order variation in the Gibbs energy functional. The resulting Euler-Lagrange equations are known as the Ginzburg-Landau equations or GL equations for short. The GL equations below are a coupled nonlinear, system of partial differential equations[2]:

$$\alpha\psi + \beta|\psi|^2\psi + \frac{1}{2m_s}(-i\hbar\nabla - \frac{e_s\mathbf{A}}{c})^2\psi = 0, \;\; \text{in} \;\; \Omega \tag{1.13}$$

$$\frac{\boldsymbol{j}_s}{c} = \frac{1}{4\pi}\nabla \times (\nabla \times \mathbf{A} - \mathbf{H}_e) = \frac{e\hbar}{2im_sc}(\psi^*\nabla\psi - \psi\nabla\psi^*) - \frac{e_s^2}{m_sc^2}|\psi|^2\mathbf{A}, \;\; \text{in} \;\; \Omega \tag{1.14}$$

with the boundary conditions

$$(-i\hbar\nabla - \frac{e_s}{c}\mathbf{A})\psi \cdot \mathbf{n} = 0, \;\; \text{on} \;\; \partial\Omega$$

$$(\nabla \times \mathbf{A} - H_e) \times \mathbf{n} = 0, \;\; \text{on} \;\; \partial\Omega\,.$$

where $\mathbf{n}$ is normal vector to the boundary. There are two important characteristic lengths in the Ginzburg-Landau model, similar to those in the London model of superconductivity. The spatial penetration depth $\lambda(T)$, a temperature dependent function, characterizes a superconducting material by specifying how deep a magnetic field can penetrate the surface of the superconducting sample. The second, the coherence length, $\xi(T)$, specifies the spatial width of the transition layer between the normal and superconducting regions. This length describes the distance over which ψ can change by a noticeable amount [8]. The ratio of these lengths, κ, is the Ginzburg-Landau constant:

$$\lambda = (-\frac{m_s\beta c^2}{4\pi\alpha e_s^2})^{\frac{1}{2}} \tag{1.15}$$

$$\xi = (-\frac{\hbar^2}{2m_s\alpha})^{\frac{1}{2}} \tag{1.16}$$

$$\kappa = \frac{\lambda}{\xi}\,. \tag{1.17}$$

Once the phenomenological GL theory was developed, a microscopic theory describing superconductivity was needed to verify it [2]. In 1957 a new microscopic theory,

the BCS theory was just what was needed [16]. The BCS theory, named after its discoverers (Bardeen, Cooper, and Schrieffer), describes superconductivity as a byproduct of lattice vibrations at low temperatures. When a metal is supercooled, much of its thermal activity ceases. The BCS theory claims that when electrons pass through this supercooled conductor, not only do random collisions between the lattice and electrons stop, but the electrons form *Cooper pairs* due to precise lattice vibrations. Electrons pairing seems counter intuitive, but this pairing is driven by the positively charged lattice choreographing the electron pairs. The electrons are coupled in the energetically favorable Cooper pair, the combined spin of the coupled system is zero. This allows the Cooper pairs to not be bound by the Pauli exclusion principle. All the electrons forming Cooper pairs can be in same quantum state, allowing them to flow with zero resistance in a correlated manner. When $T > T_c$ or $H > H_c$, the Cooper pairs are broken and the material is no longer a superconductor. In 1959, Gor'kov proved the Ginzburg-Landau theory was a limiting case of the BCS theory [2] . Furthermore, Gor'kov and Eliashberg extended the GL model to an evolutionary time dependent model in 1968 [2]. Gor'kov and Eliashberg proposed that if a superconductor was driven from equilibrium, the relaxation back to equilibrium can be described as [14]

$$\Gamma(\frac{\partial \psi}{\partial t} + \frac{ie}{\hbar}\Phi\psi) = -\frac{\delta G}{\delta \psi *}, \tag{1.18}$$

$$\boldsymbol{j} = j_n + j_s = \sigma_n(-\frac{1}{c}\frac{\partial A}{\partial t} - \nabla\Phi) - c\frac{\partial F_s}{\partial A}, \tag{1.19}$$

where Γ is a damping constant, σ is the conductivity in the normal state, and Φ is the potential difference of the system, G is the Gibbs free Energy and F_s is the portion of the Gibbs free energy that does not contain the magnetic field strength terms, defined as,

$$F_s = \int_\Omega f_n + \alpha|\psi|^2 + \frac{\beta}{2}|\psi|^4 + \frac{1}{2m_s}|(-i\hbar\nabla - \frac{e_s\mathbf{A}}{c})\psi|^2 \, d\Omega \, . \tag{1.20}$$

From this the minimizers of the system are found using calculus of variations. The minimizers are the Euler Lagrange equations that become the time dependent Ginzburg-Landau equations:

$$\Gamma(\frac{\partial \psi}{\partial t} + \frac{ie}{\hbar}\phi\psi) + \alpha\psi + \beta|\psi|^2\psi + \frac{1}{2m_s}(-i\hbar\nabla - \frac{e_s\mathbf{A}}{c})^2\psi = 0, \text{ on } \Omega \text{ and } \forall t \tag{1.21}$$

$$\boldsymbol{j} = \frac{1}{4\pi}\nabla\times(\nabla\times\mathbf{A}-\mathbf{H}) = \sigma_n(-\frac{1}{c}\frac{\partial \mathbf{A}}{\partial t} - \nabla\phi) + \frac{e_s\hbar}{im_s}(\psi^*\nabla\psi - \psi\nabla\psi^*) - \frac{4e_s^2}{m_s c}|\psi|^2\mathbf{A}, \text{ on } \Omega \text{ and } \forall t \tag{1.22}$$

with boundary conditions and initial conditions:

$$(-i\hbar\nabla - \frac{e_s}{c}\mathbf{A})\psi \cdot \mathbf{n} = 0, \text{ in } \partial\Omega \text{ and } \forall t$$

$$(\nabla \times \mathbf{A} - H_e) \times \mathbf{n} = 0, \text{ in } \partial\Omega \text{ and } \forall t$$

$$\psi(x, 0) = \psi_0(x), \text{ in } \Omega$$

$$\mathbf{A}(x, 0) = \mathbf{A}_0(x), \text{ in } \Omega$$

The time dependent Ginzburg-Landau model opened a new dimension in the study of superconductivity. The time dependent model allows one to look at the formation of magnetic vortices in Type II superconductors as well as the dynamical motion of them. Applied current in the superconducting sample could also be modeled more realistically with the time dependent model, especially alternating current. The time dependent Ginzburg-Landau model laid a basis for future work in superconductivity. More recently many scientists have taken advantage of computers to solve the Ginzburg-Landau equations numerically.

1.2 Recent Research and Thesis Discussion

1.2.1 More Recent Research

In the last 20 years, much effort has gone into numerical models for superconductors. Computers have made these numerical calculations a more efficient venture than previous times. The Ginzburg-Landau equations are a coupled pair of nonlinear partial differential equations. Numerical methods such as finite elements method have been used to solve this system. Du *et al.* [4, 5] was one of the first to explore this area. In Du's work, the Ginzburg-Landau equations are first made suitable for the finite elements method. This was done by first non-dimensionalizing the equations along a length scale of ξ, the coherence length mentioned earlier. This non-dimensionalization is done to rescale the problem, for more uniform scaling between parameters. Also non-dimensionalizing the equations eliminates many of the parameters by combining them into new parameters, typically more convenient ones. The ξ length scale is chosen because this is the scale that ψ, the order parameter, changes over. Next the Ginzburg-Landau equations are made well-posed by using a gauge symmetry. This is essentially choosing a manner in which the variables of the system are represented in terms of each other, but is derived from physical symmetries. Typically the Coulomb or Zero Potential gauge is used to represent ϕ in terms of $\boldsymbol{A}$, while adjusting the boundary conditions to complete the gauge

transformation. Du proves the existence of the minimizer of the Ginzburg-Landau free energy functional, rigorously, in terms of Sobolev spaces. The Ginburg Landau equations are naturally gauged this way. Next the finite element approximations are shown to exist and the error bounds are found.

The next extension in the numerical simulations was [6] proving the global existence and uniqueness of the solutions of the time dependent Ginzburg-Landau equations. In [6] the magnetic vortices are modeled, but on a small sample with boundary-dominated effects. Du also modeled superconductivity for s-wave and d-wave superconductivity [17, 18]. S-wave superconductivity is where the superconducting electrons are in the s-orbitals. Similarly the d-wave superconductivity is when the superconducting electrons are in the d-orbitals. From this many variants of the Ginzburg-Landau model were made. Each model is specialized for a particular set of circumstances. Normal inclusions were modeled in [10], by placing impurities in the superconducting sample. This is done to study the pinning effects of vortices from the normal inclusions. A variable thickness model was derived in [19, 20]. This allows for the study of vortex dynamics in a sample with a variable thickness, which is a more realistic sample than a perfectly homogeneous sample. Applied current in the superconducting sample was studied in[8, 14]. A high κ model was made in [21, 22] which reduces the coupled pair of Ginzburg Luandau equations to one equation by expanding the functions ψ and $\boldsymbol{A}$ in terms of κ. This is much more computationally efficient when the particular material of interest has a high value of κ. Anisotropic models of the grain boundary and rotated crystal variety were studied in [9] and [8], respectively. Another anisotropic model is the Lawrence Doniach model [8, 23, 24] that is effective when the layer spacing is too large to accurately be modeled by the anisotropic GL model. Models pertaining to thermal effects have also been derived. In [11, 12], the temperature of the superconducting sample is posed as an unknowns function and solved for, while in [8, 13], the thermal variation is posed as a stochastic process and is modeled much like a random noise process. These models have also extended to three dimensions for results that can be directly compared to experiments,[8, 25].

All those models are great tools for their specified scope of interest but each has its own downfalls. Typically using only one of these models does not capture all of the physics going on in a superconductor. For instance, a model lacking any non-isothermal feature assumes the temperature is constant and very close to the critical temperature, T_c. This model disregards any thermal effect by-products of the dynamical motion of magnetic vortices and joule heating. The isothermal model of a superconductor can be correct if the superconductor is immersed in a thermal bath to keep its temperature constant, but this is more of an ideal situation than reality. Until recently computers were not powerful enough to realistically model a superconductor. At first, the samples

were small leading to boundary dominated effects. This means the full interaction of the magnetic vortices in superconductors could not be studied. Another issue is that most of the models were two dimensional. In certain situations this is acceptable, but reality is in three dimensions. Even in the cases where a three dimensional model was made, the samples were still very small due to the memory storage required. Today, computers are much more powerful and parallel computing is much easier to implement than in the past.

Another new study has come into play since the discovery of new high temperature superconductors. The new high temperature superconductors have very novel and interesting properties. Some of them are high temperature superconductors, making superconducting technology more feasible. Another great property is some of them are very inexpensive to make such as magnesium diboride and graphene, being much cheaper than their complex iron and copper superconducting counterparts. The down side to these high temperature superconductors is that the manner in which superconductivity exists in them is very different than conventional superconductors. Some of these materials can't be successfully explained by the BCS theory, yet phrenological theories like the multi-band GL can be fitted to experiments to handle such materials [26]. These high temperature superconductors carry odd properties such as multi band superconductivity combined with anisotropy and even mixed Type I and Type II states [27]. Chan was one of the first to put serious effort into numerical modeling of multi-band superconductors, particularly the Two Band Time Dependent Ginzburg-Landau model in [14]. He followed Du's numerical methods using the finite elements method. Chan studied the vortex dynamics of two band superconductors as well as applied current to the sample from direct and current sources. Chan's work gave great insight into the formation and dynamics of superconductors and their magnetic vortices, but was limited in some ways. The studies were only two dimensional and lack features that most high temperature superconductors contain. Some of the features are anisotropy, and new thermal effects from the two band interactions. Many two band superconducting materials contain these odd properties such as MgB_2 , $LuNi_2B_2C$, and YNi_2B_2C. Making new models that include these features as well as a three dimensional representation are critical in studying these new superconducting materials.

Chapter 2

The Finite Element Method

2.1 Finite Element Method Overview

The Finite Element Method, or FEM for short, is a numerical method used to solve partial differential equations. The method is based on the general approach of the Method of Weighted Residuals and has its roots in variational techniques. The method is similar to the finite difference method in that the domain is discretized into a set of nodes or points. However, the Finite difference method only provides a discrete solution at the nodes, unlike FEM, which can (but necessarily) generate a continuous solution. This is done by forming the weak from of the problem. The weak form is typically found by multiplying the equation by a test function from an infinite dimensional space V and then integrating over the spatial domain. Then the solution is approximated in some finite dimensional vector space $V^h \subset V$. To understand this approach consider the one dimensional Poisson's Equation as the prototype problem for simplicity.

$$-u''(x) = f(x) \quad in \quad 0 < x < 1 \tag{2.1}$$

with boundary conditions

$$u'(0) = 0, \quad u(1) = 0 \tag{2.2}$$

To obtain the continuous weak from the equation is then multiplied by a test function, $v(x)$ from the vector space V. Then the equation is integrated by parts. In this way the problem is solved in a weak sense because the solution to the original problem coincides with the solution to the weak problem and conversely if the solution is smooth enough. We have

$$-u''v = fv \tag{2.3}$$

$$-\int_0^1 u''v \, dx = \int_0^1 fv \, dx \tag{2.4}$$

$$-u'v|_0^1 + \int_0^1 u'v'\,dx = \int_0^1 fv\,dx \quad \forall\, v \in V \tag{2.5}$$

Yielding the standard weak problem. Seek $u \in V$, satisfying

$$\int_0^1 u'v'\,dx = u'v|_0^1 + \int_0^1 fv\,dx \quad \forall v \in V \tag{2.6}$$

Now the boundary conditions can be discussed. There are typically two types of boundary conditions used in the finite elements method, Dirichlet and Neumann boundary conditions. Dirichlet boundary conditions place conditions on constraints on the solution u on the boundary, while Neumann boundary conditions place constraints on the derivative of the solution u'. For this problem the Neumann boundary condition is known as natural boundary condition because it can be implemented naturally into Equation (2.6) through the boundary term. Dirichlet boundary conditions are known as essential boundary conditions because they must be enforced on the solution space. If the one dimensional Poisson's equation Equation (2.1), defined on the domain $a < x < b$, has Dirichlet and Neumann boundary conditions,

$$\begin{aligned} u'(0) &= 0 \\ u(1) &= 0 \end{aligned} \tag{2.7}$$

Then weak formulation of the problem becomes, seek $u \in V$

$$\int_0^1 u'v'\,dx = \int_1^0 fv\,dx \quad \forall v \in V \tag{2.8}$$

where V consists of all functions which are sufficiently smooth and are zero at $x = 1$.

2.1.1 Discretizing the Weak Form

Discretization of the weak from is necessary to solve the weak problem given in Equation (2.6). To do this, we choose a finite dimensional subspace $V^h \subset V$ and pose the weak problem over this subspace. Then the domain of interest, Ω, is discretized into a set of non overlapping intervals. For generality, let $(a < x < b) \in \Omega$ be the one dimensional domain, then it can discretized by a set of points $\{x_0, x_1, \cdots, x_{n+1}\}$, where $x_0 = a$ and $x_{n+1} = b$ and the largest interval is of length h. The discrete weak problem (DWP) is stated as, seek $u^h \in V^h$ such that

$$\int_a^b (u^h)'(v^h)'\,dx = \int_b^a fv^h\,dx \quad \forall v^h \in V^h \tag{2.9}$$

where the Dirichlet boundary condition is imposed on the discrete space V^h.

Now that the discretized grid has been made, a specific finite vector space, V^h can chosen. Typically V^h is chosen to be a subspace of continuous piecewise polynomials. For this simple example V^h is chosen to be a subspace of continuous piecewise linear polynomial functions. Consider the weak problem from Equation (2.6), but now with $u(0) = 1$ as the boundary condition on the right side. If the solution is of the form given in Figure 2.1, then an approximate solution in the space V^h is given by Figure 2.2.

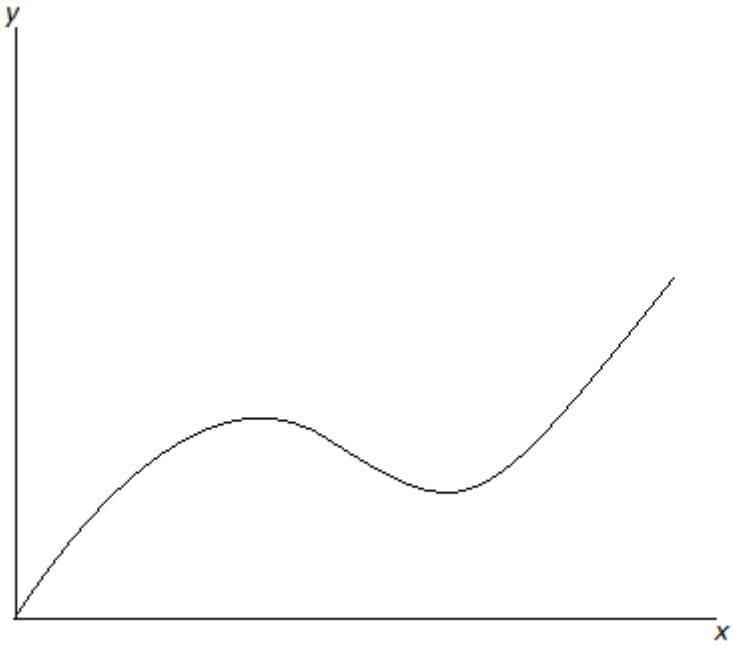

FIGURE 2.1: A general function $f(x)$

The basis is chosen to be piecewise linear polynomial "hat functions" that have the property $\phi_j(x_i) = \delta_{i,j}$. They are given explicitly by

$$\phi_i(x) = \begin{cases} \frac{x - x_{i-1}}{x_i - x_{i-1}} & : x_{i-1} < x < x_i \\ \frac{x_{i+1} - x}{x_{i+1} - x_i} & : x_i < x < x_{i+1} \\ 0 & : elsewhere \end{cases} \tag{2.10}$$

More generally for any set of nodal basis functions,

$$\phi_i(x_j) = \delta_{ij} \tag{2.11}$$

and function values in the intervals between the nodes depends on the specific species of basis function chosen. Returning to the simple example, a nodal basis function described

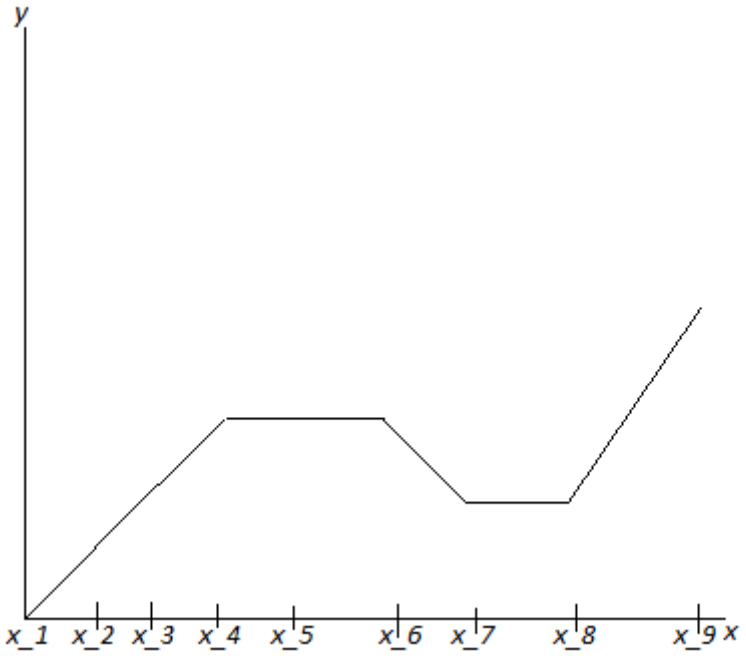

FIGURE 2.2: The function $f(x)$ is approximated in the discrete V^h using piecewise linear polynomials.

in Equation (2.10) can be seen in Figure 2.3 In the one dimensional case a homogeneous Dirichlet boundary condition at the endpoint does not have a basis function so that it has a value of 0 at the end point from the adjacent basis function. On the contrary, Neumann conditions constitute a basis function at the end point, making the problem larger.

Each interval $[x_i, x_{i+1}]$ containing one of more basis functions in its domain is known as a finite element or element for short. The geometry of the elements and the basis functions chosen for the domain are the key features of the finite element method. Continuing with the simple one dimensional example, the test function in Equation (2.10) can now be chosen to be one of the basis functions $\phi_i(x) \in V^h$. Testing against all $v^h \in V^h$ is equivalent to testing each basis function ϕ_i. Now the discrete weak problem (DWP) can be defined in terms of the basis functions given in Figure 2.3, yielding

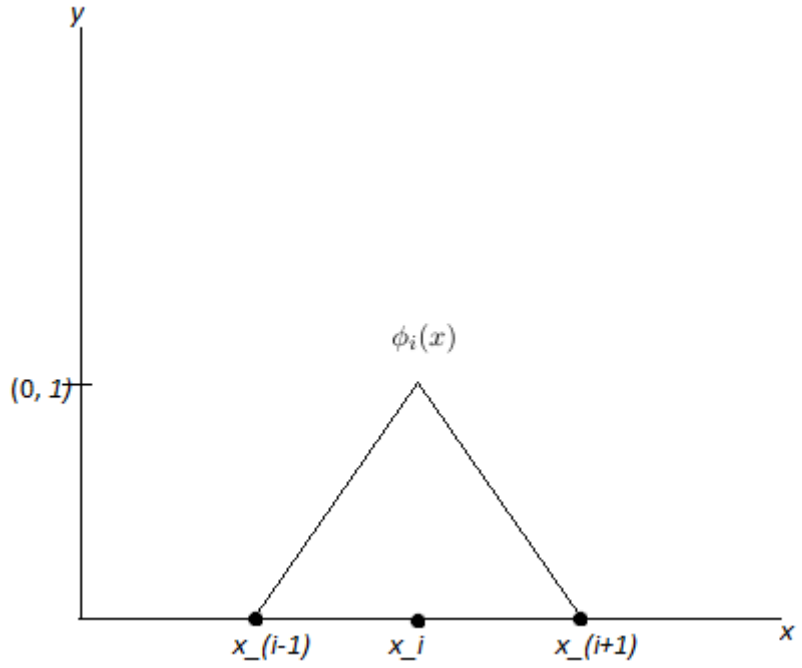

FIGURE 2.3: A linear piecewise polynomial defined on two intervals. The function is centered at x_i and is 1 at that node, while having 0 value at all other nodes. As each of the basis functions are defined, the linear functions will overlap across each interval. Each interior interval will have one linear function with negative slope and one positive linear function with positive slope defined on it.

the sequence of equations

$$\begin{aligned}
\int_a^{x_1} u^{h\prime}\phi_0'(x)\,dx &= \int_a^{x_1} f\phi_0(x)\,dx \\
\int_a^{x_2} u^{h\prime}\phi_1'(x)\,dx &= \int_a^{x_2} f\phi_1(x)\,dx \\
&\vdots \\
\int_{x_{i-1}}^{x_{i+1}} u^{h\prime}\phi_i'(x)\,dx &= \int_{x_{i-1}}^{x_{i+1}} f\phi_i(x)\,dx \\
&\vdots \\
\int_{x_{n-1}}^{b} u^{h\prime}\phi_n'(x)\,dx &= \int_{x_{n-1}}^{b} f\phi_n(x)\,dx
\end{aligned} \tag{2.12}$$

where the limits of the integrals represent where the test functions are nonzero at. Now that the weak form has be specified with a specific set of functions, the solution u can be expanded in the discrete space V^h as follows,

$$u^h = \sum_{j=0}^{n} c_j\phi_j(x) \tag{2.13}$$

and the sequence of equations in Equation 2.12 can be expanded as,

$$\begin{aligned}
\sum_{j=1}^{n} \int_a^{x_1} c_j \phi_j'(x)\phi_0'(x)\, dx &= \int_a^{x_1} f\phi_0(x)\, dx \\
\sum_{j=1}^{n} \int_a^{x_2} c_j \phi_j'(x)\phi_2'(x)\, dx &= \int_a^{x_2} f\phi_2(x)\, dx \\
&\vdots \\
\sum_{j=1}^{n} \int_{x_{i-1}}^{x_{i+1}} c_j \phi_j'(x)\phi_2'(x)\, dx &= \int_{x_{i-1}}^{x_{i+1}} f\phi_2(x)\, dx \\
&\vdots \\
\sum_{j=1}^{n} \int_{x_{n-1}}^{b} c_j \phi_j'(x)\phi_n'(x)\, dx &= \int_{x_{n-1}}^{b} f\phi_n n(x)\, dx
\end{aligned} \tag{2.14}$$

This system can be formed into a matrix equation, with a matrix of of $(n+1 \times n+1)$ entries. Since many of the ϕ_j basis functions will be zero on many of the intervals for ϕ_i, due to the relation given in Equation (2.11), the matrix will be sparse. The intervals where ϕ_i is non zero is known as the support for basis function, ϕ_i. In this case with linear piecewise polynomials, the matrix is tridiagonal. Also for the simple example of Poisson's equation, the resulting matrix is symmetric ($\mathbf{A}^T = \mathbf{A}$) and positive definite ($\mathbf{x}^T\mathbf{A}\mathbf{x} > 0 \;\; \forall \mathbf{x}$). The resulting matrix, $\mathbf{A}$, can be expressed as,

$$\begin{pmatrix}
\int_a^{x_1} \phi_0'(x)\phi_0'(x)\, dx & \int_a^{x_1} \phi_1'(x)\phi_0'(x)\, dx & 0 \cdots & 0 \\
\int_a^{x_2} \phi_0'(x)\phi_1'(x)\, dx & \int_a^{x_2} \phi_1'(x)\phi_1'(x)\, dx & \int_a^{x_2} \phi_3'(x)\phi_2'(x)\, dx \cdots & 0 \\
0 & \vdots & \ddots & \vdots \\
\vdots & & & \\
0 & \cdots & \int_{x_{n-1}}^{b} \phi_{n-1}'(x)\phi_n'(x)\, dx & \int_{x_{n-1}}^{b} \phi_n'(x)\phi_n'(x)\, dx
\end{pmatrix} \tag{2.15}$$

and the system can be expressed as,

$$\mathbf{A}\begin{pmatrix} c_1 \\ c_2 \\ \vdots \\ c_n \end{pmatrix} = \begin{pmatrix} \int_a^{x_1} f(x)\phi_1(x)dx \\ \int_{x_2}^{a} f(x)\phi_2(x)dx \\ \vdots \\ \int_{x_{n-1}}^{b} f(x)\phi_n(x)dx \end{pmatrix} \tag{2.16}$$

and the essential homogeneous Dirichlet boundary conditions have been enforced by V^h.

$$u(a) = u(b) = 0 \tag{2.17}$$

Now the coefficients, c_i can be solved for using a linear solver. The solution can be found

at any point using Equation (2.13). Since linear piecewise polynomials were used as the basis for the space V^h, the solution has non continuous first derivatives.

2.2 FEM in Two Dimensions and Higher order Basis Functions

In the last subsection the Finite Element Method was demonstrated using the one dimensional Poisson's equation. Now the method is generalized to 2 dimensions, as well as higher order polynomials. The two dimensional elliptical equation is now used for generality. Consider the following problem on $(0 < x < 1, 0 < y < 1) \in \Omega$:

$$\begin{aligned} -\Delta u(x,y) + u(x,y) &= f(x,y) \ \text{ in } \ \Omega \\ u(x,0) = u(x,1) &= 0 \\ u(0,y) &= 0 \\ u'(1,y) &= g(y) \end{aligned} \tag{2.18}$$

Now the weak must be found and the weak problem stated. Chose a space vector space V. Integrating and multiplying by a test function $v(x,y) \in V$,

$$\int_\Omega -v\Delta u + uv \; d\Omega = \int_\Omega fv \; d\Omega \tag{2.19}$$

Now the Laplacian operator is formed into two gradient operators using integration by parts (in higher dimensions is called Green's first identity). The following identity exemplifies this:

$$\int_\Omega \nabla \cdot (v\nabla u) \; d\Omega = \oint_{\partial\Omega} v\nabla u \cdot d\mathbf{S} \tag{2.20}$$

where the divergence theorem has been used to derive the relation and $d\mathbf{S} = \mathbf{n}dS$. Distributing the divergence operator,

$$\int_\Omega (v\Delta u + \nabla v \cdot \nabla u) \; d\Omega = \oint_{\partial\Omega} v\nabla u \cdot d\mathbf{S} \tag{2.21}$$

Finally, the following relation can used to pose the problem in the weak form,

$$-\int_\Omega (v\Delta u) \; d\Omega = \int_\Omega (\nabla v \cdot \nabla u) \; d\Omega - \oint_{\partial\Omega} v\nabla u \cdot d\mathbf{S} \; . \tag{2.22}$$

Yielding

$$\int_\Omega (\nabla v \cdot \nabla u) + uv \; d\Omega = \int_\Omega fv \; d\Omega + \oint_{\partial\Omega} v\frac{\partial u}{\partial n} \; dS \tag{2.23}$$

where

$$\frac{\partial u}{\partial n} = \nabla u \cdot \mathbf{n} \tag{2.24}$$

Now the natural Neumann boundary conditions can be implemented. The Dirichlet Boundary conditions place a constraint on the space V. The weak from is show below and the weak problem is stated as seek $u \in V$ such that

$$\int_\Omega (\nabla v \cdot \nabla u) + uv \; d\Omega = \int_\Omega fv \; d\Omega + \int_0^1 vg(y)dy \quad \forall v \in V \tag{2.25}$$

The discretized weak problem found by choosing a discrete space $V^h \in V$. The discretized weak problem is stated as seek $u^h \in V^h$, such that

$$\int_\Omega (\nabla v^h \cdot \nabla u^h) + u^h v^h \; d\Omega = \int_\Omega f v^h \; d\Omega + \int_0^1 v^h g(y)dy \quad \forall v^h \in V^h \tag{2.26}$$

Now the geometry can discretized and the discrete space V^h chosen

Now that the problem is stated in two dimensions, the geometry becomes more complicated. There are several choices in how to discretize the domain instead of simple intervals as in the last example. The most reasonable choices for discretization of the square domain Ω are rectangles or triangles. The discretization using squares is intuitive, while the triangles are arranged in opposite orientations to make squares to cover to domain. Figure 2.4 show the simple discretization of Ω using triangles. More complicated domains can be covered with an arrangement of different sized and oriented triangles to ensure the domain is completely covered.

Now the domain has been discretized into smaller domains called elements, the discrete space V^h is chosen. We can choose it to be a space of piecewise polynomials defined on the elements by basis functions.Typically when the domain is discretized, it is done by choosing a set of finite elements. The specific basis functions chosen dictates how many nodes each element will have. For instance, when using linear basis functions on triangular elements, each triangle will have three nodes, because a linear function on a triangle is uniquely determined by the value at three nodes. The linear basis functions have the form,

$$\phi(x, y) = m_1 y + m_2 x + c_0 \tag{2.27}$$

This gives matrix entries of the form

$$\int_{Eij} (\nabla \phi_i \cdot \nabla \phi_j + \phi_i \phi_j) \; dE_{ij} = \int_{Eij} f\phi_i \; dE_{ij} + \int_{Lij} \phi_i g(y)dy \tag{2.28}$$

where each integral spans the domain of support, E for each basis functions, and L the interval of support for the boundary. As before we require $\phi_i(x_j, y_j) = \delta_{i,j}$.Now each basis function is defined at one node and goes to zero at the other two nodes. In

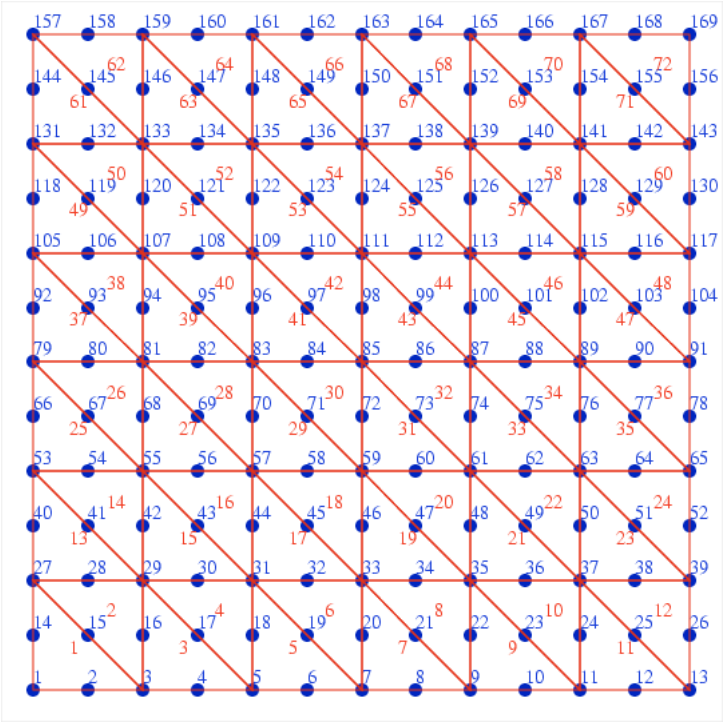

FIGURE 2.4: A square domain made into a grid and triangulated. This grid is for quadratic basis functions as opposed to linear. This is why each triangle has six nodes.The blue numbers are node numbers and the red numbers are the element number.

the situation where square elements are used, there are four nodes and bilinear basis functions are used to accommodate the fourth node. The bilinear basis functions are products on the one dimensional basis function and are of the form.

$$\phi(x, y) = m_1 y + m_2 x + m_3 xy + c_0 \tag{2.29}$$

For the discretized weak form of Equation (2.18) is shown in (2.26), triangular elements with quadratic basis function will be used. The quadratic basis functions require that the each element has six nodes, three on each side of the triangle. A pattern can be seen as the basis function order grows. There must be enough points on triangle to uniquely determine the basis functions in each direction. Thus for cubic polynomials there must be ten nodes and ten basis functions for completeness. However, this does not put a limit on the number of nodes used. More exotic elements can used that have extra nodes that place constraints on the derivatives. The basis functions used for the current example are of the form:

$$\phi_i(x, y) = m_1 x^2 + m_2 y^2 + m_3 xy + m_4 x + m_5 y + c_0 \tag{2.30}$$

where ϕ_i is one at is 1 at node i corresponding to (x_i, y_i). The quadratic basis functions can be seen in Figures 2.5,2.6, and all together in Figure 2.6. They are defined on the

unit triangle as,

$$\begin{aligned}
\phi_1(\xi,\eta) &= 2(1-\xi-\eta)(\frac{1}{2}-\xi-\eta) \\
\phi_2(\xi,\eta) &= 2\xi(\xi-\frac{1}{2}) \\
\phi_3(\xi,\eta) &= 2\eta(\eta-\frac{1}{2}) \\
\phi_4(\xi,\eta) &= 4\xi(1-\xi-\eta) \\
\phi_5(\xi,\eta) &= 4\xi\eta \\
\phi_6(\xi,\eta) &= 4\eta(1-\xi-\eta)
\end{aligned} \tag{2.31}$$

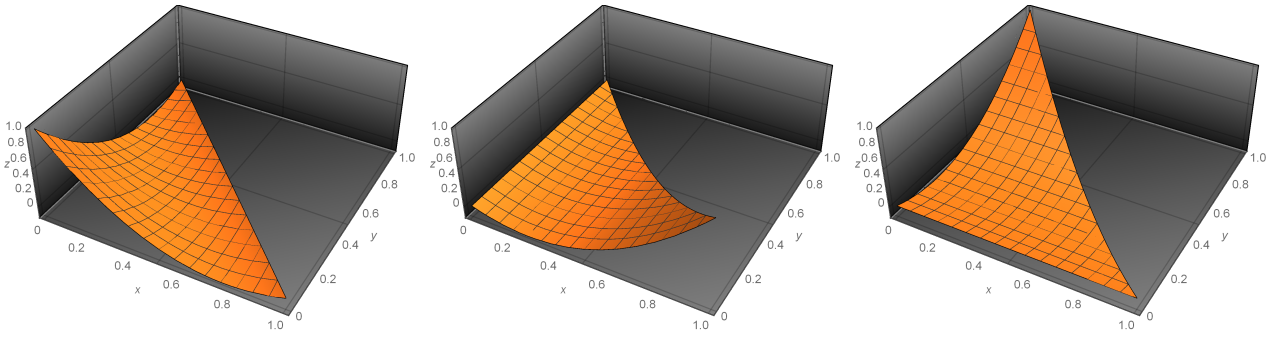

FIGURE 2.5: These are the three basis functions defined on the vertices nodes of the unit triangle

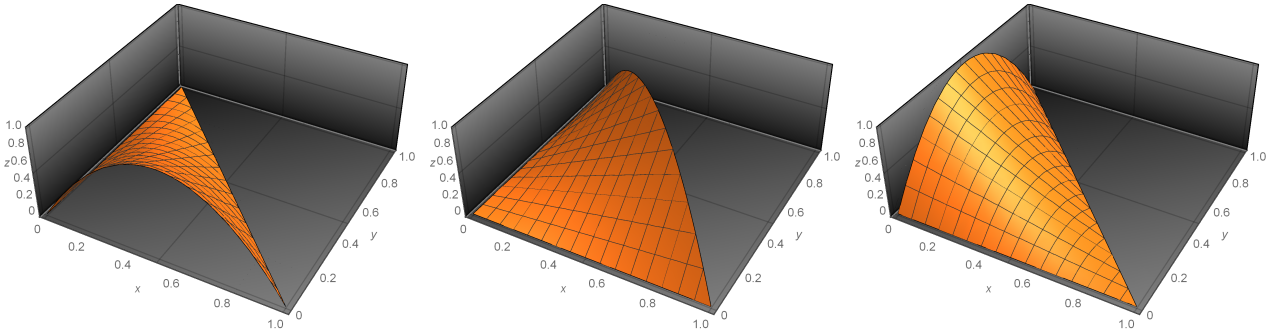

FIGURE 2.6: These are the three basis functions defined on the midpoint nodes of the unit triangle

2.2.1 Implementing FEM in two dimensions

Now that the general overview for the two dimensional FEM has been seen, some specific implementations can be shown. For the example shown in Equation (2.26), the discrete space V^h is chosen to be the space of piecewise quadratic functions $\mathbb{P}_h^2$. Previously the accuracy of the FEM has not been mentioned. To increases the accuracy the element size is reduced, giving a finer mesh, or the order of polynomial is increased to increase the resolution. The first method is known as the h-method and the second is known

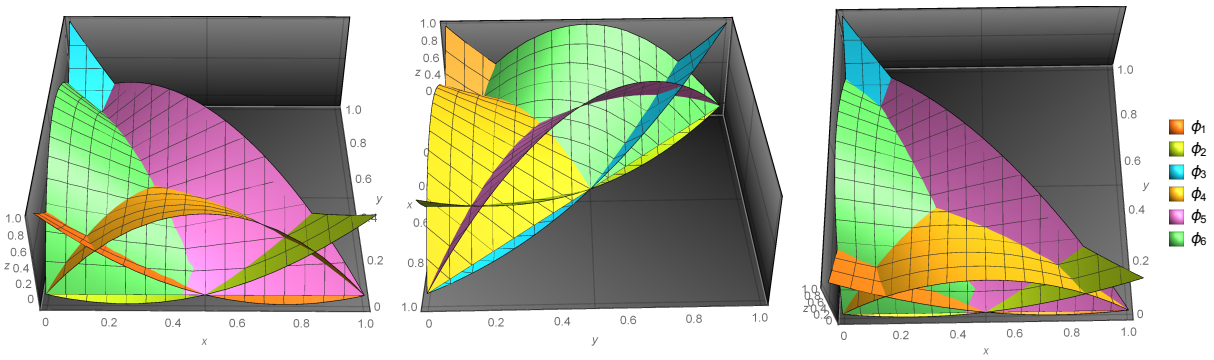

FIGURE 2.7: These are three views of all the basis functions defined on the unit triangle.

as the p-method. A third method that increases the polynomial power and reduces the mesh size is the hp-method. The accuracy is examined more closely later in the Errors Section. Once a sufficient mesh discretization has been chosen, Equation 2.32 can be used to produce a matrix equation. In standard FEM terms, the matrix containing the gradient terms is know as the stiffness matrix $\mathbf{K}$, the matrix containing the $\phi_i\phi_j$ terms is known as the mass matrix,$\mathbf{M}$, and the right hand side is known at the load vector, $\mathbf{L}$.

$$\begin{gathered}\int_{Eij}[(\nabla\phi_i\cdot\nabla\phi_j)+\phi_i\phi_j]\,dE_{ij}=\int_{Eij}f\phi_i\,dE_{ij}+\int_{Lij}\phi_i g(y)dy\\ \Updownarrow\\ \mathbf{K}+\mathbf{M}=\mathbf{L}\end{gathered}\tag{2.32}$$

These structural terms are from the engineering background the FEM comes from. As previously mentioned each matrix entries' integrals are evaluated in the domain of support. Each integral can be evaluated using an appropriate quadrature rule. Now the basis functions need to be defined within each element. They can be defined using Lagrange interpolating polynomials as in the one dimensional case, but this is rather cumbersome for a large domain and alternating triangles. Instead a symmetry can be seen amongst the basis functions belonging to each element. This symmetry can be exemplified using a standard reference triangle with standard basis functions defined on $(0<\xi<1, 0<\eta<1)$, as seen in Figure 2.8.

Now the basis functions can derived on the reference element in a simple manner and mapped, using barycentric coordinates, to the physical element shown in Figure 2.9.

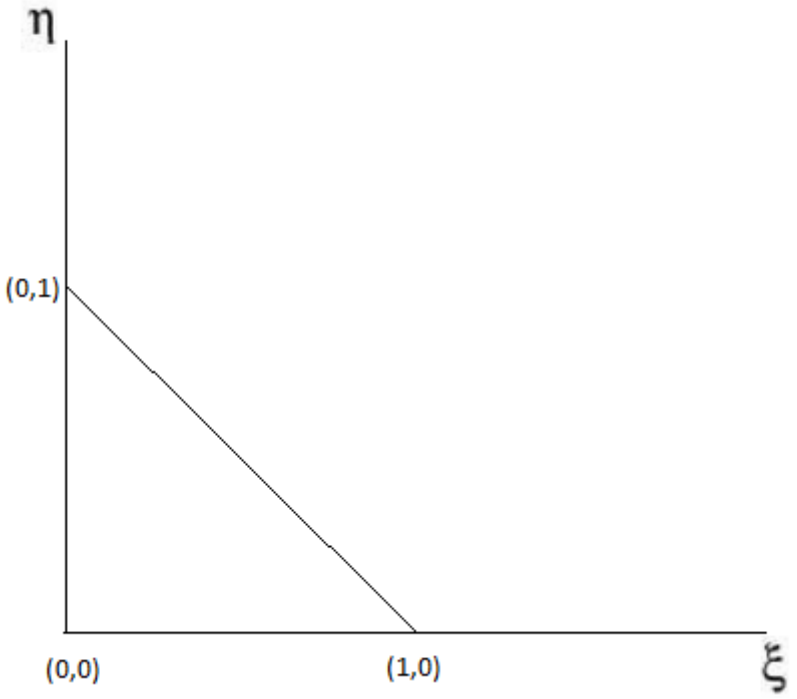

FIGURE 2.8: The reference triangle defined on $0 < x < 1, 0 < y < 1$

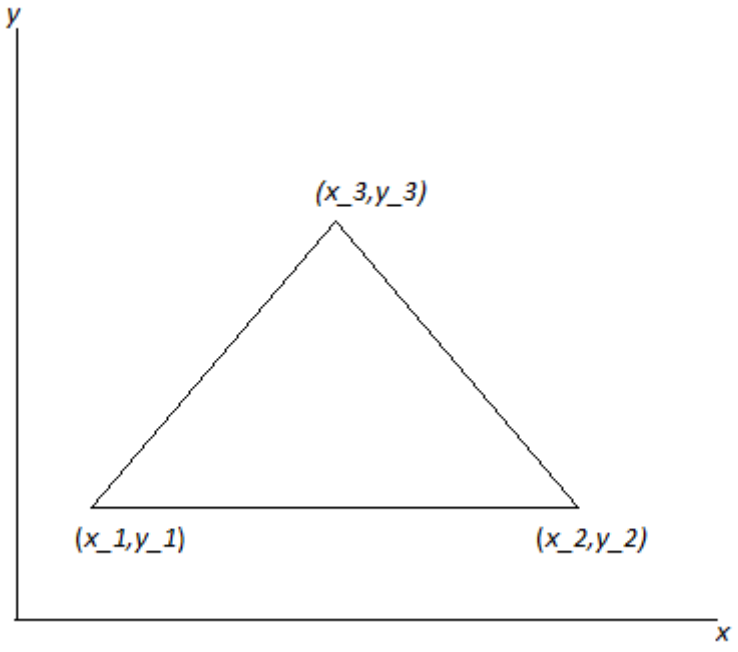

FIGURE 2.9: An example of a general triangle from which the basis functions will be mapped too.

The six quadratic basis functions on the reference triangle are defined as:

$$\begin{aligned}
\phi_1(\xi,\eta) &= 2(1-\xi-\eta)(\frac{1}{2}-\xi-\eta) \\
\phi_2(\xi,\eta) &= 2\xi(\xi-\frac{1}{2}) \\
\phi_3(\xi,\eta) &= 2\eta(\eta-\frac{1}{2}) \\
\phi_4(\xi,\eta) &= 4\xi(1-\xi-\eta) \\
\phi_5(\xi,\eta) &= 4\xi\eta \\
\phi_6(\xi,\eta) &= 4\eta(1-\xi-\eta)
\end{aligned} \tag{2.33}$$

Using barycentric coordinates, the physical point (x,y) can be mapped on the reference element by solving the following system:

$$\begin{pmatrix} x_2-x_1 & x_3-x_1 \\ y_2-y_1 & y_3-y_1 \end{pmatrix} \begin{pmatrix} \xi \\ \eta \end{pmatrix} = \begin{pmatrix} (x-x_1) \\ (y-y_1) \end{pmatrix} \tag{2.34}$$

where $\{(x_1,y_1),(x_2,y_2),(x_3,y_3)\}$ are the vertice positions of the triangles and (x,y) is the physical position. The coefficient matrix is the Jacobian matrix, $\mathbf{J}$, of the element. The reference coordinates can be found to be:

$$\begin{pmatrix} \xi \\ \eta \end{pmatrix} = \frac{1}{Det(\mathbf{J})} \begin{pmatrix} y_3-y_1 & x_1-x_3 \\ y_1-y_2- & x_2-x_1 \end{pmatrix} \begin{pmatrix} x-x_1 \\ y-y_1 \end{pmatrix} \tag{2.35}$$

or more compactly, $(\xi,\eta) : F(x,y) \rightarrow (\xi,\eta)$. Now the value of the basis functions at the mapped point $(x,y) \rightarrow (\xi,\eta)$ can trivially mapped back to the physical element since the height of basis function at a point is the same regardless of the size or orientation of the element. The situation is slightly different for the derivatives. The reference element is essentially a scaled physical element (in the case where the two elements are concentric). This means the derivatives of the basis functions will vary based on the relative size of the of reference element to the physical element. Once again a mapping can be used to solve this problem.

$$\begin{aligned}
\frac{\partial\phi_i(\xi(x,y),\eta(x,y))}{\partial x} &= \frac{\partial\phi_i}{\partial\xi}\frac{\partial\xi}{\partial x} + \frac{\partial\phi_i}{\partial\eta}\frac{\partial\eta}{\partial x} \\
\frac{\partial\phi_i(\xi(x,y),\eta(x,y))}{\partial y} &= \frac{\partial\phi_i}{\partial\xi}\frac{\partial\xi}{\partial y} + \frac{\partial\phi_i}{\partial\eta}\frac{\partial\eta}{\partial y}
\end{aligned} \tag{2.36}$$

Now that the basis functions have been found on the reference triangle and mapped to the physical triangle, the system can be solved. The next step is to integrate each term in the system. A numerical quadrature rule will be needed for this. An ideal

choice for the quadratic basis functions is the three point quadrature rule for triangles, also known as the mid point rule for triangles. This rule integrates quadratic functions exactly. The quadrature points and weights for a standard reference triangle are given below.

$$\begin{aligned}(x_1, y_1) &= (\frac{1}{2}, 0)\\ (x_2, y_2) &= (\frac{1}{2}, \frac{1}{2})\\ (x_3, y_3) &= (0, \frac{1}{2})\\ w_{(1,2,3)} &= \frac{1}{3}\end{aligned} \tag{2.37}$$

When a triangle is scaled or reoriented, the midpoint of each edge is used while the weights remain the same. To exemplify the quadrature rule, consider an entry of the mass matrix, $\mathbf{M}$ from Equation (2.32)

$$\int_E \phi_i \phi_j \, dE = \sum_k^{m_e} \int_{e_k} \phi_i \phi_j \, de_k = \sum_k^{m_e} \sum_n^3 w_n \phi_i(x_n, y_n) \phi_j(x_n, y_n) \tag{2.38}$$

where the first sum is the sum over the elements that create the domain of support for the basis functions. The second sum is the quadrature rule that sums over each pair of points and the associated weights.

Each entry in the matrix can now be evaluated numerally through the several previous steps.

$$\begin{gathered}\int_{Eij} (\nabla\phi_i \cdot \nabla\phi_j) + \phi_i \phi_j \, dE_{ij} = \int_E f\phi_i \, dE_{ij} + \int_L \phi_i g(y) dy\\ \Updownarrow\\ \sum_k^{m_e} \int_{e_k} (\nabla\phi_i \cdot \nabla\phi_j) + \phi_i \phi_j \, de_k = \sum_k^{m_e} \int_{e_k} f\phi_i \, de_k + \sum_k^{m_l} \int_{l_k} \phi_i g(y) \, dl_k\\ \Updownarrow\\ \sum_k^{m_e} \sum_n^3 w_n \{\nabla\phi_i(x_n, y_n) \cdot \nabla\phi_j(x_n, y_n) + \phi_i(x_n, y_n)\phi_j(x_n, y_n)\} =\\ \sum_k^{m_e} \sum_n^3 w_n f(x_n, y_n)\phi_i(x_n, y_n) \, de_k + \sum_k^{m_l} \sum_m^2 w_m \phi_i(1, y_m) g(y_m)\end{gathered} \tag{2.39}$$

where the line integral containing $g(y)$ has been evaluated using a two point, one dimensional, Gaussian quadrature rule. To summarize, once the matrix system is formed, the basis functions were evaluated in a reference triangle to expose the symmetry between each basis function on nodes in the physical element. Then the function values and

derivatives were mapped back into the physical element. Next the integrals are broken down into sums across each element in the respective domain of support. Finally each integral is approximated as a sum using Gaussian quadrature. The resulting system is completely numerical and can easily be solved by a general linear solver.

2.2.2 Time Discretization

Because we want to consider the time dependent GL equations we now turn to a simple problem which is time dependent. As an example, we add time dependence to the Helmholtz equation to get

$$u_t(x,t) - \Delta u(x,t) + u(x,t) = f(x,t) \tag{2.40}$$

$$\frac{u(x,t_n) - u(x,t_{n-1})}{\delta t} - \Delta u(x,t_n) + u(x,t_n) = f(x,t_n)\,. \tag{2.41}$$

There is no advantage to approximating in time with FEM so we use a finite difference approximation to the time derivative. For stability reasons, we choose an implicit method and for the numerical results presented here we choose the backward Euler method.

$$u(x,t_n) \approx \frac{u(x,t_n) - u(x,t_{n-1})}{\Delta t} \tag{2.42}$$

The weak form can then be made by choosing a space V and some set of boundary conditions to go with Equation 2.18. The weak problem is stated as seek $u \in V$ that satisfies.

$$\int_\Omega \{\frac{u(x,t_n) - u(x,t_{n-1})}{\Delta t} + (\nabla v \cdot \nabla u) + uv\}\, d\Omega = \int_\Omega fv\, d\Omega + \oint_{\partial\Omega} v\frac{\partial u}{\partial n}\, dS \quad \forall v \in V \tag{2.43}$$

This gives first order accuracy in time if the time.

2.2.3 Non-Linearities and the Newton-Raphson Method

Nonlinear algebraic equations can be solved by a method such as the Newton Rahpson method. As a simple example consider a one dimensional non linear function $f(x)$. The Newton-Raphson Method, also known as Newton's method can be formed as:

$$x_{n+1} = x_n - \frac{f(x_n)}{f'(x_n)} \tag{2.44}$$

An initial value x_0 must be chosen and this choice is critical in the methods convergence. If an x_o value is chosen too far away from the root, the method may convergence to an undesired root or diverge completely. Thankfully since Newton's method will be used on an IVBP, the time dependence helps avoid these problems, if the time step if sufficiently small. The initial value at $t = 0$ and solution at previous time steps gives a good choice of x_0 to guarantee convergence. If the IVBP has a global attractor, as is the case for the Ginzburg Landau equations[Du], the correct root will always be found based on the initial conditions.

Newton's method can also be generalized to systems of equations. Consider the matrix equation $\mathbf{Cx} = \mathbf{b}$, with $\mathbf{C}$ is $k \times k$. To form Newton's method the residual must first be formed,

$$\mathbf{R} = \mathbf{Cx} - \mathbf{b} \tag{2.45}$$

as well the Jacobian of the residual

$$\mathbf{J}[\mathbf{R}] = \begin{pmatrix} \frac{\partial R_1}{\partial x_1} & \frac{\partial R_1}{\partial x_2} & \cdots & \frac{\partial R_1}{\partial x_k} \\ \frac{\partial R_2}{\partial x_1} & \frac{\partial R_2}{\partial x_2} & \cdots & \frac{\partial R_2}{\partial x_k} \\ \vdots & \cdots & \ddots & \vdots \\ \frac{\partial R_k}{\partial x_1} & \frac{\partial R_k}{\partial x_2} & \cdots & \frac{\partial R_k}{\partial x_k} \end{pmatrix} \tag{2.46}$$

Each column in the Jacobian is formed by taking the derivative of each row with respect to the variable x_i from the vector $\mathbf{x}$ (not to be confused with the iterates x_n), then evaluating the derivatives at $\mathbf{x}_n$. Putting all this together in a similar fashion as Equation (2.44)

$$\mathbf{J}[\mathbf{R}(\mathbf{x}_n)](\mathbf{x}_{n+1} - \mathbf{x}_n) = -\mathbf{R}(\mathbf{x}_n) \tag{2.47}$$

2.3 Errors and Numerical Tests

Now the errors from the finite element method are reviewed to get a feeling of accuracy of the solutions of Ginzburg Landau model. Discrete errors are usually calculated using l_p norms, shown below,

$$l_p = (\frac{1}{m}\sum_{i}^{m}(u_i^h - u_i)^p)^{\frac{1}{p}} \tag{2.48}$$

where u_i^h is the approximated solution at the points and u is the true solution at the points. The l_2 norm, or the Euclidean norm, is the most common due to its effectiveness its simplicity. FEM provides a continuous solution on the domain using a linear combination of basis functions. This allows one to define the error across the whole domain,

known as the L_2 norm.

$$L_2 = (\int (u^h - u)^2 \, d\Omega)^{\frac{1}{2}} \tag{2.49}$$

Now u^h is defined continuously across Ω, as well as u. Once again the L_2 is the most common. The integral is evaluated much like the assembly of the FEM system, shown in Section 2.2.1 . The integral is broken down into a sum of integrals over each area of support for the respective basis functions. The error on the derivative of interest too. This is calculated using the semi-norm, which roots from Sobolev Spaces. Following [28] the L_2 norm can be notated as $|u|_0$, the L_2 first order semi norm can be notated as $|u|_1$. More generally any order semi norm can notated as $|u|_k$, where k is the order of the derivative. Now the L_2 errors can be found in ∇u^h,

$$L_2 = (\int (\nabla u^h - \nabla u)^2 \, d\Omega)^{\frac{1}{2}} \tag{2.50}$$

Now that the errors have been defined, the convergence of the h-method and p-method an be demonstrated numerically. Comparing two solutions with errors E_1 and E_2 defined on two different meshes with max mesh (element) sizes h_1 and h_2,

$$\frac{E_1}{E_2} = (\frac{h_1}{h_2})^r \tag{2.51}$$

where r is the rate of convergence. Rearranging, the convergence rate can shown to be,

$$r = \frac{log(\frac{E_1}{E_2})}{log(\frac{h_1}{h_2})} \tag{2.52}$$

The optimal convergence rate r is essentially dictated by the power of the polynomial used for the basis functions. Analytically it can be shown for polynomial basis function of power n, the optimal convergence rate is $r = n+1$ for the L_2 norm error. In a similar fashion the convergence rate of ∇u is $r = n$. This lower semi-norm is due to the lower constraints on the derivatives produced by the weak form.

The convergence rates for decreasing element size h and increasing polynomial powers p can show numerically using Poisson's equation in two dimensions.

$$\begin{gathered} -\Delta u(x,y) = 2\pi^2 sin(\pi x) sin(\pi y) \\ \Omega = (0,1) \times (0,1) \\ u(0,y) = 0 \\ u(1,y) = 0 \\ u(x,0) = u(x,1) = x \\ u(x,y) = sin(\pi x) sin(\pi y) + x \end{gathered} \tag{2.53}$$

Now the Finite Element Method can be applied to the problem above for various elements sizes and linear and quadratic polynomials. The results are tabulated below. As can

Table 2.1

$\mathbb{P}^n$	h	$\|u^h - u\|_0$	$\|\nabla u^h - \nabla u\|_1$	Conv. rate of $L2$	Conv. rate of SN
Linear	0.125	0.050737	0.852356		
Linear	0.625	0.011278	0.401787	2.169510	1.085026
Linear	0.03125	0.002652	0.194834	2.088153	1.044182
Linear	0.015625	0.000643	0.095919	2.044661	1.022358
Linear	0.0078125	0.000158	0.047588	2.022446	1.011230
quadratic	0.125	0.000827	0.044114		
quadratic	0.625	0.000084	0.009608	3.306119	2.198935
quadratic	0.03125	0.000009	0.002250	3.143553	2.094589
quadratic	0.015625	0.000001	0.000545	3.069631	2.046162
quadratic	0.0078125	1.2×10^{-7}	0.000134	3.034306	2.022808

TABLE 2.1: The table shows the convergence of the FEM with linear and quadratic basis functions. The convergence of the method for a n power polynomial are shown to be $n+1$ for u and n for ∇u.

be seen in Table 2.1 the linear polynomial basis function yields quadratic convergence on u^h and linear convergence on ∇u^h. The quadratic provide cubic convergence for u and quadratic convergence for ∇u^h. Now that the computational methods have been reviewed, it can be applied to the Ginzburg Landau equations and variants. Throughout the following sections the Ginzburg Landau theory is investigated more deeply and Finite Element approximations are used to make predictions for superconducting materials using the Ginzburg Landau theory.

Chapter 3

The Ginzburg-Landau Theory

3.1 Ginzburg Landau Theory Overview

The Ginzburg-Landau theory shown in Chapter 1 is a powerful formalism to describe superconductors, while avoiding the complicated quantum effects described by BCS theory. This makes Ginzburg-Landau theory ideal for computations. The Ginzbrug Landau theory is mesoscopically scaled theory. The theory was derived using Landau's theory of second order (continuous) phase transpositions. The simplest case is when a bulk superconducting sample is near T_c, there is no superconducting current, and since the sample is large, the change in the complex order parameter ψ can be ignored [29]. The free energy of the system can then be expanded in ψ to the second power. If F is the free energy, F_n is the constant free energy of the normal state, and Ω is domain of the sample then,

$$F = F_n + \int_\Omega \alpha(T)|\psi|^2 + \frac{1}{2}\beta(T)|\psi|^4 \, d\Omega \tag{3.1}$$

where α and β are temperature dependent material constants, that serve as expansion coefficients. $\alpha(T)$ is negative when the sample is in the superconducting state ($T < T_c$) and positive when the sample is in the normal state ($T > T_c$). For the entire temperature regime, $\beta > 0$. The free energy should always be minimized in a system, so the function ψ that minimizes F can be found using calculus of variations. The minimizer or the Euler Lagrange equation can be found by varying the path of ψ by adding $\epsilon\phi$, ϕ begin the test function. Now a functional derivative can be applied and the Euler Lagrange Equations found.

$$\lim_{\epsilon \to 0} \frac{F(\psi + \epsilon\phi) - F(\psi)}{\epsilon} = 0 \tag{3.2}$$

yielding,

$$\int_\Omega \alpha(T)\psi\phi + \frac{1}{2}\beta(T)|\psi|^2\psi\phi \, d\Omega = 0 \tag{3.3}$$

Inspecting Equation (3.3), notice it that has the same structure as the weak form for the finite elements method, with ϕ being a test function in the vector space V_h. In this way variational methods and FEM are related and FEM can even be derived using variational methods as will be seen for the Ginzburg-Landau Equations. If the integral for all ϕ in some space V is 0, then the integrand can shown to be 0 also. Setting the integrand equal to zero and dividing off the test function, the Euler Lagrange equation for the simplified free energy is obtained.

$$\alpha(T)\psi + \frac{1}{2}\beta(T)|\psi|^2\psi = 0 \tag{3.4}$$

Now the influence of the expansion coefficients comes into play. α and β in the Ginzburg-Landau can be rigorously obtained using the Quasi-classical approximation of the BCS theory [30],[14].

$$\begin{aligned} \alpha(T) &= \nu(0)ln(\frac{T}{T_c}) \\ \beta(T) &= \frac{7\zeta(3)\nu(0)}{8\pi^2T^2} \end{aligned} \tag{3.5}$$

where $\nu(0)$ is the density of states at the Fermi level, $\zeta()$ is Riemann Zeta function, and the units are such that the Boltzmann constant k_b is equal to 1. For $T \approx T_c$, α and β can be approximated as in Equation (1.12) [30],[14].

$$\begin{aligned} \alpha(T) &\approx -\alpha(0)(1 - \frac{T}{T_c}) = \alpha(1 - \frac{T}{T_c}) \\ \beta(T) &\approx \frac{7\zeta(3)\nu(0)}{8\pi^2T_c^2)} = \beta(0) = \beta \end{aligned} \tag{3.6}$$

Where $\alpha(0)$ and $\beta(0)$ are constant throughout the temperature range. Plugging the values into Equation (3.4) and solving for ψ,

$$|\psi|^2 = |\psi_\infty|^2 = \frac{-\alpha}{\beta} = n_s \tag{3.7}$$

Since the squared modulus is semi-positive definite, then $\frac{-\alpha}{\beta} \geq 0$. Thus in order to minimize the free energy, the order parameter is zero when α is positive and non zero when α is negative. Physically the order parameter represents quasi-classical wave function for the superconducting electron pairs. The squared modulus is proportional to the probability density of the superconducting electrons, n_s[16]. When $T > T_c$, α is positive and the sample is in the normal state. Here no superconducting effects exists and thus the density of superconducting electrons is zero. While if $T < T_c$, α is negative and ψ becomes $\sqrt{\frac{\alpha(0)(1-\frac{T}{T_c})}{\beta}}$. ψ_∞ is known as the solution in the bulk, and serves as the maximum value for ψ in most cases. This is the value of ψ deep inside of a large

superconducting sample, being shielded from any fields or currents.This makes the bulk value ideal for non-dimensionalizing the Ginzburg-Landau theory. Another value useful for non-dimensionalization is the thermodynamic critical field, H_c. From [16] the thermodynamic critical field can be shown to be

$$f_s - f_n = \frac{-H_c^2}{8\pi} = \frac{-\alpha^2}{\beta} \tag{3.8}$$

f_n and f_s are the free energy densities of the normal and superconducting states respectively. $\frac{-H_c^2}{8\pi}$ represents the energy needed to repel a magnetic field from the interior of a superconductor that is exhibiting the Meissner effect. The Thermodynamic critical field has the temperature dependence[16],

$$H_c(T) = H_c(0)(1 - (\frac{T}{T_c})^2) \tag{3.9}$$

The free energy in Equation (3.1) can expanded further, including terms to capture spatial changes in ψ along with the accompanying super current density $\mathbf{J}_s$, and an applied magnetic field.

3.1.1 Spatial Variations in ψ, Super-Currents, Applied Magnetic Fields, and Characteristic Lengths

Similar to the London theory, the kinetic energy of the superconductor and the energy from the magnetic field are described in the Ginzburg-Landau free energy.

$$G = F_n + \int_\Omega \alpha(T)|\psi|^2 + \frac{1}{2}\beta(T)|\psi|^4 + \frac{1}{2m^*}|(-i\hbar\nabla - \frac{e^*}{c}\mathbf{A})\psi|^2 + \frac{|\mathbf{h}|^2}{8\pi}\, d\Omega \tag{3.10}$$

$\mathbf{A}$ is the magnetic vector potential, e^* and m^* are the effective charge and mass of a superconducting electron pair and $\mathbf{B}$ is the magnetic field produced by the system,

$$\mathbf{h} = \nabla \times \mathbf{A} \tag{3.11}$$

$\mathbf{h}^2$ is a abbreviated for $\mu\mathbf{H}^2$. The first term in the functional G is the free energy of the normal state. The terms containing α and β give the energy from the phase transition. The term containing the gradient is the kinetic energy of the electrons, where guage invariant derivative is used. The last term is the energy from the induced and external magnetic fields. The energy density for a magnetic field is of the form $\frac{\mathbf{B}^2}{2\mu}$ and for the case of diamagnetism (which is the case for superconductors) it can be shown that $\mathbf{B} = \mu\mathbf{H}$. Thus the energy density can shown to be of the form $\mu\mathbf{H}^2 = \mathbf{H}^2$, by dimensional analysis. The gradient/ kinetic energy term can be included as follows.

Consider the kinetic energy of a particle, classically and quantum mechanically

$$\frac{p^2}{2m} = \frac{(i\hbar\nabla)^2}{2m} \tag{3.12}$$

This can be generalized for an electromagnetic field using the canonical momentum (also known as the gauge invariant derivative for the fields).

$$mv = \Pi = p - \frac{e}{c}\mathbf{A} \tag{3.13}$$

Then the kinetic energy for the electrons is

$$\frac{mv^2}{2} = \frac{(i\hbar\nabla - \frac{e^*}{c}\mathbf{A})^2}{2m} \tag{3.14}$$

From the kinetic movement of the electrons, a super current $\mathbf{J}_s$ will be induced and can be found using the quantum continuity equation,

$$-\nabla \cdot \mathbf{j} = e\frac{\partial|\psi|^2}{\partial t} \tag{3.15}$$

noting that $|\psi|^2 = \psi\psi^*$ and using Schrödinger's equation for ψ and ψ^*.

$$e\frac{\partial|\psi|^2}{\partial t} = e(\frac{\partial\psi}{\partial t} + \frac{\partial\psi}{\partial t}) = \frac{e}{-i\hbar 2m}(\psi^*\Pi^2\psi) + \frac{e}{i\hbar}(\psi\Pi^{2*}\psi^*) \tag{3.16}$$

The $\mathbf{A}^2$ terms cancel on the right hand side and the divergence operator can pulled out of the terms to form,

$$e\frac{\partial|\psi|^2}{\partial t} = -\nabla\cdot\mathbf{j} = \nabla\cdot(\frac{ie\hbar}{2m}(\psi^*\nabla\psi - \psi\nabla\psi^*) + \frac{e^2}{mc}|\psi^2|\mathbf{A}) \tag{3.17}$$

Which leads to the super current being

$$\mathbf{J}_s = -(\frac{ie^*\hbar}{2m^*}(\psi^*\nabla\psi - \psi\nabla\psi^*) + \frac{e^{*2}}{m^*c}|\psi^2|\mathbf{A}) \tag{3.18}$$

Now that the super current has been derived, the effects of an applied magnetic field on a superconductor using the Ginzburg-Landau theory can be investigated. To begin with, the Meissner effect can be explained using the super current and Maxwell's laws. First the order parameter is made into a modulus and a phase, $\psi = |\psi|e^{i\phi(\mathbf{r}}$, where $\phi(r)$ is the phase of the wave at position $\mathbf{r}$. Then super current becomes,

$$\mathbf{J}_s = \frac{e^*|\psi|^2}{m^*}(\hbar\nabla\phi - \frac{e^*}{c}\mathbf{A}) \tag{3.19}$$

and taking the curl of the super current reduces to

$$\nabla \times \mathbf{J}_s = -\frac{e^*|\psi|^2}{m^*}\frac{e^*}{c}\nabla \times \mathbf{A}) = -\frac{e^*|\psi|^2}{m^*}\frac{e^*}{c}\mathbf{B} \tag{3.20}$$

using Ampere's Equation and forming the Laplacian of $\mathbf{B}$

$$\nabla \times \mathbf{B} = \frac{4}{\pi}\mathbf{J}_s \tag{3.21}$$

$$-\nabla \times \nabla \times \mathbf{B} = -\Delta\mathbf{B} = \frac{4\pi}{c}\frac{e^*|\psi|^2}{m^*}\frac{e^*}{c}\mathbf{B} = \frac{1}{\lambda^2}\mathbf{B} \tag{3.22}$$

Solving this leads to the exponential decaying magnetic field seen in the Meissner effect. The penetration depth λ has also been derived, which dictates how far the field penetrates the sample. Using $|\psi|^2 = \frac{-\alpha}{\beta}$, λ becomes,

$$\lambda(T) = \sqrt{-\frac{m^*\beta c^2}{4\pi\alpha(T)e^{2*}}} \tag{3.23}$$

λ is also an important constant for nondimensionalizion that will be used later.

To include an applied magnetic field, $\mathbf{H}_e$, the free energy in Equation (3.10) is modified by the term $-\frac{\mathbf{H}_e\cdot\mathbf{h}}{4\pi}$. To simplify things the new magnetic field terms with $\mathbf{B}$ and $\mathbf{H}_e$ become $\frac{|\mathbf{h}-\mathbf{H}_e|^2}{8\pi}$. This modification does not change the minimizers of the functional[14]. The free energy becomes,

$$G = F_n + \int_\Omega \alpha(T)|\psi|^2 + \frac{1}{2}\beta(T)|\psi|^4 + \frac{1}{2m^*}|(-i\hbar\nabla - \frac{e^*}{c}\mathbf{A})\psi|^2 + \frac{|\mathbf{h}-\mathbf{H}_e|^2}{8\pi}\, d\Omega \tag{3.24}$$

Now a similar method of calculus of variations is used as was used for Equation (3.4), to minimize the modified free energy. The variation is done in ψ^* (equivalent to varying ψ) and a second variation is done in $\mathbf{A}$, yielding two Euler Lagrange Equations. The Ginzburg-Landau Equations are,

$$\alpha(1-\frac{T}{T_c})\psi + \beta|\psi|^2\psi + \frac{1}{2m^*}(-i\hbar\nabla - \frac{e^*\mathbf{A}}{c})^2\psi = 0, \text{ in } \Omega \tag{3.25}$$

$$\frac{1}{4\pi}\nabla \times (\nabla \times \mathbf{A} - \mathbf{H}) = \frac{-ie^*\hbar}{2m^*}(\psi^*\nabla\psi - \psi\nabla\psi^*) - \frac{e^{2*}}{m^*c}|\psi|^2\mathbf{A} = \mathbf{J}_s, \text{ in } \Omega \tag{3.26}$$

with boundary conditions:

$$\begin{aligned}(-i\hbar\nabla - \frac{e^*}{c}\mathbf{A})\psi\cdot\mathbf{n} = 0, \text{ on } \partial\Omega\\ (\nabla\times\mathbf{A} - \mathbf{H}_e)\times\mathbf{n} = 0, \text{ on } \partial\Omega\end{aligned} \tag{3.27}$$

The first equation describes the order parameter and the second describes the magnetic vector potential. The boundary conditions are such that the surface terms from the calculus of variations are zero. The boundary conditions also have physical implications too. The first one assures that no super current crosses the boundary, indicative of a Insulator-Superconductor interface[14]. However for a Normal Metal-Superconductor interface, the proximity effect must be accounted for. The proximity effect is where some of super current leaks into the normal metal surrounding it, as is the case for a sample with metal leads carrying a applied current. The corresponding boundary condition is

$$(-i\hbar\nabla - \frac{e^*}{c}\mathbf{A})\psi \cdot \mathbf{n} = i\hbar\zeta\psi \quad on \quad \partial\Omega \tag{3.28}$$

where the super current still does not leave the sample, implying $\mathbf{J}_s \cdot \mathbf{n} = 0$ on $\partial\Omega$. This boundary condition becomes the natural boundary condition of the the free energy functional if the term $\int_{\partial\Omega} \bar{\zeta}|\psi|^2$ is added.

Now in a similar manner as [16], the characteristic length of ψ can be found. This is the length over which any appreciable change in ψ exists[8]. Simplifying the ψ equation to one dimension, setting $\mathbf{A} = 0$ (absence of fields) and normalizing ψ by the bulk solution $\psi_\infty = \sqrt{\frac{-\alpha}{\beta}}$ to produce $f = \frac{\psi}{\psi_\infty}$, we find the ψ becomes,

$$\frac{\hbar^2}{2m^*|\alpha|}\frac{d^2f}{dx^2} + f - f^3 = 0 \tag{3.29}$$

From this it can seen that the scale over which ψ changes is the coherence length, defined as

$$\xi(T) = \sqrt{-\frac{\hbar^2}{2m^*\alpha(T)}} \tag{3.30}$$

This can be shown further by assuming f is small, signifying a small change in ψ from the equilibrium value ψ_∞. Thus solving a linearized differential equation, yielding an exponential solution scaled by $\xi(T)$, similar to the derivation of λ.

In this section the G.L. theory was derived as well as several characteristic parameters. These parameters provide a very natural way to non-dimensionalize the G.L. equations, while including empirical parameters. $\alpha(T)$, $\beta(T)$,$|\psi_\infty|^2$ can be redefined

using λ and H_c.

$$\begin{aligned} |\psi_\infty(T)|^2 = n_s &= \frac{m^* c^2}{4\pi e^{2*}\lambda^2(T)} \\ \alpha(T) &= -\frac{e^{2*}}{m^* c^2} H_c^2(T)\lambda^2(T) \\ \beta(T) &= \frac{4\pi e^{4*}}{m^{2*} c^4} H_c^2(T)\lambda^4(T) \end{aligned} \tag{3.31}$$

Now ξ can be related to magnetic effects inside the superconductor by using the new value for $\alpha(T)$.

$$\xi(T) = \frac{\mathbf{\Phi}_0}{2\sqrt{2}\pi H_c(T)\lambda(T)} \tag{3.32}$$

and similarly we can defined $H_c(T)$ as

$$H_c(T) = \frac{\mathbf{\Phi}_0}{2\sqrt{2}\pi\xi(T)\lambda(T)} \tag{3.33}$$

where $\mathbf{\Phi}_0 = \frac{hc}{e^*}$ is the quantum fluxoid, which is related to magnetic vortices in Type-II superconductors.

So far all these values have been defined with their temperature dependences. To further simplify things the temperature dependence can be separated from these parameters and their constant temperature independent values are used. Then the temperature dependence is captured in the GL equations by the $(1 - \frac{T}{T_c}) = \tau$ term. The temperature dependence near $T = T_c$ lies only in $\alpha(T)$, inspecting $\xi(T)$,$\lambda(T)$, and ψ_∞ for their α dependence, it is found that

$$\begin{aligned} \xi(T) &\approx \xi(0)\tau^{-\frac{1}{2}} \\ \lambda(T) &\approx \lambda(0)\tau^{-\frac{1}{2}} \\ \psi_\infty(T) &\approx \psi_\infty(0)\tau^{\frac{1}{2}} \end{aligned} \tag{3.34}$$

The T=0 values are those used for non dimensionalizaion. Finally another important parameter is the Ginzbrug Landau parameter κ,

$$\kappa = \frac{\lambda(0)}{\xi(0)} \tag{3.35}$$

The value of κ for a material dictates if a material is a Type I or Type II superconductor. If $\kappa < \frac{1}{\sqrt{2}}$, then the material is Type I material and experience the full Meissner effect until the superconductivity is destroyed by a magnetic field of strength H_c. For $\kappa > \frac{1}{\sqrt{2}}$ the material is a Type II superconductor, where a semi Meissner effect is exhibited between for a field strength H of $H_{c1} < H < H_{c2}$. This is due to the fact that when $\kappa > \frac{1}{\sqrt{2}}$, it is energetically favorable to create normal states inside the sample to

maintain a mixed state state [14] .In this mixed state, the magnetic field penetrates the sample with magnetic flux quantum $\mathbf{\Phi_0}$, that generates magnetic vortices in the sample. The super current density $\mathbf{J}_s$ is current produced by the vortices that encircles them. Below H_{c1}, Type II superconductors experience the full Meissner effect, and above H_{c2} superconductivity ceases. H_{c1} and H_{c1} can be found to be [14],

$$H_{c1}(T) = \frac{H_c(T) ln\kappa}{\sqrt{2}\kappa} H_{c2}(T) = \sqrt{2} H_c(T) \tag{3.36}$$

with$H_{c1}(T) < H_c(T) < H_{c2}(T)$. The magnetic vortices associated with Type II superconductors can be seen in the order parameter ψ. The sites where the magnetic field penetrates the sample in vortices creates destroys the superconductivity and creates normal sites. This can be seen in ψ where the value goes to 0 but only in a local radial manner. This represents the absence of superconducting electrons in the normal sites created by the vortices.

3.1.2 Time dependence and Non dimensionalization

Now that the Ginzburg-Landau theory has been reviewed, extensions of the model can be derived. As shown in Chapter 1, the Time Dependent Ginzburg-Landau model was discovered by Gor'kov and Eliashberg in 1968. Viewing the Ginburg Landau equations from (3.25) and (3.26) as variations in the free energy in Equation (3.24), the variation in ψ^* can be equated to a small disturbance in equilibrium of the superconductor.

$$\Gamma(\frac{\partial \psi}{\partial t} + \frac{ie}{\hbar}\Phi\psi) = -\frac{\delta G}{\delta \psi *}, \tag{3.37}$$

where Γ is a positive relaxation constant. The time dependence of $\mathbf{A}$ can be captured by inspecting the normal current density generated by a disturbance in the superconductor.

$$\mathbf{J}_n = \sigma_n \mathbf{E} = -(\frac{1}{c}\frac{\partial \mathbf{A}}{\partial t} + \nabla\Phi) \tag{3.38}$$

where σ_n is the conductivity of the material, $\mathbf{E}$ is the electric field, and Φ is the scalar electric potential. Now the total current density, $\mathbf{J} = \mathbf{J}_n + \mathbf{J}_s$, with $\mathbf{J}_s = -c\frac{\partial F_s}{\partial A}$, becomes

$$\boldsymbol{j} = j_n + j_s = \sigma_n(-\frac{1}{c}\frac{\partial A}{\partial t} - \nabla\phi) - c\frac{\partial F_s}{\partial A}, \tag{3.39}$$

This generates the Time Dependent Ginzburg-Landau Equations,

$$\Gamma(\frac{\partial \psi}{\partial t} + \frac{ie}{\hbar}\phi\psi) + \alpha(1 - \frac{T}{T_c})\psi + \beta|\psi|^2\psi + \frac{1}{2m^*}(-i\hbar\nabla - \frac{e^*\mathbf{A}}{c})^2\psi = 0, \text{ in } \Omega \tag{3.40}$$

$$\frac{1}{4\pi}\nabla\times(\nabla\times\mathbf{A}-\mathbf{H}) = \sigma_n(-\frac{1}{c}\frac{\partial A}{\partial t}-\nabla\Phi)+\frac{-ie^*\hbar}{2m^*}(\psi^*\nabla\psi-\psi\nabla\psi^*)-\frac{e^{2*}}{m^*c}|\psi|^2\mathbf{A} = \mathbf{J}_s, \quad textin \ \ \Omega \tag{3.41}$$

with initial and boundary conditions:

$$\begin{gathered}(-i\hbar\nabla - \frac{e_s}{c}\mathbf{A})\psi\cdot\mathbf{n} = 0, \ \text{ on } \ \partial\Omega \ \text{ and } \ \forall t \\ (\nabla\times\mathbf{A} - H_e)\times\mathbf{n} = 0, \ \text{ on } \ \partial\Omega \ \text{ and } \ \forall t \\ \psi(x,0) = \psi_0(x), \quad \text{in}\Omega \\ \mathbf{A}(x,0) = \mathbf{A}_0(x), \quad \text{in}\Omega\end{gathered} \tag{3.42}$$

The time evolution of the superconducting sample can now be captured by the model. This is useful for modeling the vortex dynamics of Type II superconductors as well as applied current. To improve the numerics of a computational simulation, the equations can be non-dimensionlied. The non-dimensionalization improves the scaling and introduces new parameters, typically more convenient in some manner than the dimensionalized ones . $\xi(0)$, $\lambda(0)$, κ, ψ_∞, and H_c are used to help form the non dimensional variables. This removes α and β from the GL equations and replaces them with $\xi(0)$, $\lambda(0)$, κ, as the material input parameters. The following non-dimensional parameters (with bars over them) are used to make the TDGL equations non dimensionalized.

$$\begin{gathered}x = x_0\bar{x}, \qquad t = \bar{t}\frac{(-\alpha)}{\Gamma\hbar} \\ H_c = \sqrt{\frac{8\pi\alpha^2}{\beta}}, \quad \mathbf{A} = H_c x_0\bar{\mathbf{A}} \\ \mathbf{H} = \sqrt{2}H_c\bar{\mathbf{H}} \quad \psi = \sqrt{\frac{-\alpha}{\beta}}\bar{\psi} \\ \lambda = \sqrt{-\frac{c^2m^*\beta}{4\pi e^{*2}\alpha}}, \quad \xi = \sqrt{-\frac{\hbar^2}{2m^*\alpha}} \\ \sigma_n = \frac{\Gamma c^2}{2\pi\hbar}\sigma, \quad \Phi = \frac{-\alpha}{\Gamma}\bar{\Phi}\end{gathered} \tag{3.43}$$

These values can be inserted into Equations (3.39)-(3.40) and simplified, yielding the non-dimensionalized TDGL equations.

$$(\frac{\partial\psi}{\partial t} + i\Phi\psi) + (|\psi|^2 - \tau)\psi + (-i\frac{\xi}{x_0}\nabla - \frac{x_0}{\lambda}\mathbf{A})^2\psi = 0 \tag{3.44}$$

$$\sigma(\frac{1}{\lambda^2}\frac{\partial\mathbf{A}}{\partial t} + \frac{1}{\kappa}\nabla\Phi) + \nabla\times\nabla\times\mathbf{A} + \frac{i}{2\kappa}(\psi\nabla\psi^* - \psi^*\nabla\psi) + \frac{1}{\lambda^2}|\psi|^2\mathbf{A} = \nabla\times\mathbf{H}_e \tag{3.45}$$

$$\begin{aligned}(-i\frac{\xi}{x_0}\nabla - \frac{x_0}{\lambda}\mathbf{A})\psi\cdot\mathbf{n} = 0, \ \text{ on } \partial\Omega \text{ and } \forall t\\ (\nabla\times\mathbf{A} - H_e)\times\mathbf{n} = 0, \ \text{ on } \partial\Omega \text{ and } \forall t\\ \psi(x,0) = \psi_0(x), \quad \text{in } \ \Omega\\ \mathbf{A}(x,0) = \mathbf{A}_0(x), \quad \text{in } \ \Omega\end{aligned} \tag{3.46}$$

and with

$$\tau = 1 - \frac{T}{T_c}$$

Now the TDGL equations are a two equations system with three variables. This system is not suited for computations and must be closed using a gauge transformation. In electrodynamics, there may be several arrangements of potentials Φ and $\mathbf{A}$ that produce an electrodynamic field. The transformation from one set of potential to another is known as a gauge transformation.

$$G_\chi(\psi,\mathbf{A},\Phi) \to (\psi e^{i\chi}, \mathbf{A} + \frac{\hbar c}{e^*}\nabla\chi, \Phi - \frac{\hbar}{e^*}\frac{\partial\chi}{\partial t}) \tag{3.47}$$

The TDGL are invariant under one of these transformation. Typically the gauge transformation is used to replace Φ by a function of $\mathbf{A}$. Now some of the typical gauge choices are reviewed.

The first gauge choice is the Coulumb gauge, which assumes $\mathbf{A}$ is divergence free. The gauge transformation can be satisfied by

$$\begin{aligned}\Delta\chi = -\nabla\cdot\mathbf{A} = 0 \ \text{ in } \ \Omega\\ \nabla\chi\cdot\mathbf{n} = -\mathbf{A}\cdot\mathbf{n} \ \text{ on } \ \Gamma\end{aligned} \tag{3.48}$$

where Γ is the boundary of Ω. This gauge is very useful for steady state equations such as the elliptical GL equations but it is not suited for quadratic problems due the the divergence free magnetic vector potential. The next gauge is the Lorenz gauge, which is obtained by,

$$\frac{\partial\chi}{\partial t} - \Delta\chi = \Phi \pm \nabla\cdot\mathbf{A} \ \ on \ \ \Omega \tag{3.49}$$

and boundary condition

$$\nabla\chi\cdot\mathbf{n} = \pm\mathbf{A}\cdot\mathbf{n} \ \ on \ \ \Gamma \tag{3.50}$$

This gauge can be used to replace Φ by $\pm\nabla\cdot\mathbf{A}$. Then the curl term and the divergence term can be made into the vector Laplacian. The TDGL equations in the Lorenz gauge have the additional boundary condition,

$$\mathbf{A}\cdot\mathbf{n} = 0 \tag{3.51}$$

and the initial condition

$$\nabla \cdot \mathbf{A} = 0 \text{ in } \Omega \tag{3.52}$$

Finally we have the simplest and most common gauge, the zero potential gauge, or the $\Phi = 0$ gauge. The gauge transformation becomes

$$\frac{\partial \chi}{\partial t} = \Phi \tag{3.53}$$

with initial conditions (at $t = 0$),

$$\begin{aligned} \Delta\chi &= -\nabla \cdot \mathbf{A} \text{ in } \Omega \\ \nabla\chi \cdot \mathbf{n} &= -\mathbf{A} \cdot \mathbf{n} \text{ on } \Gamma \end{aligned} \tag{3.54}$$

This is the gauge choosen for the numerical studies below (in the case of applied current the gauge is modified). In the zero potential gauge the TDGL equations become,

$$(\frac{\partial \psi}{\partial t}) + (|\psi|^2 - \tau)\psi + (-i\frac{\xi}{x_0}\nabla - \frac{x_0}{\lambda}\mathbf{A})^2\psi = 0 \tag{3.55}$$

$$\sigma(\frac{1}{\lambda^2}\frac{\partial \mathbf{A}}{\partial t}) + \nabla \times \nabla \times \mathbf{A} + \frac{i}{2\kappa}(\psi\nabla\psi^* - \psi^*\nabla\psi) + \frac{1}{\lambda^2}|\psi|^2\mathbf{A} = \nabla \times \mathbf{H}_e \tag{3.56}$$

$$\begin{aligned} \nabla\psi \cdot \mathbf{n} = 0, &\text{ on } \partial\Omega \text{ and } \forall t \\ (\nabla \times \mathbf{A} - H_e) \times \mathbf{n} = 0, &\text{ on } \partial\Omega \text{ and } \forall t \\ \mathbf{A} \cdot \mathbf{n} = 0, &\text{ on } \partial\Omega \text{ and } \forall t \\ \nabla \cdot \mathbf{A}(\mathbf{x}, 0) = 0 &\text{ in } \Omega \\ \psi(x, 0) = \psi_0(x), &\text{ in } \Omega \\ \mathbf{A}(x, 0) = \mathbf{A}_0(x), &\text{ in } \Omega \end{aligned} \tag{3.57}$$

Now that the TDGL system has been closed by the zero potential gauge, the system can be put in the weak form to make it applicable to FEM. Defining the inner product as,

$$(f, g) = \int_\Omega f^* \cdot g \, d\Omega \tag{3.58}$$

where f and g can be scalars or vectors and * represents the complex conjugate. Assuming the solution variables, ψ and $\mathbf{A}$, can be well approximated in some vector space $\mathcal{V} \times \mathbf{V}$. Then we can choose the test functions to be, $(\tilde{\psi}, \tilde{\mathbf{A}}) \in \mathcal{V} \times \mathbf{V}$. The weak from can derived either by multiplying the TDGL equations by the appropriate test function and integrating by parts or the variations in the free energy can be found using $(\tilde{\psi}, \tilde{\mathbf{A}})$ to vary the path of ψ and $\mathbf{A}$. After applying one of the methods the weak form for the

TDGL equations in the zero potential gauge is,

$$(\frac{\partial\psi}{\partial t},\tilde{\psi})+([|\psi|^2-\tau)\psi],\tilde{\psi})+(-i\frac{\xi}{x_0}\nabla\psi-\frac{x_0}{\lambda}\mathbf{A}\psi,-i\frac{\xi}{x_0}\nabla\tilde{\psi}-\frac{x_0}{\lambda}\mathbf{A}\tilde{\psi})=0 \tag{3.59}$$

$$\sigma(\frac{1}{\lambda^2}\frac{\partial\mathbf{A}}{\partial t},\tilde{\mathbf{A}})+(\nabla\times\mathbf{A},\nabla\times\tilde{\mathbf{A}})+(\frac{i}{2\kappa}[\psi\nabla\psi^*-\psi^*\nabla\psi],\tilde{\mathbf{A}})+(\frac{1}{\lambda^2}|\psi|^2\mathbf{A},\tilde{\mathbf{A}})=(\mathbf{H}_e,\nabla\times\tilde{\mathbf{A}}) \tag{3.60}$$

$$\begin{aligned}\nabla\cdot\mathbf{A}(\mathbf{x},0)&=0\ \ \Omega\\ \psi(x,0)&=\psi_0(x),\qquad \Omega\\ \mathbf{A}(x,0)&=\mathbf{A}_0(x),\qquad \Omega\end{aligned} \tag{3.61}$$

Since all the boundary conditions are Neumann they are naturally included in the weak form. Now the Jacobian for the Newton system can formed and the Nonlinear problem solved. As in [4][6][7], and [14], the following modified problem is solved using FEM.

$$(\frac{\partial\psi}{\partial t},\tilde{\psi})+([|\psi|^2-\tau)\psi],\tilde{\psi})+(-i\frac{\xi}{x_0}\nabla\psi-\frac{x_0}{\lambda}\mathbf{A}\psi,-i\frac{\xi}{x_0}\nabla\tilde{\psi}-\frac{x_0}{\lambda}\mathbf{A}\tilde{\psi})=0 \tag{3.62}$$

$$\begin{aligned}&\sigma(\frac{1}{\lambda^2}\frac{\partial\mathbf{A}}{\partial t},\tilde{\mathbf{A}})+(\nabla\times\mathbf{A},\nabla\times\tilde{\mathbf{A}})+\epsilon(\nabla\cdot\mathbf{A},\nabla\cdot\tilde{\mathbf{A}})\\ &+(\frac{i}{2\kappa}[\psi\nabla\psi^*-\psi^*\nabla\psi],\tilde{\mathbf{A}})+(\frac{1}{\lambda^2}|\psi|^2\mathbf{A},\tilde{\mathbf{A}})=(\mathbf{H}_e,\nabla\times\tilde{\mathbf{A}})\end{aligned} \tag{3.63}$$

$$\begin{aligned}\nabla\cdot\mathbf{A}(\mathbf{x},0)&=0\ \text{ in }\ \Omega\\ \psi(x,0)&=\psi_0(x),\ \text{ in }\ \Omega\\ \mathbf{A}(x,0)&=\mathbf{A}_0(x),\ \text{ in }\ \Omega\end{aligned} \tag{3.64}$$

The $\epsilon(\nabla\cdot\mathbf{A},\nabla\cdot\tilde{\mathbf{A}})$ term is used to improve the convergence of the finite element method, and in [6], the modified problem above is proved to produces the correct steady solution as $\epsilon\to 0$.

In Figure 3.1 is an example of the order parameter ψ for $\lambda=60$nm, $\xi=5$nm, $(1-\frac{T}{T_c})=0.7$, $\frac{T}{T_c}$=0.3, $\mathbf{H}_e=1.5=1.5\sqrt{2}\mathbf{H}_c$. The vortices can seen in the areas where $|\psi|$ goes to 0. The magnetic flux vortices induced by the external field destroy superconductivity where they penetrate the sample. This sample is 20nm×20nm

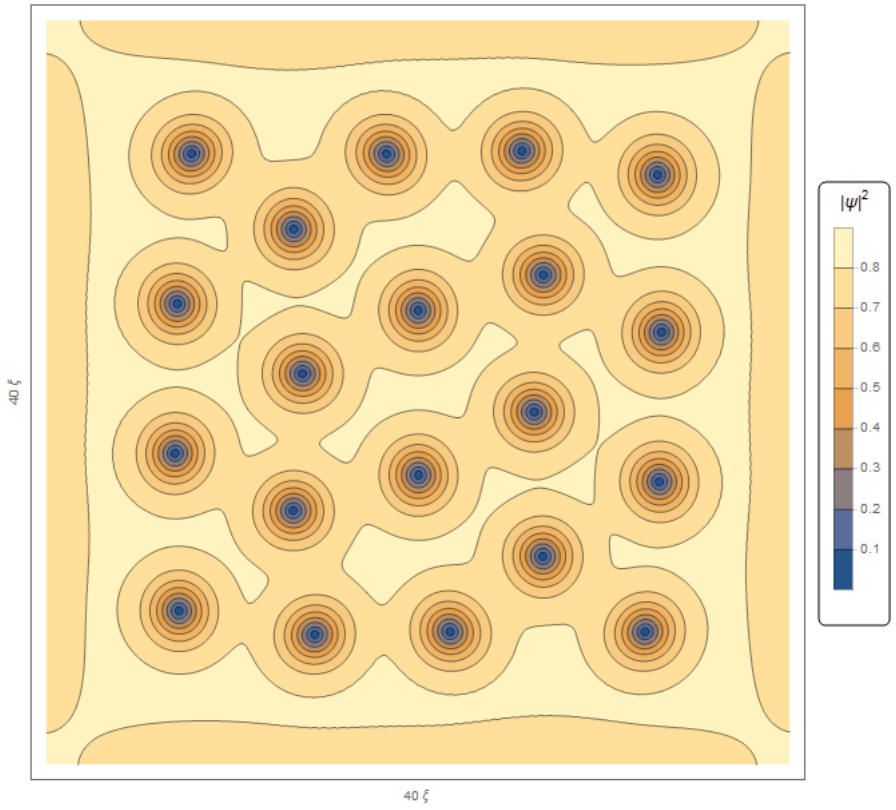

FIGURE 3.1: This figure shows the order parameter ψ in the steady state. The results are from the Time Dependent Ginzburg-Landau using finite element approximations.

3.2 Ginzburg Landau variants and modifications.

The Finite Element approximations of TDGL model are useful for examining the vortex dynamics of a Type II superconductor but the model is limited in some ways. The domain of validity for the temperature range is approximately $0.6T_c < T < T_c$, which can be shown by deriving the GL model from a pertubative calculation of the BCS theory [31]. The model is also limited to conventional isotropic materials with no applied currents. The model can modified to alleviate some of these limitations. The effective mass model was investigated by [8],[9], which uses an effective mass tensor to create anisotropy. Some new high temperature superconductors have multi-band behavior, as is the case for Magnesium Diboride [32]. Microscopically, there are multiple energy gaps with different band structures that give rise to superconductivity. A two-band model was derived by [33] and investigated [14]. Applying current to a superconducting sample is also of interest, since efficient movement of the electrical current is the defining property of superconductivity. Applied current for the one band case was investigated by [8] and for the two band case by [14]. Another interesting application for superconductors is the possibility of a powerful superconducting magnet. This can only be exhibited in Type II materials since the magnetic field penetrates them in the mixed state. Making a

superconductor a magnet is somewhat of a balancing act in practice. The applied current creates a (changing) magnetic field and with the magnetic field from neighboring metals or wires (essentially an external magnetic field) can destroy the superconductivity in the sample. This occurs when the changing magnetic field moves the vortices in the material. This creates Lorentz force that produces resistivity in the sample. However if the vortices can kept stationary, the superconductivity can persist throughout the sample. This is known as vortex pinning. In [8] the pinning effects for grain boundaries and normal sites were investigated using the one-band TDGL model. Grain boundaries are boundaries between cells where the material reorients and the anisotropy switches directions. Normal sites are where impurities have been placed in the sample. In the next few subsections, these various models are shown, and combined to try and model new high temperature materials such as Magnesium diboride.

3.2.1 The Effective Mass Model, Anisotropies, and Grains Boundaries

Many high temperature superconductors come with anisotropic properties such as directional dependent values for H_{c2}. This can captured by assuming the effective mass of the electron pairs is directional dependent. Following the methods of [8],[9], a mass tensor, $\mathbf{M}$ is used to replace m in the Ginzburg-Landau free energy. This variable mass also affects the characteristic lengths of the superconductor, ξ,λ. For the 3 dimensional case, $\mathbf{M}$ is,

$$\mathbf{M} = \begin{pmatrix} m_{\parallel} & 0 & 0 \\ 0 & m_{\parallel} & 0 \\ 0 & 0 & m_{\perp} \end{pmatrix} \tag{3.65}$$

Where $m_{\parallel}$ corresponds to the ab plane where the sample is isotropic in this plane. $m_{\perp}$ corresponds the the c plane where effective mass if different in this direction. In the two dimensional xy plane $\mathbf{M}$ reduces to,

$$\mathbf{M} = \begin{pmatrix} m_x & 0 \\ 0 & m_y \end{pmatrix} \tag{3.66}$$

Using the definitions of ξ and λ from Equations (3.27) and (3.29) for m_x and m_y respectively, we know how have 4 characteristic lengths: . The Ginzburg-Landau parameter κ is now defined as

$$\kappa = \frac{\lambda_x}{\xi_x} \tag{3.67}$$

The anisotropy of the model is characterized by the anisotropic parameters γ_x and γ_y which is the inverses of the effective mass in that direction

$$\gamma = \frac{m_x}{m_y} = (\frac{\lambda_x}{\lambda_y})^2 = (\frac{\xi_y}{\xi_x})^2 \tag{3.68}$$

The anisotropic mass tensor can be inserted into the dimensional Free energy from Equation (3.24), it becomes,

$$\begin{aligned} G = F_n + \int_\Omega \alpha(T)|\psi|^2 + \frac{1}{2}\beta(T)|\psi|^4 + \frac{1}{2}(-i\hbar\nabla - \frac{e^*}{c}\mathbf{A})^*\psi^* \cdot \mathbf{M}^{-1} \cdot (-i\hbar\nabla - \frac{e^*}{c}\mathbf{A})\psi \\ + \frac{|\mathbf{h} - \mathbf{H}_e|^2}{8\pi}\, d\Omega \end{aligned} \tag{3.69}$$

Non-dimensionalizing the free energy using the relations in (3.42) and ξ_x for ξ, λ_x for λ, yielding

$$G = F_n + \int_\Omega \frac{1}{2}(|\psi|^2 - \tau)^2 + |(\frac{\xi_x}{x_0}\frac{\partial}{\partial x} - \frac{x_0}{\lambda_x}A_y)\psi|^2 + \gamma|(\frac{\xi_x}{x_0}\frac{\partial}{\partial x} - \frac{x_0}{\lambda_x}A_y)\psi|^2 + \frac{|\mathbf{h} - \mathbf{H}_e|^2}{8\pi}\, d\Omega \tag{3.70}$$

Applying the variational method to find the minimizers, the anisotropic Ginzburg-Landau Equations (in the zero potential gauge) are

$$(\frac{\partial\psi}{\partial t}) + (|\psi|^2 - \tau)\psi + (-i\frac{\xi_x}{x_0}\frac{\partial}{\partial x} - \frac{x_0}{\lambda_x}A_x)^2\psi + \gamma(-i\frac{\xi_x}{x_0}\frac{\partial}{\partial y} - \frac{x_0}{\lambda_x}A_y)^2\psi = 0 \tag{3.71}$$

$$\begin{aligned} \sigma(\frac{1}{\lambda_x^2}\frac{\partial\mathbf{A}}{\partial t}) + \nabla\times\nabla\times\mathbf{A} + \{\frac{i}{2\kappa}(\psi\frac{\partial}{\partial x}\psi^* - \psi^*\frac{\partial}{\partial x}\psi) + \frac{x_0^2}{\lambda_x^2}|\psi|^2 A_x\} + \\ \gamma\{\frac{i}{2\kappa}(\psi\frac{\partial}{\partial y}\psi^* - \psi^*\frac{\partial}{\partial y}\psi) + \frac{x_0^2}{\lambda_x^2}|\psi|^2 A_y\} = \nabla\times\mathbf{H}_e \end{aligned} \tag{3.72}$$

$$\begin{aligned} \nabla\psi\cdot\mathbf{n} = 0, \;\; on \;\; \partial\Omega \;\; and \;\; \forall t \\ (\nabla\times\mathbf{A} - H_e)\times\mathbf{n} = 0, \;\; on \;\; \partial\Omega \;\; and \;\; \forall t \\ \mathbf{A}\cdot\mathbf{n} = 0, \;\; on \;\; \partial\Omega \;\; and \;\; \forall t \\ \nabla\cdot\mathbf{A}(\mathbf{x},0) = 0 \;\; \Omega \\ \psi(x,0) = \psi_0(x), \qquad \Omega \\ \mathbf{A}(x,0) = \mathbf{A}_0(x), \qquad \Omega \end{aligned} \tag{3.73}$$

Assuming the anisotropy is only in the y direction then ,$\gamma_x = 1$ and the the characteristic lengths are related by

$$\begin{aligned} \lambda_y^2 &= \frac{\gamma}{\lambda_x^2} \\ \xi_y^2 &= \gamma \xi_x^2 \end{aligned} \tag{3.74}$$

The anisotropy in the superconductor is most evident in the vortices seen in the order parameter. As previously mentioned at the end of Subsection 3.1.1 the vortices can be seen where ψ goes to zero in a radial manner in the superconductor . In the case of the anisotropic model the vortcies are now elliptical in shape, with ellipticity depending the values of γ_x and γ_y. The ratio of the x and y vortex lengths, l_x and l_y respectively, of the vortices is equal the square root of the ratio of the effective masses [8].

$$\frac{l_x}{l_y} = \sqrt{\frac{m_x}{m_y}} \tag{3.75}$$

In Figure 3.2 is an example of the order parameter ψ for $\lambda = 60$nm, $\xi = 5$nm, $(1 - \frac{T}{T_c}) = 0.7$, $\frac{T}{T_c}$=0.3, $\mathbf{H}_e = 1.5 = 1.5\sqrt{2}\mathbf{H}_c$ and $\gamma = \frac{1}{4}$. The vortices can seen in the areas where $|\psi|$ goes to 0. The vortices's are contracted in the y direction due to the anisotropy in the superconductor. This sample is $10nm \times 10$nm

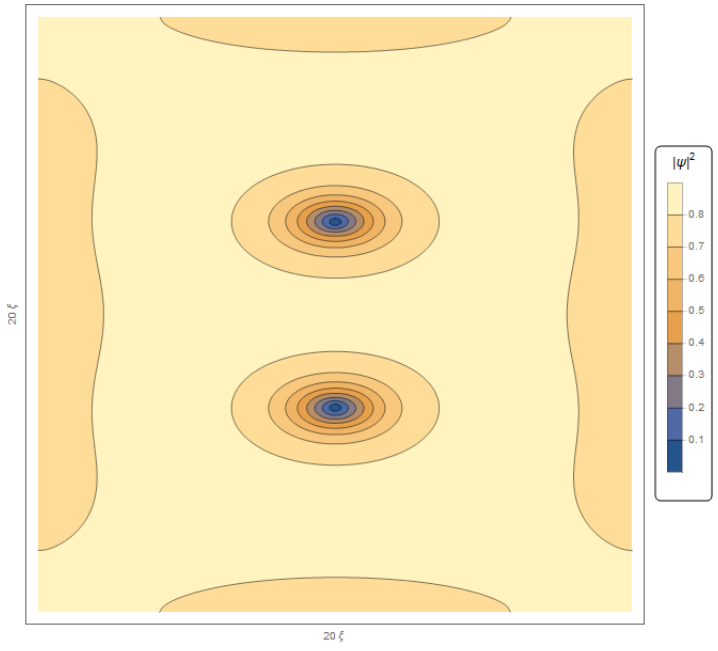

FIGURE 3.2: This figure shows the order parameter ψ in the steady steady state. There results are from the Anisotropic Time Dependent Ginzburg-Landau model using finite element approximations.

In materials with domain cells, there are boundaries where the anisotropy changes direction or value. There's are known as grain boundary and exist where a crystal structure reorients itself or where layers connect [8]. Grain boundaries can be easily included into the anisotropic Ginzburg-Landau by turning the constants γ_x and γ_y into functions of (x, y). In a numerical setting such as the Finite Element approximations, the effect of the grain boundary can be captured by deciding how the anisotropy will change from element to element. As a simple example, consider the functions $\gamma_x(x, y)$ and $\gamma_y(x, y)$ on a square domain, seen in Figure 3.3 . $\gamma_x(x, y) = \frac{1}{\gamma}$ for $x < y$ and 1 for $x > y$. Conversely $\gamma_y(x, y) = \frac{1}{\gamma}$ for $x > y$ and 1 for $x < y$. The anisotropy value changes as the $x = y$ line is crossed. When a magnetic vortcies crosses this grain boundary, it must shift its orientation. The process shifting of orientation creates a higher free energy than remaining on the boundary, depending on the specific magnetic field and current. This creates a pinning "force" on the vortices pins them to this boundary. These same pinning effects can be seen by introducing thin areas and normal sites into the sample[8],[10]. The normal site are introduced by locally setting $\alpha < 0$ on the site. Using the S-N boundary interfaces (the boundary condition in (3.28)), some of the superconducting electrons can leak into the normal site.

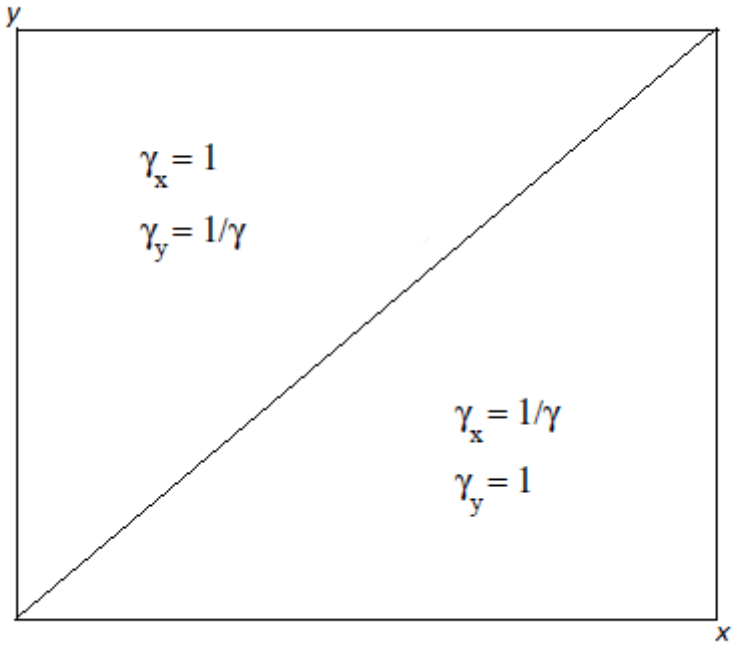

FIGURE 3.3: This figure shows a grain boundary across the diagonal of the sample. The anisotropy of the sample changes orientation across the grain boundary.

3.2.2 The Two Band TDGL model

Some superconducting materials contain multiple energy gaps responsible for the superconducting properties. This is somewhat typical in high temperature materials. In some materials such as MgB_2, the two band effects are very pronounced for lower temperatures while strong single band effects are seen near T_c[34]. This is because one of the bands in MgB_2 has weak second superconducting band that loses it's contribution as $T \to T_c$. Some of these two band materials are$NbSe_2$ and NbS_2 (with T_c of $7K$ and $6K$ respectively), some iron based superconductors such as $LaFeAsO$, and some cuprate based superconductors such as $YBa_2Cu_3O_6$ and $HgBa_2Ca_2Cu_2O_8$ (which has the highest T_c of $135K$ as of 2014) [35]. Many of these materials are also layered or highly anisotropic.

The Two band model captures the effects of two energy gaps by including a second order parameter ψ_2. Theses two bands are then coupled with Josephson coupling terms and coupling in the magnetic vector potential. The two band model was studied numerally using FEM were done by[14]. The model can be formed by including a second order parameter and necessary terms into the free energy.

$$G(\psi_1, \psi_2, \mathbf{A}) = \int_\Omega (f_1 + f_2 + f_{12} + f_m)\, d\Omega \tag{3.76}$$

with , for $\mu = 1, 2$

$$\tag{3.77}$$

$$f_\mu = \alpha_\mu(T)|\psi_\mu|^2 + \frac{1}{2}\beta_\mu(T)|\psi_\mu|^4 + \frac{1}{2m_\mu^*}|(-i\hbar\nabla_\mu - \frac{e^*}{c}\mathbf{A})\psi_\mu|^2 \tag{3.78}$$

$$f_{12} = \epsilon[\psi_1^*\psi_2 + \psi_1\psi_2^*] + \epsilon_1[(i\hbar\nabla_\mu - \frac{e^*}{c}\mathbf{A})\psi_1^*(-i\hbar\nabla_\mu - \frac{e^*}{c}\mathbf{A})\psi_2 + c.c.] \tag{3.79}$$

$$f_m = \frac{|\mathbf{h} - \mathbf{H}_e|^2}{8\pi} \tag{3.80}$$

Where $c.c$ is the complex conjugate of the accompanying term in the brackets. Like the one band model, the time dependence is captured by relating the variation in the free energy to the rate of return to equilibrium.

$$\Gamma(\frac{\partial\psi_1}{\partial t} + \frac{ie}{\hbar}\phi\psi_1) = -\frac{\delta F}{\delta\psi_{1*}} \tag{3.81}$$

$$\Gamma(\frac{\partial\psi_2}{\partial t} + \frac{ie}{\hbar}\phi\psi_2) = -\frac{\delta F}{\delta\psi_{2*}} \tag{3.82}$$

$$(\frac{1}{c}\frac{\partial\mathbf{A}}{\partial t} + \nabla\Phi) = -c\frac{\delta F}{\delta\psi_*} \tag{3.83}$$

Solving this variational problem give the Two Band Ginzburg-Landau Equations (separating the temperature dependence from α).

$$\Gamma_1(\frac{\partial\psi_1}{\partial t}+\frac{ie}{\hbar}\Phi\psi_1)+\alpha(1-\frac{T_1}{T_{c1}})\psi_1+\beta|\psi_1|^2\psi_1+\frac{1}{2m_1^*}(-i\hbar\nabla-\frac{e^*\mathbf{A}}{c})^2\psi_1$$
$$+\epsilon\psi_2+\epsilon_1(-i\hbar\nabla-\frac{e^*\mathbf{A}}{c})^2\psi_2=0$$

$$\Gamma_2(\frac{\partial\psi_2}{\partial t}+\frac{ie}{\hbar}\Phi\psi_2)+\alpha(1-\frac{T_2}{T_{c2}})\psi_2+\beta|\psi_2|^2\psi_2+\frac{1}{2m_2^*}(-i\hbar\nabla-\frac{e^*\mathbf{A}}{c})^2\psi_2$$
$$+\epsilon\psi_1+\epsilon_1(-i\hbar\nabla-\frac{e^*\mathbf{A}}{c})^2\psi_1=0$$

$$\begin{aligned}\frac{1}{4\pi}\nabla\times(\nabla\times\mathbf{A}-\mathbf{H})=\sigma_n(-\frac{1}{c}\frac{\partial A}{\partial t}-\nabla\Phi)+\frac{ie^*\hbar}{2m_1^*}(\psi_1\nabla\psi_1^*-\psi_1^*\nabla\psi_1)-\frac{e^{2*}}{m_1^*c}|\psi_1|^2\mathbf{A}\\ +\frac{-ie^*\hbar}{2m_2^*}(\psi_2\nabla\psi_2^*-\psi_2^*\nabla\psi_2)-\frac{e^{2*}}{m_2^*c}|\psi_2|^2\mathbf{A}\\ +\epsilon_1 i\hbar e^*(\psi_2\nabla\psi_1^*-\psi_2^*\nabla\psi_1+\psi_1\nabla\psi_2^*-\psi_1^*\nabla\psi_2)\\ -\epsilon_1\frac{2e^{*2}}{c}\mathbf{A}(\psi_1\psi_2^*+\psi_2\psi_1^*)\end{aligned} \tag{3.84}$$

with boundary and initial conditions

$$\begin{aligned}(\frac{1}{2m_1^*}(-i\hbar\nabla-\frac{e^*\mathbf{A}}{c})\psi_1+\epsilon_1(-i\hbar\nabla-\frac{e^*\mathbf{A}}{c})\psi_2)\cdot\mathbf{n}=0\quad on\quad\partial\Omega\times(0,t')\\ (\frac{1}{2m_2^*}(-i\hbar\nabla-\frac{e^*\mathbf{A}}{c})\psi_2+\epsilon_1(-i\hbar\nabla-\frac{e^*\mathbf{A}}{c})\psi_1)\cdot\mathbf{n}]=0\quad on\quad\partial\Omega\times(0,t')\\ (\nabla\times\mathbf{A})\times\mathbf{n}=\mathbf{H}_e\times\mathbf{n}\quad on\quad\partial\Omega\times(0,t')\\ \psi_1(x,y,0)=\psi_{1,0}(x,y)\quad on\quad\Omega\\ \psi_2(x,y,0)=\psi_{2,0}(x,y)\quad on\quad\Omega\\ \mathbf{A}(x,y,0)=A_0(x,y)\quad on\quad\Omega\end{aligned} \tag{3.85}$$

The above boundary conditions are the natural boundary conditions for the two band free energy functional. For a Normal Metal-Superconductor interface the boundary

conditions must be modified to be the De Gennes's boundary conditions,

$$\begin{aligned}
&(\frac{1}{2m_1^*}(-i\hbar\nabla - \frac{e^*\mathbf{A}}{c})\psi_1 \\
+\epsilon_1(-i\hbar\nabla - \frac{e^*\mathbf{A}}{c})\psi_2)\cdot\mathbf{n} &= (\zeta_1 i\frac{\hbar}{2m_1^*}\psi_1 + \zeta_2\eta_1 i\hbar\psi_1) \quad \text{on} \quad (\partial\Omega\times(0,t') \\
&\frac{1}{2m_2^*}(-i\hbar\nabla - \frac{e^*\mathbf{A}}{c})\psi_2 \\
+\epsilon_1(-i\hbar\nabla - \frac{e^*\mathbf{A}}{c})\psi_1)\cdot\mathbf{n} &= (\zeta_1 i\frac{\hbar}{2m_1^*}\psi_2 + \zeta_2\eta_1 i\hbar\psi_1) \quad \text{on} \quad \partial\Omega\times(0,t')
\end{aligned} \tag{3.86}$$

where $\zeta_1, \zeta_2 < 0$ and $\zeta_1 = \zeta_2$ to satisfy $\mathbf{J}_s\cdot\mathbf{n} = 0$ on $\partial\Omega$. These can made into the natural boundary conditions of the free energy functional by adding the additional term,

$$\int_{\partial\Omega}(\frac{\hbar^2}{2m_1^*}\zeta_1|\psi_1|^2 + \frac{\hbar^2}{2m_1^*}\zeta_2|\psi_2|^2) + \eta_1(\hbar^2\zeta_1\psi_1\psi_2^* + \hbar^2\zeta_1\psi_1^*\psi_2 + \hbar^2\zeta_2\psi_1\psi_2^* + \hbar^2\zeta_2\psi_1^*\psi_2)\,dS \tag{3.87}$$

Another possible set of S-N boundary conditions are

$$\begin{aligned}
&(\frac{1}{2m_1^*}(-i\hbar\nabla - \frac{e^*\mathbf{A}}{c})\psi_1 \\
+\epsilon_1(-i\hbar\nabla - \frac{e^*\mathbf{A}}{c})^2\psi_2)\cdot\mathbf{n} &= (\zeta_1 i\frac{\hbar}{2m_1^*}\psi_1 \quad \text{on} \quad \partial\Omega\times(0,t') \\
&(\frac{1}{2m_2^*}(-i\hbar\nabla - \frac{e^*\mathbf{A}}{c})\psi_2 \\
+\epsilon_1(-i\hbar\nabla - \frac{e^*\mathbf{A}}{c})^2\psi_1)\cdot\mathbf{n} &= (\zeta_1 i\frac{\hbar}{2m_1^*}\psi_2) \quad \text{on} \quad \partial\Omega\times(0,t')
\end{aligned} \tag{3.88}$$

which are obtained by adding the additional term to the free energy,

$$\int_{\partial\Omega}(\frac{\hbar^2}{2m_1^*}\zeta_1|\psi_1|^2 + \frac{\hbar^2}{2m_1^*}\zeta_2|\psi_2|^2)\,dS \tag{3.89}$$

The initial conditions are such that the superconducting sample is in near equilibrium, where $\psi_i = \psi_{\infty,i}$ and $\mathbf{A}_0 = 0$, when $\epsilon = 0$. In the case of inter-band interactions the interaction terms must be minimized. The Josephson interaction term can rewritten as

$$\int_\Omega \eta(\psi_1^*\psi_2 + \psi_1\psi_2^*)\,d\Omega = \int_\Omega \eta|\psi_1|^2|\psi_2|^2 cos(\theta_1 - \theta_2)\,d\Omega \tag{3.90}$$

where θ_i is the respective phase of the complex order parameter. For $\epsilon > 0$ the phase difference must be π and for $\epsilon < 0$ the phase difference must be 0. To accommodate this as well as the relative change in ψ_i with temperature, the initial values for the real and

imaginary parts are chosen to be,

$$\begin{aligned}
\psi_{1,R}(x,y,0) &= 0.8 sign(\epsilon)|(1-\frac{T}{T_{c,1}}) \\
\psi_{1,R}(x,y,0) &= 0.6 sign(\epsilon)|(1-\frac{T}{T_{c,1}}) \\
\psi_{1,R}(x,y,0) &= -0.8 sign(\epsilon)|(1-\frac{T}{T_{c,2}}) \\
\psi_{1,R}(x,y,0) &= -0.6 sign(\epsilon)|(1-\frac{T}{T_{c,2}})
\end{aligned} \tag{3.91}$$

The inter-band interactions are captured by the ϵ and ϵ_1 terms as well as the coupling the magnetic vector potential equation. The ϵ term is responsible for the Josephson like interactions, while the ϵ_1 term is responsible for the gradient coupling. There even more exotic coupling terms such as density-density coupling that couple the order parameters at higher powers [36]. Though this coupling may exist in some cases, the density-density term maybe incomplete and have accompanying terms when one derives the Extended Two Band equations from the perturbation theory of the BCS model [37].

The addition of a second superconducting band allows for some rather peculiar situations. The presence of two different critical temperatures, T_{c1} and T_{c2} allows for the possibility the operating the temperature to be below one bands critical temperature while being above the second critical temperature. Due to the Josephson like inter-band coupling, superconductivity is not destroyed in the second band. The effect is much like the proximity effect leaking superconducting electrons into normal sites (where $\alpha > 0$). Another new feature is the possibility of one band having Type I properties while the other has Type II properties. This is characterized by the band's Ginzburg-Landau parameter κ. Once again the inter-band interactions play strong role in the composite behavior of the two different bands. Strong enough coupling will induce weak vortices in the Type I band, even though this behavior is absent in the two band model. This also gives rise to the possibility of an intermediate type of superconductivity, fittingly named "Type 1.5" superconductivity. This type is characterized by hexagonal vortex patters that posses long range mutual attraction and short range repulsion[38]. This existence of this behavior is an ongoing debated and is not investigated in this research.

For computations the 2B-TDGL can non-dimensionalized using the following relations:

$$
\begin{gathered}
x = x_0\bar{x}, \qquad t = \bar{t}\frac{(-\alpha)}{\Gamma_1\hbar} \\
H_c = \sqrt{\frac{8\pi\alpha_1^2}{\beta_1}}, \quad \mathbf{A} = H_c x_0 \bar{\mathbf{A}} \\
\Phi = \frac{\hbar(-\alpha_1)}{2\Gamma_1 e^*}\bar{\Phi}, \quad \Gamma = \frac{\Gamma_1(-\alpha_1)}{\Gamma_2(-\alpha_2)} \\
\mathbf{H} = \sqrt{2}H_c\bar{\mathbf{H}} \qquad \psi_i = \sqrt{\frac{-\alpha_i}{\beta_i}}\bar{\psi}_i \\
\lambda_i = \sqrt{-\frac{c^2 m_i^*\beta_i}{4\pi e^{*2}\alpha_i}}, \qquad \xi_i = \sqrt{-\frac{\hbar^2}{2m_i^*\alpha_i}} \\
\kappa_i = \sqrt{\frac{c^2 m_i^*\beta_i}{2\pi e^{*2}\hbar^2}} \quad \nu = \frac{\lambda_2\xi_2}{\lambda_1\xi_1} \\
\eta = \eta\sqrt{\frac{\beta_1\alpha_2}{\beta_2\alpha_1}}\frac{1}{\alpha_1} \quad \eta_1 = \epsilon_1 2\sqrt{m_1^* m_2^*} \\
\sigma = \frac{\sigma_n m_1^*\beta_!}{\Gamma_1 e^{*2}}
\end{gathered}
\tag{3.92}
$$

The non-dimensionlized 2B-TDGL Equations are (with the bars dropped),

$$
\begin{gathered}
(\frac{\partial\psi_1}{\partial t} + i\Phi\psi_1) + (|\psi_1|^2 - \tau_1)\psi_1 + (-i\frac{\xi_1}{x_0}\nabla - \frac{x_o}{\lambda_1}\mathbf{A})^2\psi_1 \\
+\eta\psi_2 + \eta_1\frac{\xi_1}{\nu\xi_2}(-i\frac{\xi_2}{x_0}\nabla - \nu\frac{x_o}{\lambda_2}\mathbf{A})^2\psi_2 = 0
\end{gathered}
$$

$$
\begin{gathered}
\Gamma(\frac{\partial\psi_2}{\partial t} + i\Phi\psi_2) + (|\psi_2|^2 - \tau_2)\psi_2 + (-i\frac{\xi_1}{x_0}\nabla - \nu\frac{x_o}{\lambda_1}\mathbf{A})^2\psi_2 \\
+\eta\psi_1 + \eta_1\nu\frac{\xi_2}{\xi_1}(-i\frac{\xi_1}{x_0}\nabla - \frac{x_o}{\lambda_1}\mathbf{A})^2\psi_1 = 0
\end{gathered}
$$

$$
\begin{gathered}
\nabla\times(\nabla\times\mathbf{A} - \mathbf{H}) = \sigma(-\frac{x_o^2}{\lambda_1^2}\frac{\partial A}{\partial t} - \frac{1}{\kappa_1}\nabla\Phi) + i\frac{1}{\kappa_1}(\psi_1\nabla\psi_1^* - \psi_1^*\nabla\psi_1) - \frac{x_0^2}{\lambda_1}|\psi_1|^2\mathbf{A} \\
+i\frac{1}{2\kappa_2\nu}(\psi_2\nabla\psi_2^* - \psi_2^*\nabla\psi_2) - \frac{x_0^2}{\lambda_2}|\psi_2|^2\mathbf{A} \\
+i\eta_1\frac{\xi_1}{2\lambda_2}(\psi_2\nabla\psi_1^* - \psi_2^*\nabla\psi_1 + \psi_1\nabla\psi_2^* - \psi_1^*\nabla\psi_2) \\
-\eta_1\frac{x_0^2}{\lambda_1\lambda_2}\mathbf{A}(\psi_1\psi_2^* + \psi_2\psi_1^*)
\end{gathered}
\tag{3.93}
$$

and non-dimensionalized boundary and initial conditions,

$$\begin{gathered}((-i\frac{\xi_1}{x_0}\nabla-\frac{x_o}{\lambda_1}\mathbf{A})\psi_1+\eta_1\frac{1}{\nu}(-i\frac{\xi_1}{x_0}\nabla-\nu\frac{x_o}{\lambda_1}\mathbf{A})\psi_2)\cdot\mathbf{n}=i\zeta_1\frac{\xi_1}{x_0}\psi_1 \quad on \quad \partial\Omega\times(0,t')\\ ((-i\frac{\xi_1}{x_0}\nabla-\nu\frac{x_o}{\lambda_1}\mathbf{A})\psi_2+\eta_1\nu(-i\frac{\xi_1}{x_0}\nabla-\frac{x_o}{\lambda_1}\mathbf{A})\psi_1)\cdot\mathbf{n}=i\zeta_2\frac{\xi_2}{x_0}\psi_2 \quad on \quad \partial\Omega\times(0,t')\\ (\nabla\times\mathbf{A})\times\mathbf{n}=\mathbf{H}_e\times\mathbf{n} \quad on \quad \partial\Omega\times(0,t')\\ \psi_1(x,y,0)=\psi_{1,0}(x,y) \quad on \quad \Omega\\ \psi_2(x,y,0)=\psi_{2,0}(x,y) \quad on \quad \Omega\\ \mathbf{A}(x,y,0)=A_0(x,y) \quad on \quad \Omega\end{gathered} \tag{3.94}$$

3.2.3 Applied Current in the 2B-TDGL

One of a superconductors defining features is zero electrical resistance, along with Meissner effect. The property of zero resistance can taken advantage of by applying a current to the superconductor for efficient transportation. In type two superconductors, efficient superconducting magnetics can be made [39]. The applied current variant was shown for the one band case in [8] and derived for the two band model in [14]. Here we limit ourselves to the two band version, which analogous to the one band version. The effects of the applied current density $\mathbf{J}_a$ can be captured by gauging the system in this way to include the current. This can be done by modifying the zero electric potential gauge. Consider the gauge transformation,

$$(\psi_1,\psi_2,\bar{\mathbf{A}},\Phi)=G_\chi(\psi_1e^{i\kappa_1\chi},\psi_2e^{i\kappa_2\chi},\mathbf{B},\phi) \tag{3.95}$$

with $\bar{\mathbf{A}}=\mathbf{B}+\frac{\lambda_1^2}{x_0^2}\nabla\chi$ and $\Phi=\phi-\kappa_1-\frac{\partial\chi}{\partial t}$, and χ solves the following problem.

$$\begin{gathered}\frac{\partial\chi}{\partial t}=\phi-\Phi \quad on \quad \Omega\\ \nabla\cdot\mathbf{n}=-\mathbf{B}\cdot\mathbf{n} \quad on \quad \partial\Omega\\ -\Delta\chi=\nabla\cdot\mathbf{B} \quad on \quad \Omega \quad and \quad t=0\end{gathered} \tag{3.96}$$

This produces the same boundary and initial conditions as the zero potential gauge, but now $\Phi=\Phi_a$. Looking at the electrical field, $\mathbf{E}_a$, produced by the applied current on the boundary ,

$$\mathbf{J}_a=\sigma\mathbf{E}_a=-\sigma(\frac{x_o^2}{\lambda_1^2}\frac{\partial\mathbf{A}_a}{\partial t}+\frac{1}{\kappa_1}\nabla\Phi_a) \tag{3.97}$$

Using the Helmholtz decomposition on the applied current density [14], Laplace's equation is made with boundary conditions.

$$\begin{aligned} \Delta\Phi_a(t) = 0 \quad on \quad \Omega \\ \frac{\partial \phi_a(t)}{\partial n} = -\frac{\kappa_1}{\sigma}\mathbf{J}_a \cdot \mathbf{n} \quad on \quad \partial\Omega \end{aligned} \tag{3.98}$$

From the gauge transformation $\mathbf{A}$ now becomes $\bar{\mathbf{A}} = \mathbf{A} + \mathbf{A}_a$ and the S-N boundary conditions are required since the superconductor in now in electrical contact with a normal metal carrying the current to the sample. The 2B-TDGL in the current gauge become.

$$\begin{aligned} \Gamma_1(\frac{\partial \psi_1}{\partial t} + \frac{ie}{\hbar}\Phi_a\psi_1) + \alpha(1 - \frac{T_1}{T_{c1}})\psi_1 + \beta|\psi_1|^2\psi_1 + \frac{1}{2m_1^*}(-i\hbar\nabla - \frac{e^*\mathbf{A}}{c})^2\psi_1 \\ +\epsilon\psi_2 + \epsilon_1(-i\hbar\nabla - \frac{e^*\mathbf{A}}{c})^2\psi_2 = 0 \end{aligned}$$

$$\begin{aligned} \Gamma_2(\frac{\partial \psi_2}{\partial t} + \frac{ie}{\hbar}\Phi_a\psi_2) + \alpha(1 - \frac{T_2}{T_{c2}})\psi_2 + \beta|\psi_2|^2\psi_2 + \frac{1}{2m_2^*}(-i\hbar\nabla - \frac{e^*\mathbf{A}}{c})^2\psi_2 \\ +\epsilon\psi_1 + \epsilon_1(-i\hbar\nabla - \frac{e^*\mathbf{A}}{c})^2\psi_1 = 0 \end{aligned}$$

$$\begin{aligned} \frac{1}{4\pi}\nabla \times (\nabla \times \mathbf{A} - \mathbf{H}) = \sigma_n(-\frac{1}{c}\frac{\partial A}{\partial t} - \nabla\Phi_a) + \frac{ie^*\hbar}{2m_1^*}(\psi_1\nabla\psi_1^* - \psi_1^*\nabla\psi_1) - \frac{e^{2*}}{m_1^*c}|\psi_1|^2\mathbf{A} \\ +\frac{-ie^*\hbar}{2m_2^*}(\psi_2\nabla\psi_2^* - \psi_2^*\nabla\psi_2) - \frac{e^{2*}}{m_2^*c}|\psi_2|^2\mathbf{A} \end{aligned} \tag{3.99}$$

If $\mathbf{J}_a$ is defined in the y direction, being applied on the x boundaries, Φ_a can be found using,

$$\mathbf{J}_a(t) = -\frac{\sigma}{\kappa}\nabla\Phi_a(t) \tag{3.100}$$

Yielding,

$$\Phi_a = -\frac{\kappa_1}{\sigma}J_a y \tag{3.101}$$

This value is inserted into the ψ equations as Type-A current. As for the magnetic vector potential equation the current density $\mathbf{J}_a(t)$ is inserted in place of $-\frac{\sigma}{\kappa}\nabla\Phi_a(t)$. In this equation the current can be related to the magnetic field induced by the current by,

$$\mathbf{J}_a(t) = \nabla \times \mathbf{H}_a \tag{3.102}$$

yielding the field,

$$\mathbf{H} = -J_a(x - \frac{x_0}{2})\hat{z} \tag{3.103}$$

Now the non-dimensionalized 2B-TDGL equations with the applied current become

$$(\frac{\partial\psi_1}{\partial t} - i\frac{\kappa_1}{\sigma}(J_a y)\psi_1) + (|\psi_1|^2 - \tau_1)\psi_1 + (-i\frac{\xi_1}{x_0}\nabla - \frac{x_o}{\lambda_1}\mathbf{A})^2\psi_1 + \eta\psi_2 + \eta_1\frac{\xi_1}{\nu\xi_2}(-i\frac{\xi_2}{x_0}\nabla - \nu\frac{x_o}{\lambda_2}\mathbf{A})^2\psi_2 = 0$$

$$\Gamma(\frac{\partial\psi_2}{\partial t} - i\frac{\kappa_1}{\sigma}(J_a y)\psi_2) + (|\psi_2|^2 - \tau_2)\psi_2 + (-i\frac{\xi_1}{x_0}\nabla - \nu\frac{x_o}{\lambda_1}\mathbf{A})^2\psi_2 + \eta\psi_1 + \eta_1\nu\frac{\xi_2}{\xi_1}(-i\frac{\xi_1}{x_0}\nabla - \frac{x_o}{\lambda_1}\mathbf{A})^2\psi_1 = 0$$

$$\begin{aligned}\nabla\times(\nabla\times\mathbf{A} - \mathbf{H} + (J_a[x - \frac{x_0}{2}])) = \sigma(-\frac{x_o^2}{\lambda_1^2}\frac{\partial A}{\partial t}) + i\frac{1}{\kappa_1}(\psi_1\nabla\psi_1^* - \psi_1^*\nabla\psi_1) - \frac{x_0^2}{\lambda_1}|\psi_1|^2\mathbf{A} \\ +i\frac{1}{2\kappa_2\nu}(\psi_2\nabla\psi_2^* - \psi_2^*\nabla\psi_2) - \frac{x_0^2}{\lambda_2}|\psi_2|^2\mathbf{A} \\ +i\eta_1 i\frac{\xi_1}{2\lambda_2}(\psi_2\nabla\psi_1^* - \psi_2^*\nabla\psi_1 + \psi_1\nabla\psi_2^* - \psi_1^*\nabla\psi_2) \\ -\eta_1\frac{x_0^2}{\lambda_1\lambda_2}\mathbf{A}(\psi_1\psi_2^* + \psi_2\psi_1^*)\end{aligned} \tag{3.104}$$

Where the J_a terms are applied on the boundary with current leads on the sample, in this case the x boundaries.

Chapter 4

Modeling Magnesium Diboride

4.1 Magnesium Diboride

Magnesium diboride or MgB_2 is a ceramic material that had been previously considered a bad conductor. However, in 2001 Japanese physicists discovered superconducting properties in MgB_2 below 39K. The discovery of superconducting properties led to a large spike in interest of the material. By the end of 2001 highly clean samples were developed [32] to give better insight into how exactly the superconductivity manifested in MgB_2. First some of structural properties of magnesium diboride are reviewed before discussing the superconducting properties. MgB_2 is a layered material that consists of alternating layers of graphite type structures of boron and closely packed magnesium layers [40]. As a result of this structure, calculations have shown that MgB_2 has four bands crossing the Fermi energy, producing four disconnected Fermi sheets. Two of these bands are from from the boron's p_z orbitals, known as the π bands. The boron's p_x and p_y orbitals from the other two bands known as the σ bands.

Recent analysis of MgB_2 has shown that this material posseses many odd properties not seen with other conventional superconductors. The upper critical field, H_{c2} has a strong anisotropy, meaning the field strength necessary to destroy the superconducting effects is dependent on which plane it is aligned with[34]. H_{c2} in the ab plane also has a very strong dependence on the inverse temperature as seen in [34]. Furthermore, the anisotropic parameter $\gamma = \frac{H_{c2}^{ab}}{H_{c2}^{c}}$, is highly temperature dependent, ranging from $\gamma = 5$ near $T = 0$ to $\gamma = 2$ near $T = T_c$. One would expect that this same anisotropic behavior would persist in the lower critical field H_{c1}. However the anisotropy in the lower critical field was found to increase with temperature while the upper critical fields anisotropy decreased with increasing temperature[32]. This has led many authors to believe that

MgB_2 maybe better described by a multi-band theory such as the 2BTDGL. Some authors, such as[34], have shown the two band model captures the upward curvature upper critical field in a much larger temperature domain than the single band model.

Magnesium diboride comes with many novel properties that make it an ideal superconductor for practical applications. Its critical temperature is 39K which avoids the use of expensive liquid helium to cool samples. It is a very inexpensive material compared to optimally doped cuprate superconductors. It has a rather high critical current and upper critical field. Futhermore, MgB_2 possesses clean grain boundaries that do not impede applied current while pinning vortices to keep the superconducting properties from collapsing[31]. The upper critical field in MgB_2 near $T = 0$K were found to be 14T in the ab planes and 3T in the c plane[41]. The same author found the critical currents to range from 10^5 A/m^2 at 20T to 10^9 A/cm^2 at 10K. The σ and π bands are the electron bands responsible for the superconducting properties in MgB_2. The main mechanism of the superconductivity is conventional s-wave photon-electron interactions, stronger in the σ band[38]. This gives rise to two energy gaps of Δ_σ 7meV and Δ_π 7meV. The π band is the weak interacting band but its effects are very important. The π minimizes impurity and inter-band scattering, and its coupling effects with the stronger σ band produce many of the odd effects seen in it magnetic properties.

4.2 Modeling MgB_2

Many authors have explored methods to increase the critical current. Some of these include doping, tuning the magnetic field strength, and different preparation methods to make the material [41]. Most of these methods are conducted experimentally or involve lengthy analysis. No extensive numerical studies of the vortex dynamics in MgB_2 using FEM have been done. Numerical studies are a good setting to make qualitative and quantitative predictions about a material. Numerical studies are inexpensive and easy to modify compared to their experimental counterparts. The validity of the numerical studies depends on the validity of the model used. Even if the results are only correct in an approximate sense, they can give the experimentalist a good sense of what is going on in a material before a lengthy and costly experiment is done.

The 2BTDGL derived from the BCS (which coincides with the model in Chapter 3) has been shown to accurately reproduce the odd behavior of the upper critical field [34]. Also, the same authors showed that the 2BTDGL has a temperature range of validity

down to around 30K in MgB_2. In this research a variant of the GL model is used for numerical studies of Magnesium Diboride. The model parameters are those for a clean sample of MgB_2 gotten from the experimental data and fitted using the BCS model. Using a GL variant is much simpler than modeling a full BCS type theory while still producing reliable results.

4.2.1 The Anisotropic 2B-TDGL with applied current

To properly capture the properties of magnesium diboride, the parameters for each band must be investigated. In [38] and [41], the parameters for each band can be found, shown in Table 4.1. To accommodate these parameters, the anisotropic GL model can

Table 4.1

$\xi_\sigma(0) = 13$ nm	$\lambda_\sigma(0) = 47.81$ nm	$\kappa_\sigma = 3.68$
$\xi_\pi(0) = 51$ nm	$\lambda_\pi(0) = 33.6$ nm	$\kappa_\pi = 0.66$
T_c=39 K	$T_{c,\sigma}$=35.6 K	$T_{c,\pi}$=11.8 K
$\gamma_\sigma = 4.55$	$\gamma_\pi = 1$	T=30 K

TABLE 4.1: These are the parameters for a clean sample MgB_2.

be combined with the two band model to capture the anisotropy in the σ band. An effective mass tensor can be implemented for the ψ_1 equation, representing the σ band. The anisotropic 2BTDGL with applied current is:

$$\begin{aligned}
&(\frac{\partial\psi_1}{\partial t} - i\frac{\kappa_1}{\sigma}(J_a y)\psi_1) + (|\psi_1|^2 - \tau_1)\psi_1 + (-i\frac{\xi_1}{x_0}\nabla - \frac{x_o}{\lambda_1}\mathbf{A})\cdot\boldsymbol{\gamma}\cdot(-i\frac{\xi_1}{x_0}\nabla - \frac{x_o}{\lambda_1}\mathbf{A})\psi_1 \\
&+\eta\psi_2 + \eta_1\frac{\xi_1}{\nu\xi_2}(-i\frac{\xi_2}{x_0}\nabla - \nu\frac{x_o}{\lambda_2}\mathbf{A})\cdot\boldsymbol{\gamma}\cdot(-i\frac{\xi_2}{x_0}\nabla - \nu\frac{x_o}{\lambda_2}\mathbf{A})\psi_2 = 0
\end{aligned}$$

$$\begin{aligned}
&\Gamma(\frac{\partial\psi_2}{\partial t} - i\frac{\kappa_1}{\sigma}(J_a y)\psi_2) + (|\psi_2|^2 - \tau_2)\psi_2 + (-i\frac{\xi_1}{x_0}\nabla - \nu\frac{x_o}{\lambda_1}\mathbf{A})^2\psi_2 \\
&+\eta\psi_1 + \eta_1\nu\frac{\xi_2}{\xi_1}(-i\frac{\xi_1}{x_0}\nabla - \frac{x_o}{\lambda_1}\mathbf{A})\boldsymbol{\gamma}\cdot(-i\frac{\xi_1}{x_0}\nabla - \frac{x_o}{\lambda_1}\mathbf{A})\psi_1 = 0
\end{aligned}$$

$$\begin{aligned}
\nabla\times(\nabla\times\mathbf{A} - \mathbf{H} + (J_a[x - \frac{x_0}{2}])) &= \sigma(-\frac{x_o^2}{\lambda_1^2}\frac{\partial A}{\partial t}) + i\frac{1}{\kappa_1}\boldsymbol{\gamma}\cdot(\psi_1\nabla\psi_1^* - \psi_1^*\nabla\psi_1) - \frac{x_0^2}{\lambda_1}|\psi_1|^2\mathbf{A} \\
&+i\frac{1}{2\kappa_2\nu}(\psi_2\nabla\psi_2^* - \psi_2^*\nabla\psi_2) - \frac{x_0^2}{\lambda_2}|\psi_2|^2\mathbf{A} \\
&+i\eta_1 i\frac{\xi_1}{2\lambda_2}\boldsymbol{\gamma}\cdot(\psi_2\nabla\psi_1^* - \psi_2^*\nabla\psi_1 + \psi_1\nabla\psi_2^* - \psi_1^*\nabla\psi_2) \\
&-\eta_1\frac{x_0^2}{\lambda_1\lambda_2}\boldsymbol{\gamma}\cdot\mathbf{A}(\psi_1\psi_2^* + \psi_2\psi_1^*)
\end{aligned} \tag{4.1}$$

where the S-N boundary conditions are used since the superconducting sample is in electrical contact with the normal metal carrying the applied current. To include the natural boundary conditions, the method in Chapter 2 can applied to the system to produce the weak from and thus a suitable model for FEM approximations. Some of notation has been simplified by using $\mathbf{D}_i$ as the gauge invariant derivative and using $\mathscr{R}$ to extract the real part of a term. The weak problem of the model above is stated as seek $\psi_1 \in V$,$\psi_2 \in V$ and $\mathbf{A} \in \mathbf{Z}$

$$\begin{aligned}\int_\Omega \frac{\partial \psi_1}{\partial t}\tilde{\psi} - i\frac{\kappa_1}{\sigma}J_a y\psi_1\tilde{\psi} + (|\psi_1|^2 - \tau_1)\psi_1\tilde{\psi} + \mathbf{D}_1\psi_1 \cdot \boldsymbol{\gamma} \cdot \mathbf{D}_1\tilde{\psi_1} + \eta\psi_2\tilde{\psi} \\ +\eta_1\frac{\xi_1}{\nu\xi_2}\mathbf{D}_2\psi_2 \cdot \boldsymbol{\gamma} \cdot \mathbf{D}_2\tilde{\psi}\, d\Omega = -\int_{\partial\Omega}\zeta_1\frac{\xi_1^2}{x_0}\psi_1\tilde{\psi}\, dS \quad \forall\tilde{\psi_1} \in V\end{aligned} \tag{4.2}$$

$$\begin{aligned}\int_\Omega \Gamma\frac{\partial \psi_2}{\partial t}\tilde{\psi} - i\frac{\kappa_1}{\sigma}J_a y\psi_1\tilde{\psi_2} + (|\psi_2|^2 - \tau_2)\psi_2\tilde{\psi} + \mathbf{D}_2\psi_2 \cdot \mathbf{D}_2\tilde{\psi} + \eta\psi_1\tilde{\psi} \\ +\eta_1\frac{\xi_2}{\xi_1}\mathbf{D}_1\psi_1 \cdot \boldsymbol{\gamma} \cdot \mathbf{D}_1\tilde{\psi}\, d\Omega = -\int_{\partial\Omega}\zeta_2\frac{\xi_2^2}{x_0}\psi_2\tilde{\psi}\, dS \quad \forall\tilde{\psi_2} \in V\end{aligned} \tag{4.3}$$

$$\begin{aligned}\int_\Omega \sigma\frac{x_o^2}{\lambda_1^2}\frac{\partial \mathbf{A}}{\partial t}\tilde{\mathbf{A}} + \eta(\nabla\cdot\mathbf{A})\cdot(\nabla\cdot\tilde{\mathbf{A}}) + (\nabla\times\mathbf{A})\cdot(\nabla\times\tilde{\mathbf{A}}) + \mathscr{R}\{i\frac{1}{\kappa_1}(\boldsymbol{\gamma}\cdot\nabla\psi_1)\cdot\psi_1\cdot\tilde{\mathbf{A}}\} + \frac{x_0^2}{\lambda_1^2}|\psi_1|^2\boldsymbol{\gamma}\cdot\mathbf{A}\cdot\tilde{\mathbf{A}} \\ +\mathscr{R}\{i\frac{1}{\nu\kappa_1}(\nabla\psi_2)\cdot\psi_2\tilde{\mathbf{A}}\} + \frac{x_0^2}{\lambda_2^2}|\psi_2|^2\mathbf{A}\cdot\tilde{\mathbf{A}} + \eta_1\boldsymbol{\gamma}\cdot(\mathscr{R}\{i\frac{\xi_1}{\lambda_2}(\cdot\nabla\psi_1)\cdot\psi_2\tilde{\mathbf{A}}\} + \mathscr{R}\{i\frac{\xi_1}{\lambda_2}(\cdot\nabla\psi_2)\cdot\psi_1\tilde{\mathbf{A}}\}) \\ +\eta_1\frac{x_0}{\lambda_1\lambda_2}\boldsymbol{\gamma}\cdot\{(\psi_1\psi_2^* + \psi_2\psi_1^*)\mathbf{A}\cdot\tilde{\mathbf{A}}\}\, d\Omega = \int_\Omega(\mathbf{H}_e - J_a(x - \frac{x_0}{2}\hat{(z)}))\cdot(\nabla\times\tilde{\mathbf{A}})\, d\Omega \\ \forall\tilde{\mathbf{A}} \in \mathbf{Z}\end{aligned} \tag{4.4}$$

With

$$\boldsymbol{\gamma} = \begin{pmatrix}\frac{1}{\gamma_x(x,y)} & 0\\ 0 & \frac{1}{\gamma_y(x,y)}\end{pmatrix},\quad \tau_i = 1 - \frac{T}{T_{c,i}},\quad \nu = (\frac{\lambda_2(0)\xi_1(0)}{\lambda_1(0)\xi_2(0)}),\ \mathbf{D}_1 = (-i\frac{\xi_1}{x_0}\nabla - \frac{x_0}{\lambda_1}\mathbf{A}),$$
$$\mathbf{D}_2 = (-i\frac{\xi_2}{x_0}\nabla - \nu\frac{x_0}{\lambda_2}\mathbf{A})$$

Some modifications from Chapters 2 and 3 can been seen. This is the weak form of the two band model with Josephson coupling (η) and inter-gradient coupling (η_1). An effective mass is included by using the $\boldsymbol{\gamma}$ tensor for ψ_1. This captures the anisotropy in the σ band as shown in Table 4.1. The value of γ in the tensor is shown as a function to represent grain boundaries where the γ value flips across the diagonal ($x = y$). An artificial term $\eta(\nabla\cdot\mathbf{A})\cdot(\nabla\cdot\tilde{\mathbf{A}})$ term is used to improve the stability of the numerical method as in [14]. In these papers, it was shown that this additional term does not

affect the evolution or steady state of the solution.

This is the model used in this research to study vortex dynamics and ways to increase the critical current in MgB_2. Specifically the effects of the relatively unknown coupling parameter η on the critical current are investigated with grain boundaries. Although the coupling parameters are not known well, they play a strong role in the critical current value. In [42] the (relative) effective London penetration depth $\lambda_L(T)$, for a two band superconductor is shown to have a non linear dependence on the coupling parameters η and η_1. Furthermore, in [36], the relative critical current was found to be $\mathbf{J}_c = \frac{\lambda_L^2(0)}{\lambda_L^2(T)}(\mathbf{H}_{c2})^{\frac{1}{2}}$. This shows that the critical current is also dependent on the coupling parameters η and η_1. To avoid lengthly analysis of this non linear relations under different parameters, numerical studies can be done to give insight into the effects of the coupling parameters. These studies can be used to help pin the exact values of the coupling parameters by comparing the numerical results to experiment. The numerical studies can also be used to study improvements in the critical current. If a certain value is seen to improve the critical current, experimentalists can look for a physical mechanism to tune this parameter, such as doping or particular preparation methods.

Another feature to be studied is the effect of grain boundaries in addition to the coupling parameters. Specifically clean grain boundaries where the crystal structure reorients itself are included. These are contained in MgB_2 and do not impede super currents [39]. However grain boundaries do impede the movement of magnetic vortices, which increases the critical current. When a current is applied to a superconductor, it creates a non-uniform magnetic field in the sample that induces the movement of the vortices. If the vortices move enough they will combine to make the sample into a large normal site and destroy superconductivity. Impeding the movement of vortices can dramatically improve the critical current in a superconductor. From [41], the depinning current, $\mathbf{J}_d$ needed to move a magnetic vortex is

$$\mathbf{J}_d = \frac{\mathbf{\Phi_0}}{3\sqrt{3}\pi\lambda^2\xi\mu_0} \tag{4.5}$$

where $\mathbf{\Phi_0}$ is the magnetic quantum flux and μ_0 is the permeability of free space. The coherence length and penetration can taken from the dominant band (the σ band for ψ_1) and the temperature dependences separated from them using (3.34). For characteristic lengths and $T = 30$K this gives, $\mathbf{J}_d = 8.68 \times 10^8$ A/m^2. Conversely to pin the vortex, a pinning force of $Fp = \mathbf{J} \times \mu_0\mathbf{H}$, where $\mathbf{H}$ is magnetic field in the sample, is needed to pin the vortices. In [43] this relation is reduced to

$$F_p = H_{c2}^m f(h) \quad h = \frac{H}{H_{c2}} \tag{4.6}$$

with

$$f(h) \propto h^p(1-h)^q \tag{4.7}$$

and $p = \frac{1}{2}$, $q = 2$ for grain boundary pinning

In [43], [39] and[44] flux pinning and grain boundary pinning are investigated experimentally or analytically. The lack of numerical studies leaves a gap between these two efforts. The experimentalists have a very good insight into the effective properties of the two bands as well as large scale vortex dynamics [38], but these experiments have trouble resolving the effects from the individual bands as well as how the vortices evolve. The theorists have great insight into the microscopic effects of each band and how they produce macroscopic properties like J_c and $H_{c1,c2}$, but these relations used are too cumbersome to produce an efficient numeral model. The Ginzburg-Landau theory provides a mesoscopic resolution that bridges the gap between these two extremes. Furthermore numerical studies provide an illustrative insight into vortex dynamics while avoiding lengthy analysis.

4.3 The Effects of Coupling Parameters and Grain Boundaries on $\mathbf{J}_c$ in $\mathbf{MgB}_2$

To investigate the effect of the coupling parameters and grain boundaries on the critical current, a series of numerical studies was done with various parameter sets. The key to these numerical studies is to find trends in the solutions while avoiding lengthy calculations. The non-dimensionalized values can be returned to the dimensionalied values and tell experimentalists how to tune their experiments to investigate the desired phenomena seen in the numeral studies. Below some numerical studies are done using FEM to find the order parameter value ψ and thus study the vortex dynamics. The parameters are chosen to be those of the magnesium diboride, givin in Table 4.1

For all the studies the operating temperature is taken to be 31K. This specific temperature was chosen for several reasons. Firstly and most importantly, the temperature must stay within the validity of the GL theory for a clean sample, given in [34]. Secondly to take advantage of practicality of the high T_c, results are found at a temperature near T_c, where it is more inexpensive to maintain this temperature (as opposed to 0K). The applied field $\mathbf{H}_e$ is taken in the z direction and uniform. As shown in [45], $\mathbf{J}_c$ grows sharply with a decrease in $\mathbf{H}_e$ below 3T for $T = 30$K. In these studies, the field is kept relatively low to try and maximize $\mathbf{J}_c$. The applied current is taken to be in the

y direction with the leads on the x boundaries. The applied current is of the form

$$\begin{aligned} \mathbf{J}_a &= J_a \sin(\omega t)\hat{y} \quad on \quad (\partial\Omega)_x \\ \mathbf{J}_a &= 0 \quad on \quad (\partial\Omega)_y \end{aligned} \tag{4.8}$$

where ω is the angular frequency of the sine wave, $(\partial\Omega)_x$ is the x boundaries at $y = 0$ and $y = L$, where L is the length of square sample. Similarly $(\partial\Omega)_y$ is the y boundaries. The relaxation constant Γ and the conductivity σ have been set to 1 since the only effect the time domain of the sample. ξ, λ, κ, γ are taken to be their temperature independent values given in Table 4.1, where the temperature dependencies have been extracted from α and captured with τ_1 and τ_2 in Equation (4.4). The S-N boundary condition values, ζ_1 and ζ_2 are taken to be both be 0.1 and ω to be 0.025 as in [14]. The only input parameters that are varied are $\mathbf{J}_a$, $\mathbf{H}_e$, η, and η_1.

4.4 Investigation of the Effects of the Coupling Parameters on the Critical Current

For these studies non-dimensionalized units are used for all values, the non-dimensionalizations are given in Chapter 3. The time scale is non-dimensionalized and highly dependent on the relaxation parameter Γ. However, the sample size can given in terms of ξ_1 and thus has a dimensional value. The vortex evolutions are shown at various time steps to show the behavior of magnesium diboride under the model given above in this chapter. The material parameters for MgB_2 are given in 4.1 For the first example, Example 1, J_a is set rather high at 20 to see if this value exceed the critical current. The sample contains a grain boundary across the diagonal ($x = y$ line) where the anisotropy flips from the y direction to the x directions. Also $\eta = 0.8$ (strong coupling) and $\mathbf{H}_e = 1.6$ (moderate) for the 2st,50th,100th, and 400th time step. This same is approximately $15\xi_1 \times 15\xi_1$ or 200nm×200nm. The test functions are piecewise quadratic polynomials shown in Chapter 2. The mesh is 159×159 nodes. The non-material input parameters for Example 1 are shown in Table 4.2. Example 1 can be seen in Figure 4.1-4.4. Late in

Table 4.2

J_a	20
$\mathbf{H}_e$	1.6
η	0.8
η_1	0

TABLE 4.2: these are the non-material input parameters for Example 1

the evolution in Figure 4.4, most of sample is in the normal state. Due to this the sample has lost its superconducting properties, particularly for the applied current in the y direction. The applied current now feel resistance and produce Joule heat. This model is isothermal, but if the thermal effects were taken into account, the remaining non zero order parameters would quickly drop to zero from the thermal heating of the sample [11]. In Example 2, $J_a = 7.0$, while the external field and coupling constants remain

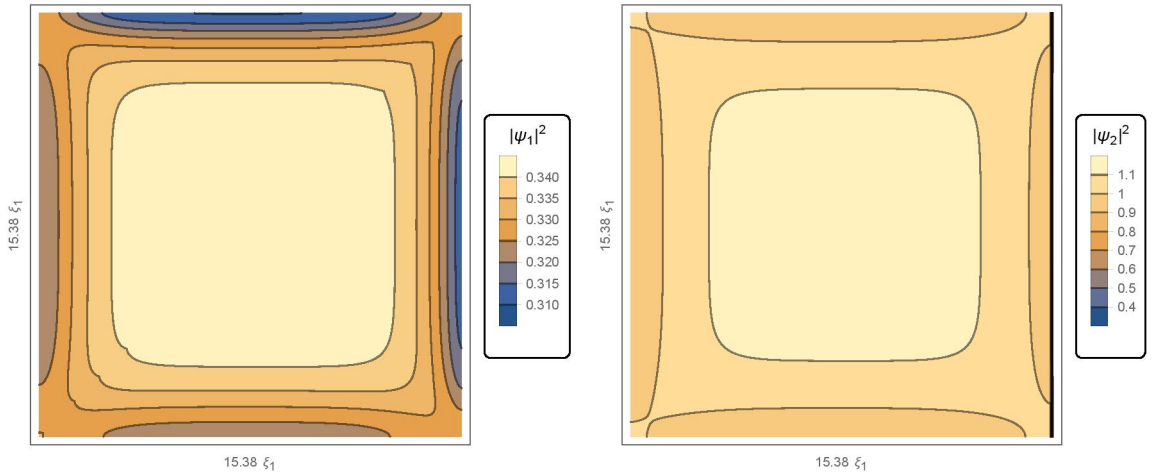

FIGURE 4.1: Example 1: ψ_1, left and ψ_2 right at the 2nd time step

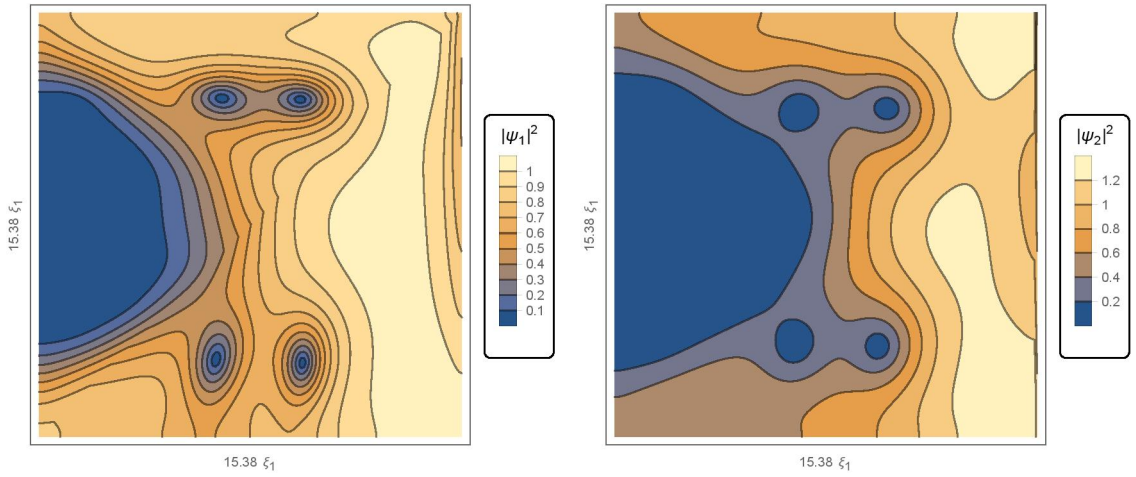

FIGURE 4.2: Example 1: ψ_1, left and ψ_2 right at 50th time step

the same as Example 1. The non-material input parameters for Example 2 are shown in Table 4.3. Example 2 can be seen in Figure 4.5-4.10. Late in the evolution, the sample still possesses superconducting properties. Though some of the sample is in the normal state, a superconducting pathway still exists for the applied current. On this pathway the order parameter value is 1 in the first band greater than 1 in the second band. This means the superconducting electron density is large in this region. This evolution was ran further than the others to ensure that superconductivity was not destroyed late in the evolution. The values that are greater than 1 in the second band occur from the

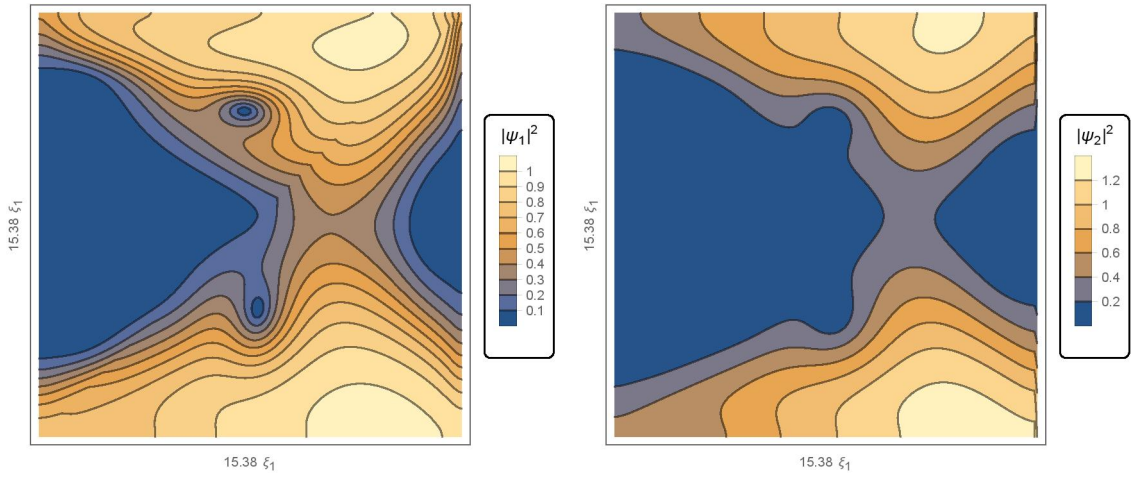

FIGURE 4.3: Example 1: ψ_1, left and ψ_2 right at the 100th time step

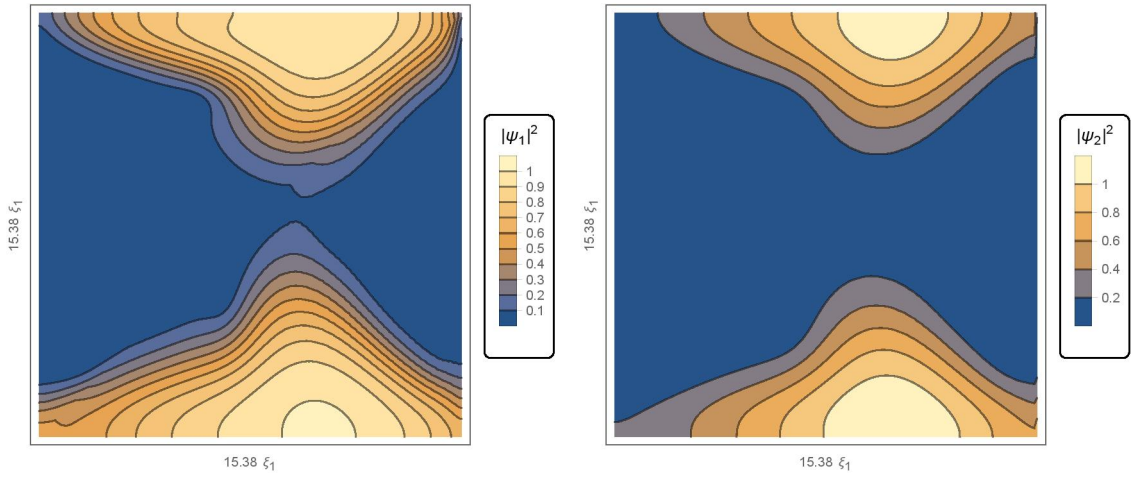

FIGURE 4.4: Example 1: ψ_1, left and ψ_2 right at the 400th time step

Table 4.3

J_a	7
$\mathbf{H}_e$	1.6
η	0.8
η_1	0

TABLE 4.3: these are the non-material input parameters for Example 2

large coupling and the large magnitude of the reduced temperature τ_2 -1.5 for $T = 31k$. In [14], $|\psi_i|_{max} \leq \sqrt{4\max\{\eta, \nu^2\eta\} + \max\{\tau_1, \tau_2\}}$, $i = 1, 2$.

In Example 3 the applied current is reduced to $J_a = 2$ and the coupling constant $\eta = 0.2$ (weak coupling). The non-material input parameters for Example 3 are shown in Table 4.4. Example 3 can be seen in Figure 4.11-4.13. We see that late in evolution superconductivity of the applied current has not been completely destroyed in the sample. The grain boundary is impeding the movement of the vorcties and normal sites, but the superconductivity is severely diminished, as most of the order parameter values

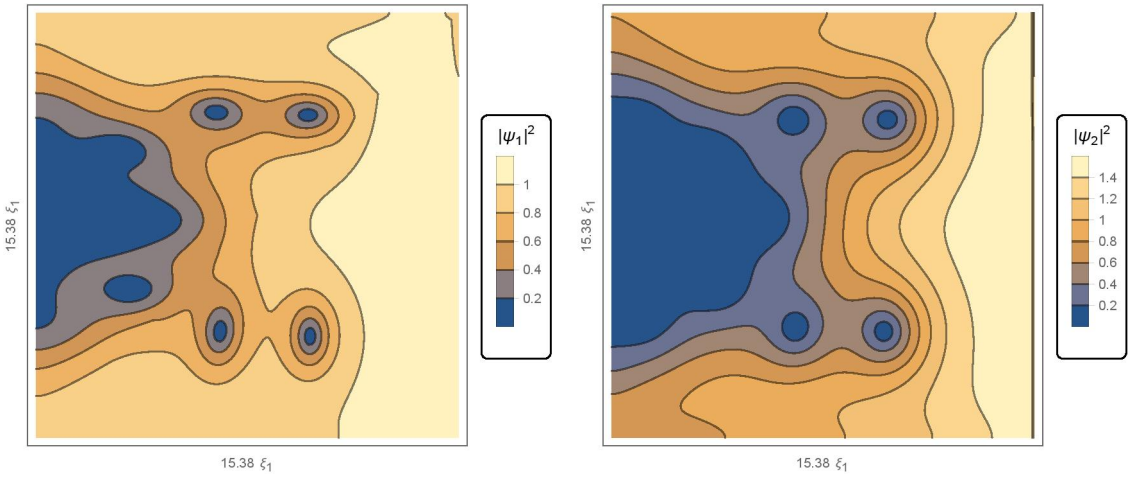

FIGURE 4.5: Example 2: ψ_1, left and ψ_2 right at the 20th time step

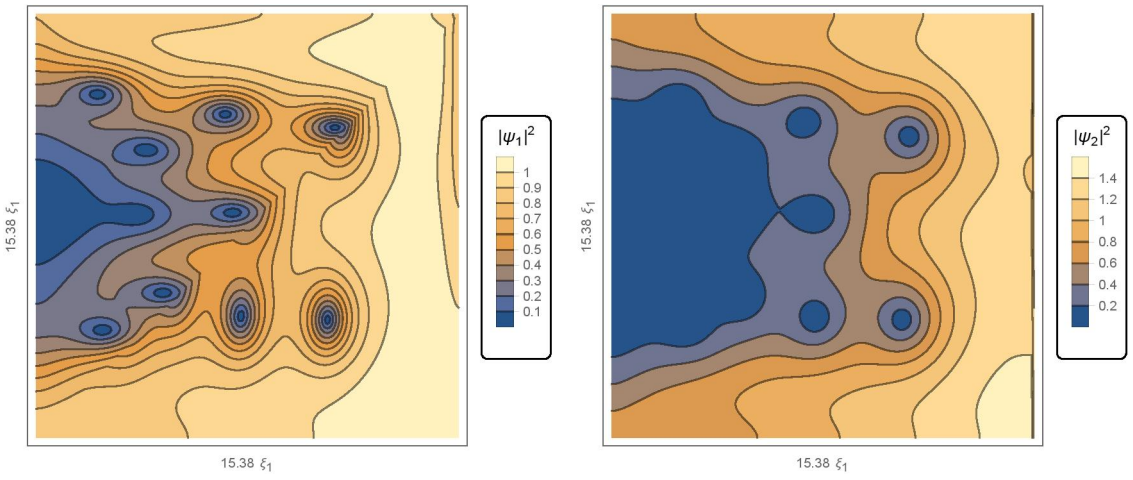

FIGURE 4.6: Example 2: ψ_1, left and ψ_2 right at the 60th time step

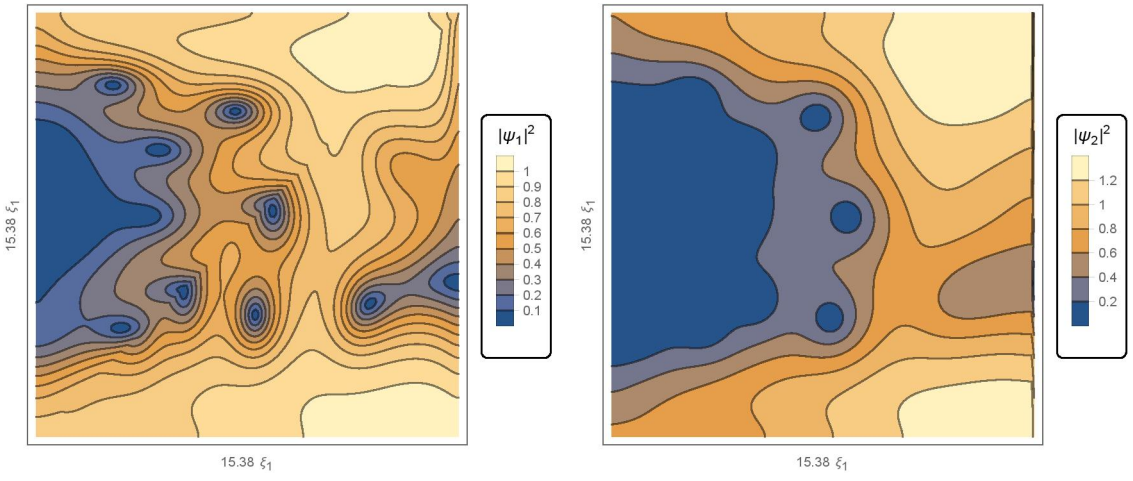

FIGURE 4.7: Example 2: ψ_1, left and ψ_2 right at the 62nd time step

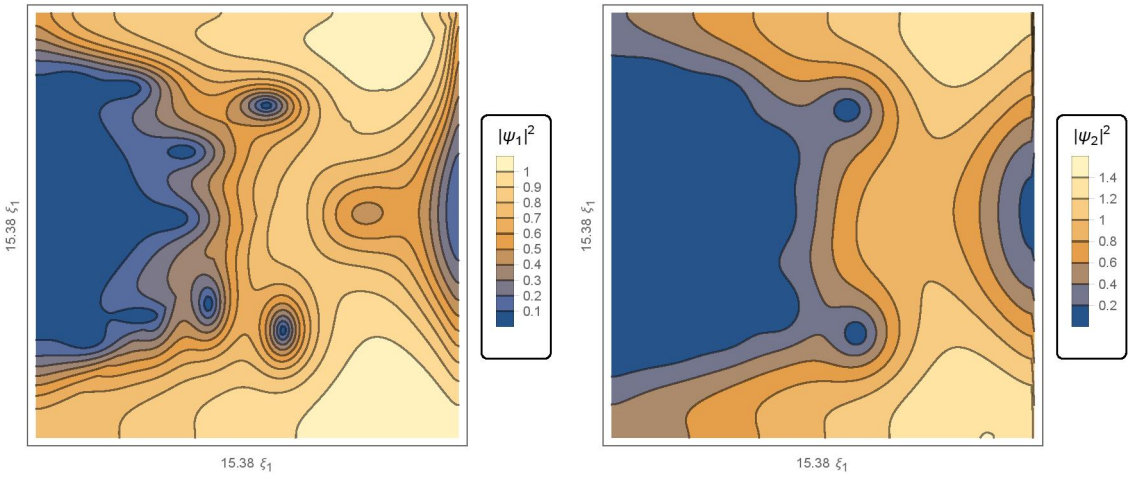

FIGURE 4.8: Example 2: ψ_1, left and ψ_2 right at 64th time step

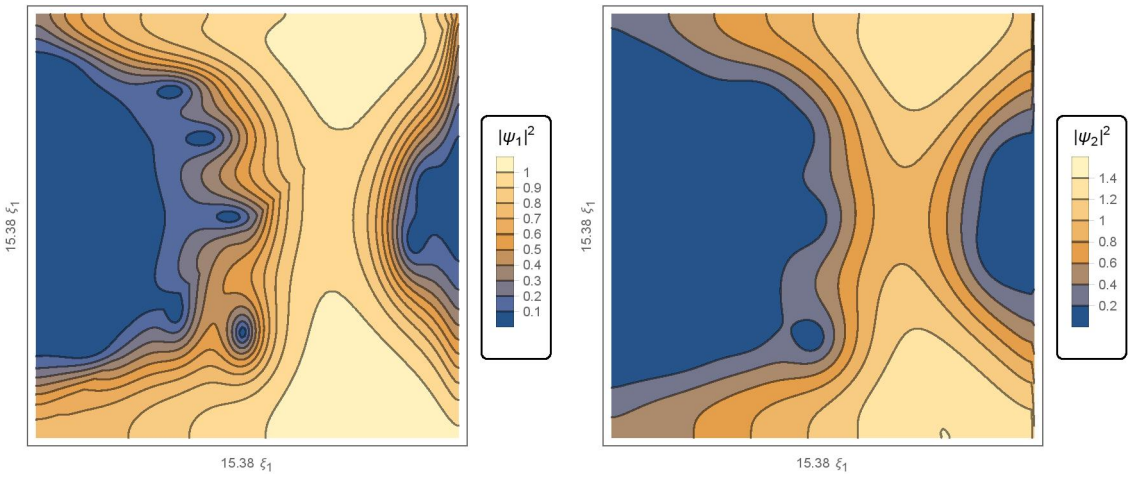

FIGURE 4.9: Example 2: ψ_1, left and ψ_2 right at the 66th time step

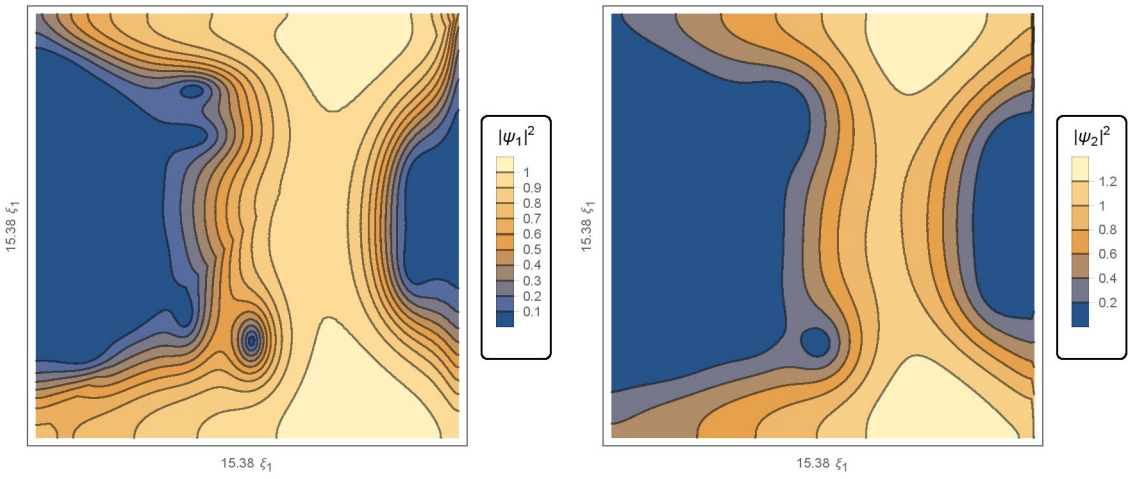

FIGURE 4.10: Example 2: ψ_1, left and ψ_2 right at the 100th time step

Table 4.4

J_a	2
$\mathbf{H}_e$	1.6
η	0.2
η_1	0

TABLE 4.4: these are the non-material input parameters for Example 3

are near 0. Still under weaker coupling, the superconductivity is destroyed faster than in Example 1.

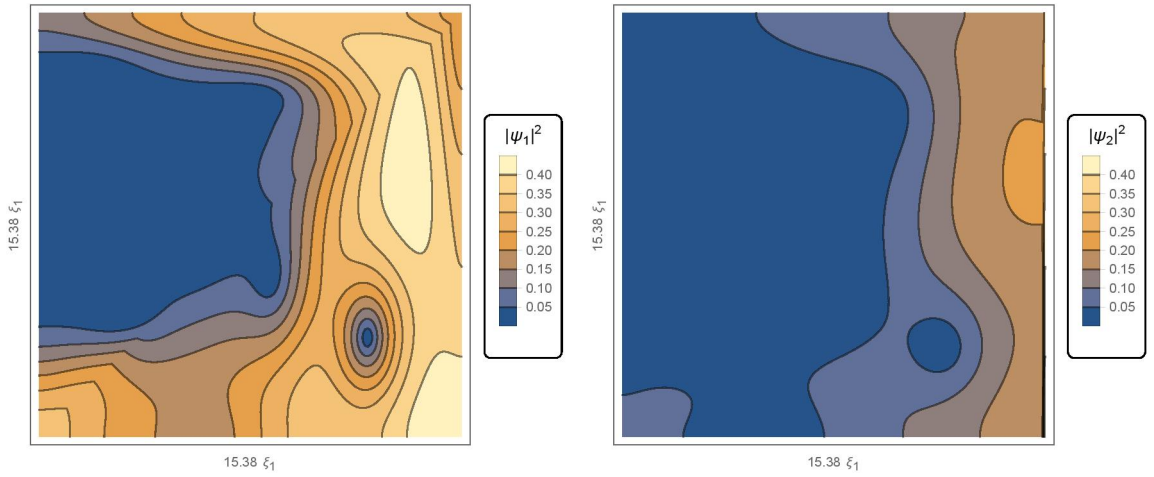

FIGURE 4.11: Example 3: ψ_1, left and ψ_2 right at the 200th time step

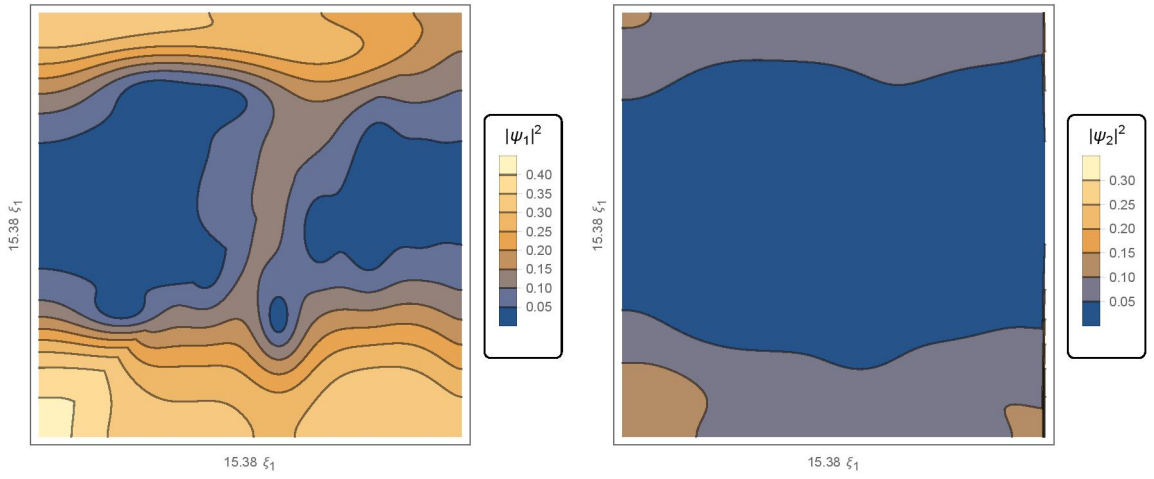

FIGURE 4.12: Example 3: ψ_1, left and ψ_2 right at the 400th time step

In Example 4, the applied current and η are kept the same as in Example 3. Now the external field is non existent $\mathbf{H}_e = 0$ and $\eta_1 = 0.2$. The non-material input parameters for Example 4 are shown in Table 4.5. Example 4 can be seen in Figure 4.14-4.20. The superconductivity is much more prevalent with the lower field. Furthermore, the inter-band coupling has increased the influence from the normally weakly interacting,

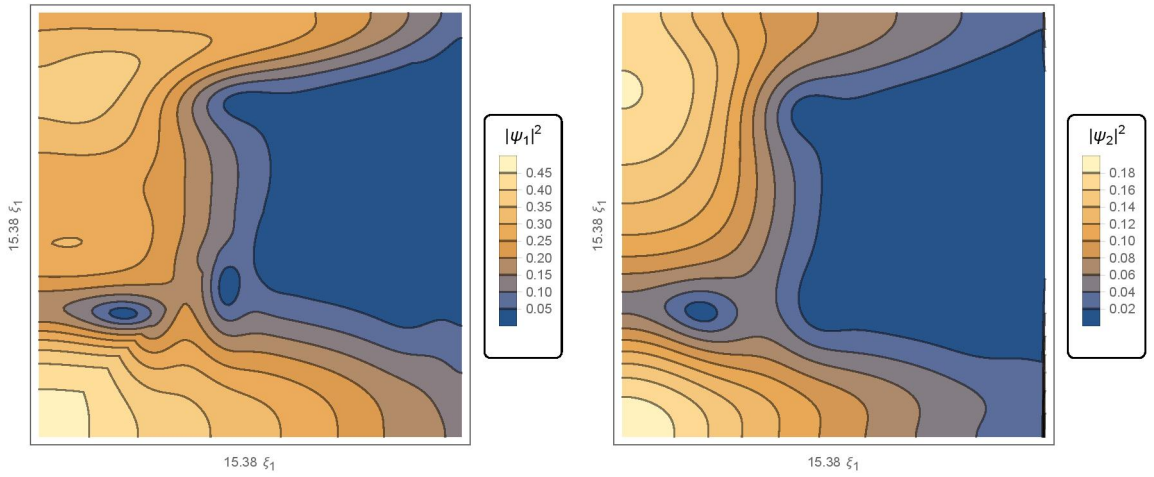

FIGURE 4.13: Example 3: ψ_1, left and ψ_2 right at the 500th time step

Table 4.5

J_a	2
$\mathbf{H}_e$	0
η	0.2
η_1	0.2

TABLE 4.5: these are the non-material input parameters for Example 4

isotropic π band. If no coupling was present, the second band would contain no vortices. This Example also demonstrates how the grain boundaries impede the movement of vortices. Shown in the 60th-66th time steps, Figures 4.15-4.18, a vortex-antivortex pair can be seen moving across the sample. One of pair crosses the grain boundary, where it meets it counter part and annihilates. Even late in the evolution the superconductivity is not destroyed, the lower magnetic field and stronger contribution from the second band have kept the vortices from combing into a large normal site on the sample.

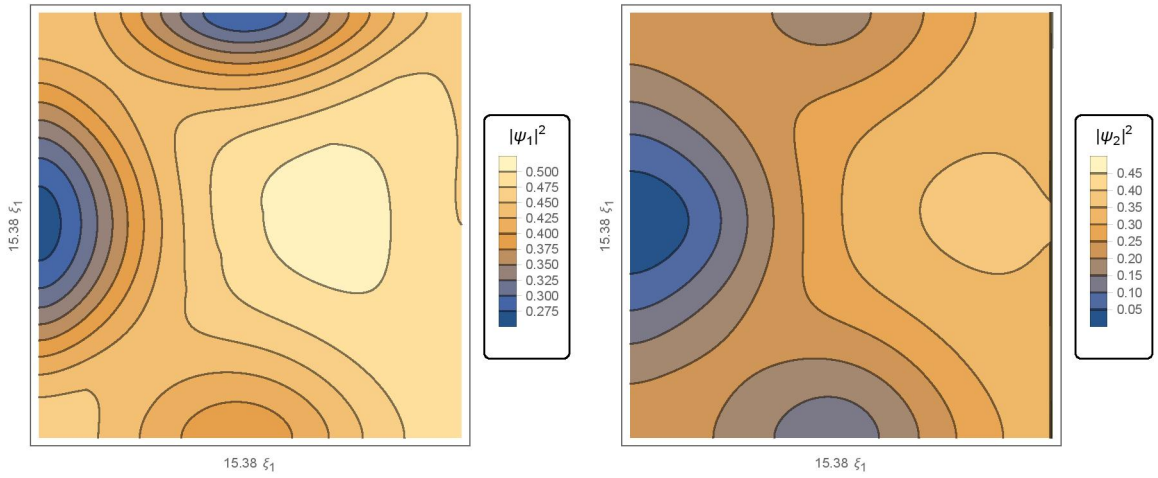

FIGURE 4.14: Example 4: ψ_1, left and ψ_2 right at the 20th time step

In Example 5 the field is $\mathbf{H}_e = 0.5$, $J_a = 2$,$\eta = 0.2$ and $\eta_1 = 0$. The non-material input

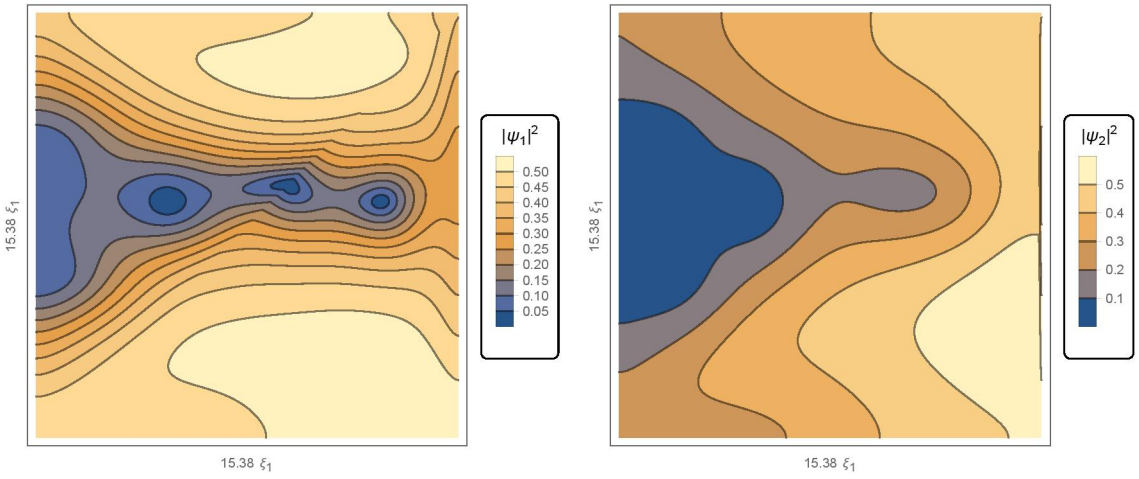

FIGURE 4.15: Example 4: ψ_1, left and ψ_2 right at the 60th time step

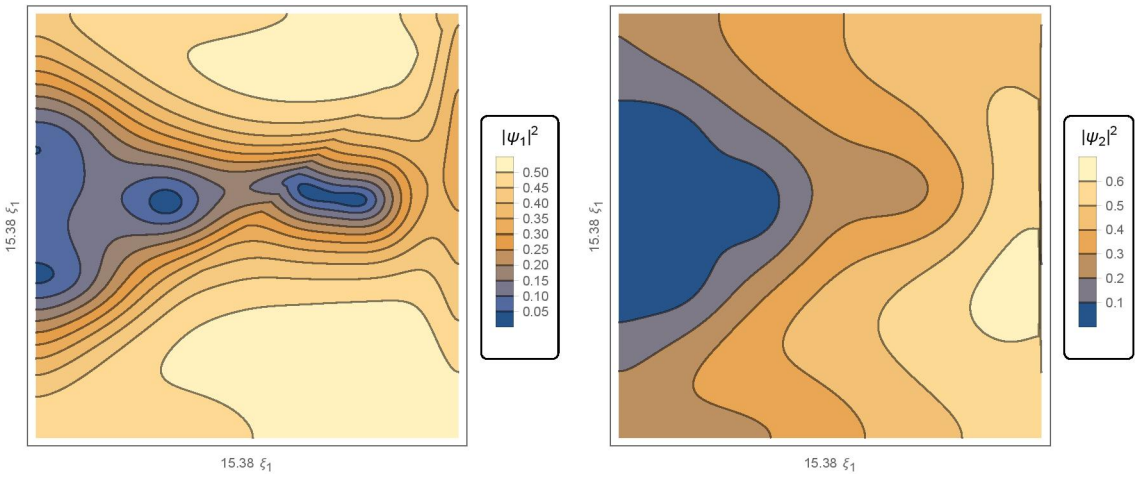

FIGURE 4.16: Example 4: ψ_1, left and ψ_2 right at the 62nd time step

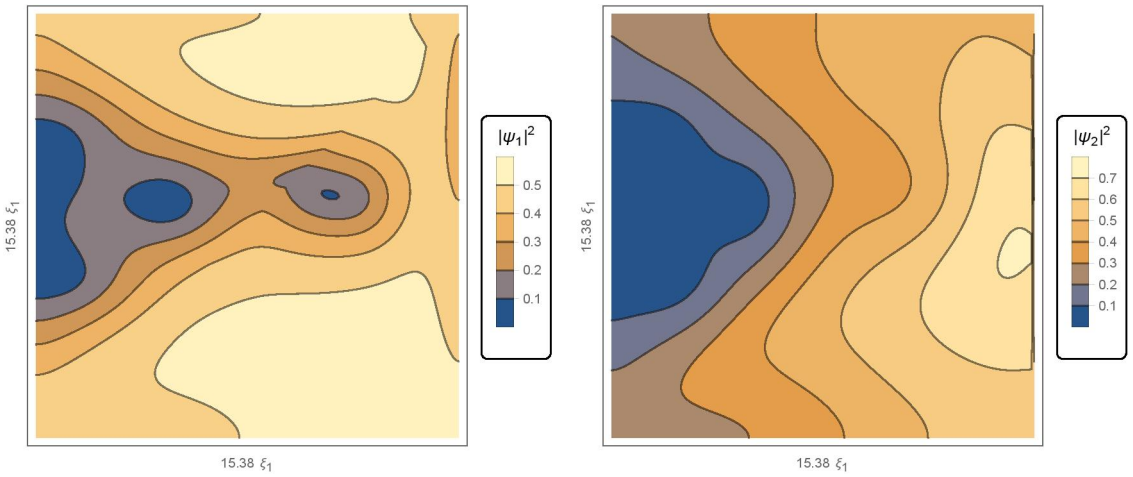

FIGURE 4.17: Example 4: ψ_1, left and ψ_2 right at 64th time step

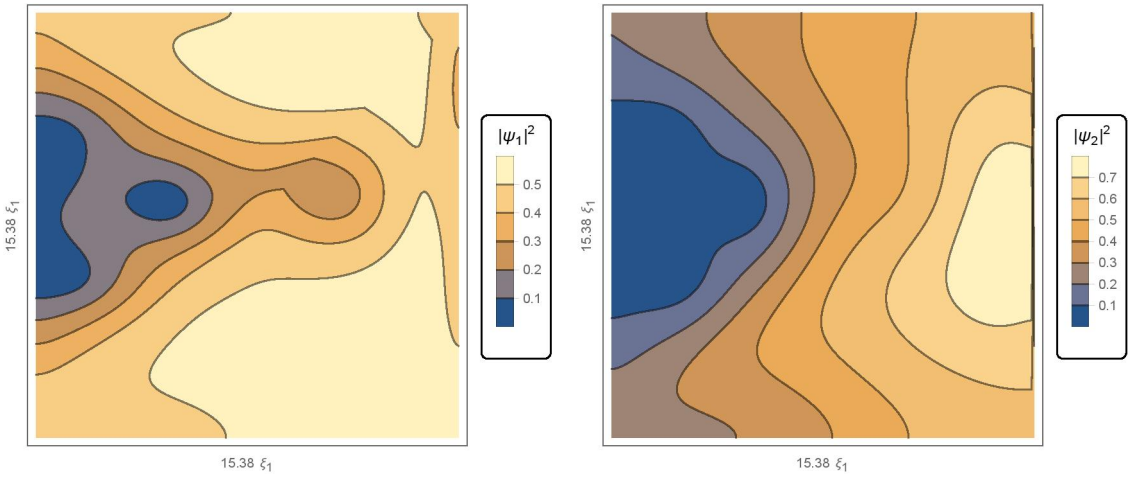

FIGURE 4.18: Example 4: ψ_1, left and ψ_2 right at the 66th time step

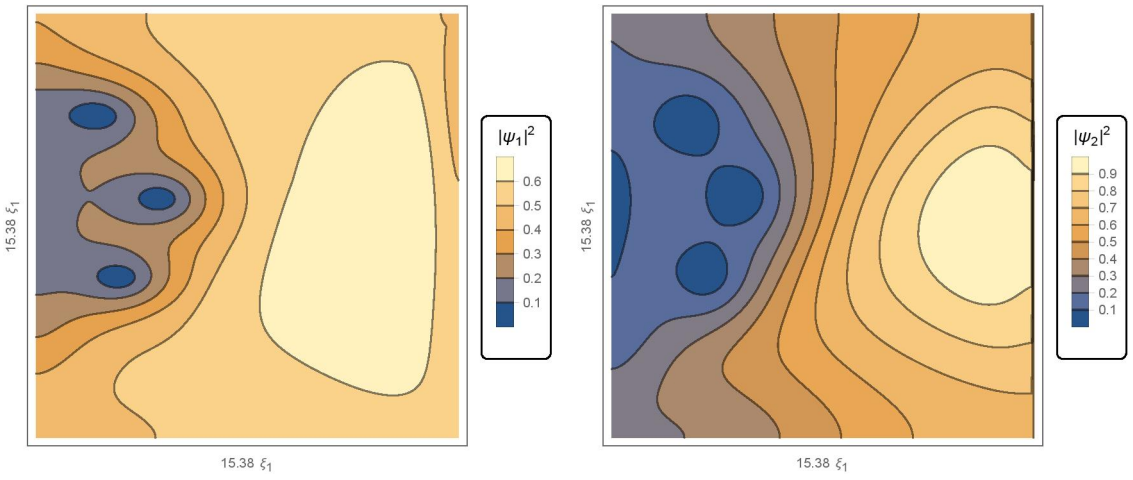

FIGURE 4.19: Example 4: ψ_1, left and ψ_2 right at the 100th time step

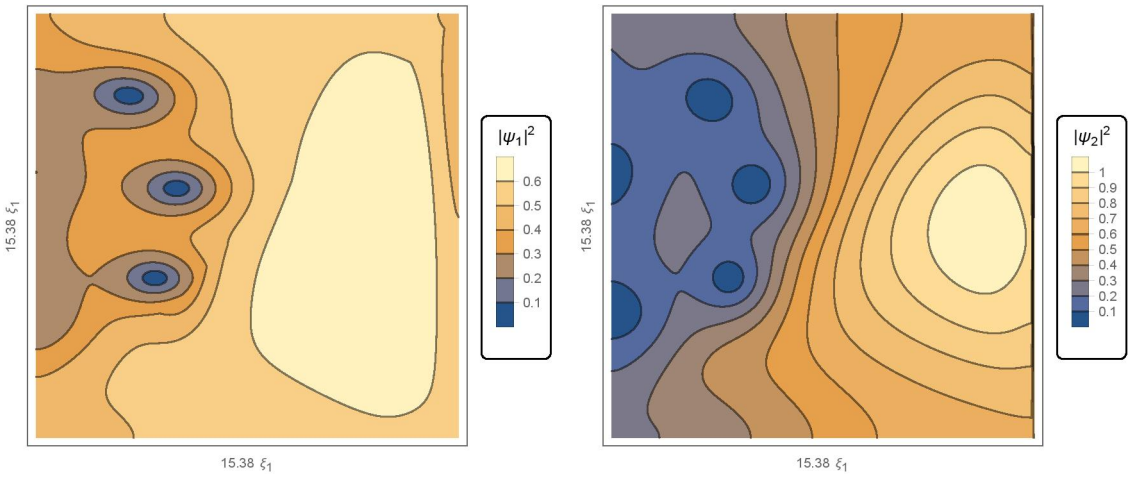

FIGURE 4.20: Example 4: ψ_1, left and ψ_2 right at the 174th time step

parameters for Example 2 are shown in Table 4.6. Example 5 can be seen in Figure

Table 4.6

J_a	2
$\mathbf{H}_e$	0.5
η	0.2
η_1	0

TABLE 4.6: these are the non-material input parameters for Example 5

4.21-4.24. In this example we see that the superconductivity is prevalent when the field is weak, given by the high values of the order parameters which are proportional the number of superconducting electrons. Furthermore, the vortices are easier to impede and pin as seen at time step 200. In 4.23 a vortex seen to be impeded by the grain boundary. Though at later times the vortex is not longer pinned to the grain boundary.

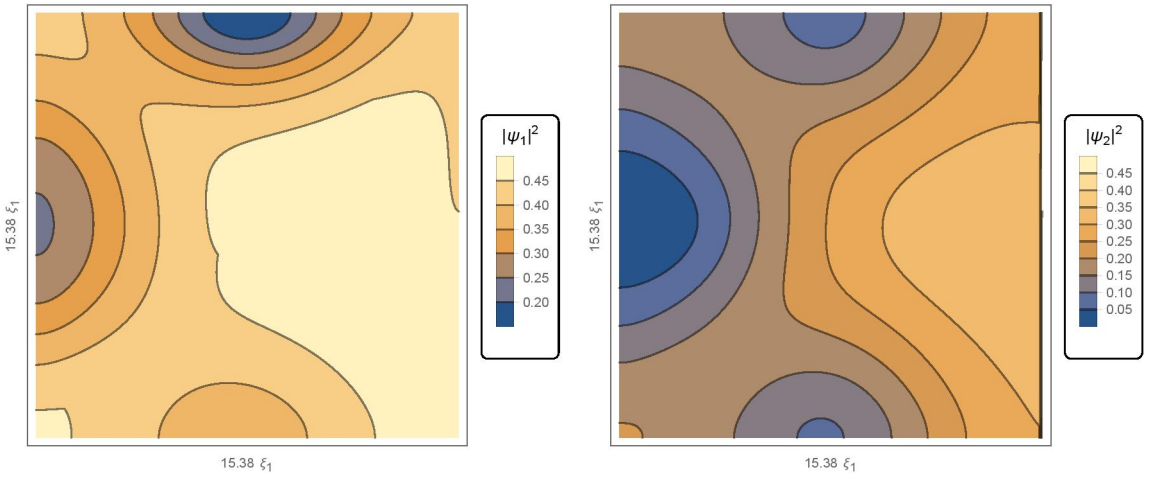

FIGURE 4.21: Example 5: ψ_1, left and ψ_2 right at the 20th time step

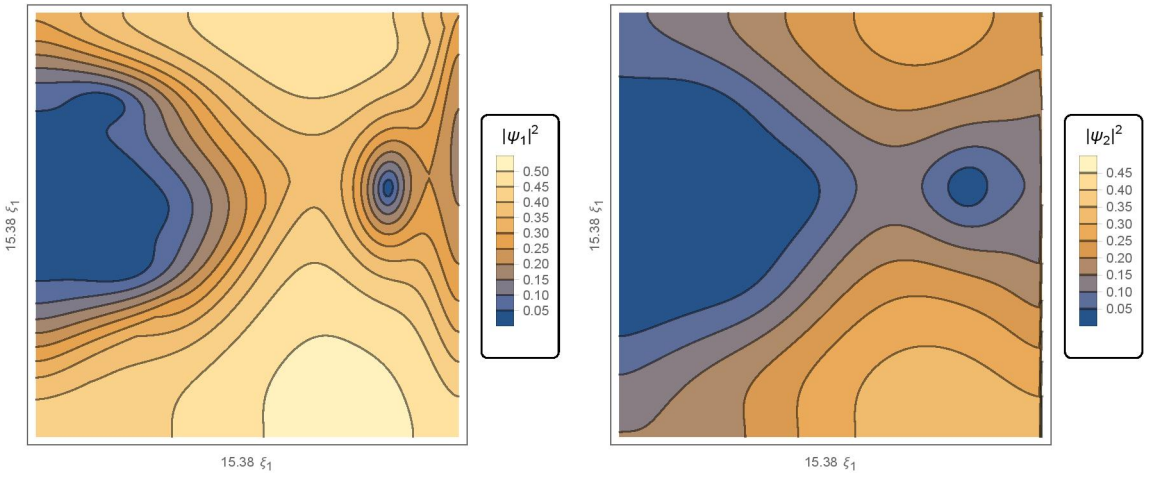

FIGURE 4.22: Example 5: ψ_1, left and ψ_2 right at the 100th time step

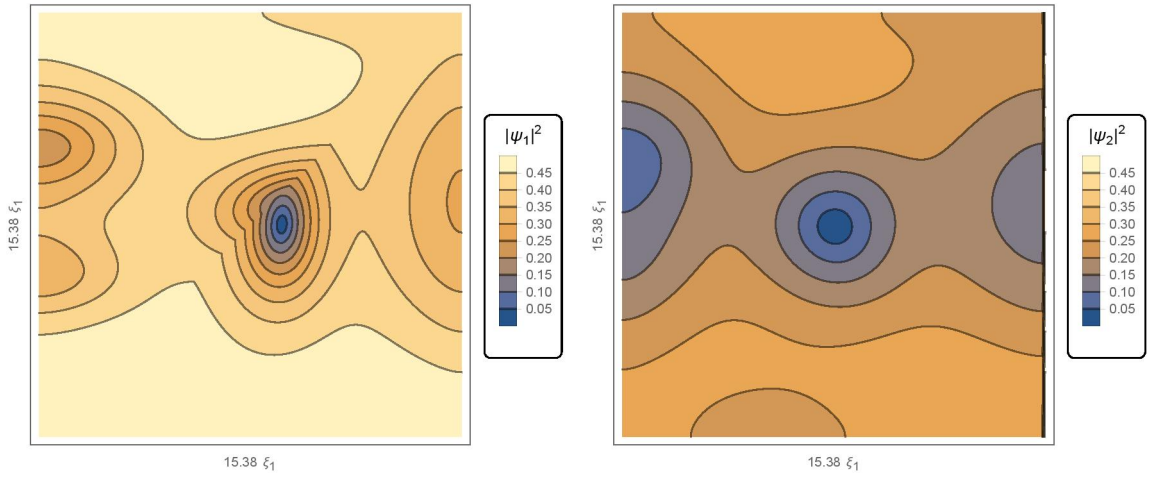

FIGURE 4.23: Example 5: ψ_1, left and ψ_2 right at the 200th time step

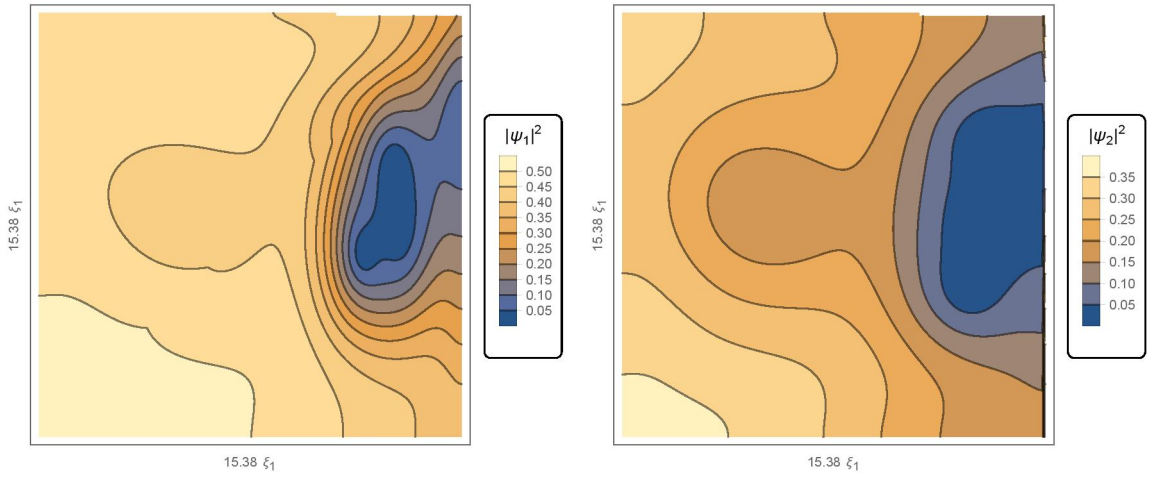

FIGURE 4.24: Example 5.4: ψ_1, left and ψ_2 right at the 328th time step

From our five numerical examples we can make some predictions about how the coupling constants effect the superconductivity in a sample with an applied current. In Example 1 with high current and high coupling, the superconductivity was completely destroyed after the sample evolved long enough. However at the same field and coupling the sample showed strong superconducting effects at J_a=7. Though the sample did have a large normal site on it, the strong coupling gave large ψ values where the superconducting properties persisted. With the ψ values near their maximum, this means that most of the electrons in this region are experiencing very little to no resistance. In Example 3 the coupling constant $\eta = 0.2$ and $J_a = 2.0$. Even though the current severely reduced, the sample was almost completely covered with a normal site ($\psi = 0$). The area that still experienced superconducting effects had lower order parameter values (< 0.5 for the σ band and $< .18$ in the π band.) In Example 4 the field was reduced to $\mathbf{H}_e = 0$ and $\eta_1 = 0.2$. This example shows how the vortex motion is impeded by the grain boundary, the field was lowered to weak the pinning force needed, but the vortex

was still unpinned late in the evolution. Normally when $\eta_1 = 0$, larger η values are need to create this vortex-antivortex behavior seen [14]. However only small η values combined with small η_1 values are needed to create this behavior. In Example 5, the field is low $\mathbf{H}_e = 0.5$ as well as thee coupling $\eta = 0.2$ and $\eta_1 = 0$. The lowered field has increased the superconductivity in the sample when compared to larger fields. However the superconducting regions are still weak with order parameter values less than 0.5. Though this sample shows superconducting properties, the applied current would experience a large resistance.

From Example 2, we see that the large coupling increases the superconductivity in the sample, though the strong field creates large normal sites. In Examples 4 and 5 where the field is reduced, the large normal sites do not appear, but the superconductivity is still weak, shown by small order parameter values. The effects of pinning can also be seen in Examples 4 and 5 where the field is weaker. This is due to the smaller pinning force $\mathbf{J}_p = \mathbf{J}_a \times \mathbf{H}_e$ need to pin the vortex. From these results, a prediction can be made on how the coupling parameter, η effects the critical current. If the Josephson-like coupling can be increased between the bands in MgB_2, the critical current can be increased. This is due to the stronger influence of the π band. If the coupling was weak or non existent, the second band would be a strictly Type I superconductor and no vortices would be seen in the samples. However the coupling keeps the band from loosing its superconducting effects, even past it's critical field ($\mathbf{H}_e$ κ_2), and above its critical temperature. Thus the optimized critical current for a clean sample of magnesium diboride in this model can be found for strong Josephson coupling effects and small external fields.

To summarize, a model was derived to describe magnesium diboride. The material parameters are given in 4.1. These and the parameters used for Examples 1-5 were the input parameters of the model. In Example 1, the destruction of superconductivity was shown with a large normal site ($|\psi_1|^2$ and $|\psi_2|^2 \to 0$) for a high applied current. Comparing Example 2 to Example 3, the increase in the coupling parameter η is seen to improve superconductivity, by the higher $|\psi_1|^2$ and $|\psi_1|^2$ values. This shows the Josephson-like coupling and the π band play an important role in increasing the critical current. In Example 4 a vortex-antivortex pair can be seen to annihilating each other. This example also shows the grain boundary impeding the movement of the vortices. Example 5 had the same parameters as Example 2, which gave poor superconductivity, except that applied field was weakened. Example 5 showed that lowering the applied field also improves the superconductivity as expected.

Bibliography

[1] Paul A. Tipler and Ralph A. Llewellyn. *Modern Physics, Fifth Edition.* W.H. Freeman and Company, New York, New York, 2008.

[2] K.-H. Hoffmann and Q. Tang. *Ginzburg-Landau Phase Transitions Theory and Superconductivity.* Springer Basel AG, 2000.

[3] Lev Petrovich Gorkov. Microscopic derivation of the ginzburg-landau equations in the theory of superconductivity. *Sov. Phys. JETP*, 9(6):1364–1367, 1959.

[4] Q. Du, M. Gunzburger, and J. Peterson. Analysis and approximation of the ginzburg–landau model of superconductivity. *SIAM Review*, 34(1):54–81, 1992. doi: 10.1137/1034003. URL http://dx.doi.org/10.1137/1034003.

[5] Q. Du, M. D. Gunzburger, and J. S. Peterson. Solving the ginzburg-landau equations by finite-element methods. *Phys. Rev. B*, 46:9027–9034, Oct 1992. doi: 10.1103/PhysRevB.46.9027. URL http://link.aps.org/doi/10.1103/PhysRevB.46.9027.

[6] Qiang Du. Global existence and uniqueness of solutions of the time-dependent ginzburg-landau model for superconductivity. *Applicable Analysis*, 53(1-2):1–17, 1994. doi: 10.1080/00036819408840240. URL http://www.tandfonline.com/doi/abs/10.1080/00036819408840240.

[7] Q. Du. Finite element methods for the time-dependent ginzburg-landau model of superconductivity. *Computers & Mathematics with Applications*, 27(12):119 – 133, 1994. ISSN 0898-1221. doi: http://dx.doi.org/10.1016/0898-1221(94)90091-4. URL http://www.sciencedirect.com/science/article/pii/0898122194900914.

[8] Jennifer Deang. A study of inhomogeneities and anisotropies in superconductors via ginzburg-landau type models. Dissertation, Virginia Polytechnic Institute.

[9] S. Chapman, Q. Du, and M. Gunzburger. On the lawrence–doniach and anisotropic ginzburg–landau models for layered superconductors. *SIAM Journal on Applied Mathematics*, 55(1):156–174, 1995. doi: 10.1137/S0036139993256837. URL http://dx.doi.org/10.1137/S0036139993256837.

[10] S Jonathan Chapman, Qiang Du, and Max D Gunzburger. A ginzburg–landau type model of superconducting/normal junctions including josephson junctions. *European Journal of Applied Mathematics*, 6(02):97–114, 1995.

[11] Dan Phillips and Eunjee Shin. On the analysis of a non-isothermal model for superconductivity. *European Journal of Applied Mathematics*, 15(02):147–179, 2004.

[12] Zhiming Chen and K-H Hoffmann. Global classical solutions to a non-isothermal dynamical ginzburg-landau model in superconductivity. *Numerical Functional Analysis and Optimization*, 18(9-10):901–920, 1997.

[13] Pierre C Hohenberg and Bertrand I Halperin. Theory of dynamic critical phenomena. *Reviews of Modern Physics*, 49(3):435, 1977.

[14] Wan-Kan Chan. *Analysis and approximation of a two-band Ginzburg-Landau model of superconductivity*. ProQuest, 2007.

[15] W. Meissner and R. Ochsenfeld. Ein neuer effekt bei eintritt der supraleitfähigkeit. *Naturwissenschaften*, 21(44):787–788, 1933. ISSN 0028-1042. doi: 10.1007/BF01504252. URL http://dx.doi.org/10.1007/BF01504252.

[16] Michael Tinkham. *Introduction to superconductivity*. Courier Dover Publications, 2012.

[17] Qiang Du. Studies of a ginzburg–landau model for d-wave superconductors. *SIAM Journal on Applied Mathematics*, 59(4):1225–1250, 1999.

[18] Yong Ren, Ji-Hai Xu, and CS Ting. Ginzburg-landau equations for mixed s+d symmetry superconductors. *Physical Review B*, 53(5):2249, 1996.

[19] SJ Chapman, Qiang Du, and MD Gunzburger. A model for variable thickness superconducting thin films. *Zeitschrift für angewandte Mathematik und Physik ZAMP*, 47(3):410–431, 1996.

[20] Qiang Du and Max D Gunzburger. A model for superconducting thin films having variable thickness. *Physica D: Nonlinear Phenomena*, 69(3):215–231, 1993.

[21] S Chapman, Q Du, M Gunzburger, and J Peterson. Simplified ginzburg–landau models for superconductivity valid for high kappa and high fields. *Adv. Math. Sci. Appl*, 5(1):193–218, 1995.

[22] Qiang Du and Paul Gray. High-kappa limits of the time-dependent ginzburg-landau model. *SIAM Journal on Applied Mathematics*, 56(4):1060–1093, 1996.

[23] Zhiming Chen, K-H Hoffmann, and Lishang Jiang. On the lawrence–doniach model for layered superconductors. *European Journal of Applied Mathematics*, 8(04):369–387, 1997.

[24] K-H Hoffmann and Jun Zou. Finite element analysis on the lawrence-doniach model for layered superconductors. *Numerical Functional Analysis and Optimization*, 18 (5-6):567–589, 1997.

[25] Qiang Du and Xiaonan Wu. Numerical solution of the three-dimensional ginzburg–landau models using artificial boundary. *SIAM journal on numerical analysis*, 36 (5):1482–1506, 1999.

[26] NV Orlova, AA Shanenko, MV Milošević, FM Peeters, AV Vagov, and VM Axt. Ginzburg-landau theory for multiband superconductors: Microscopic derivation. *Physical Review B*, 87(13):134510, 2013.

[27] Johan Carlstrom, Egor Babaev, and Martin Speight. Type-1.5 superconductivity from interband josephson coupling. In *APS Meeting Abstracts*, volume 1, page 42014, 2010.

[28] Dietrich Braess. *Finite elements: Theory, fast solvers, and applications in solid mechanics*. Cambridge University Press, 2007.

[29] R.D. Parks. *Superconductivity*. Marcel Dekker Inc., 1969.

[30] Nikolai B. Kopnin. *Theory of Nonequilibrium Superconductivity*. Oxford University Press, 2001.

[31] AV Vagov, AA Shanenko, MV Milošević, VM Axt, and FM Peeters. Extended ginzburg-landau formalism: Systematic expansion in small deviation from the critical temperature. *Physical Review B*, 85(1):014502, 2012.

[32] Thomas Dahm. Superconductivity of magnesium diboride: theoretical aspects. In *Frontiers in Superconducting Materials*, pages 983–1009. Springer, 2005.

[33] ME Zhitomirsky and V-H Dao. Ginzburg-landau theory of vortices in a multigap superconductor. *Physical Review B*, 69(5):054508, 2004.

[34] VH Dao and ME Zhitomirsky. Anisotropy of the upper critical field in mgb2: the two-gap ginzburg-landau theory. *The European Physical Journal B-Condensed Matter and Complex Systems*, 44(2):183–188, 2005.

[35] M Zehetmayer. A review of two-band superconductivity: materials and effects on the thermodynamic and reversible mixed-state properties. *Superconductor Science and Technology*, 26(4):043001, 2013.

[36] Johan Carlström, Egor Babaev, and Martin Speight. Type-1.5 superconductivity in multiband systems: Effects of interband couplings. *Physical Review B*, 83(17): 174509, 2011.

[37] A Vagov, AA Shanenko, MV Milošević, VM Axt, and FM Peeters. Two-band superconductors: Extended ginzburg-landau formalism by a systematic expansion in small deviation from the critical temperature. *Physical Review B*, 86(14):144514, 2012.

[38] Victor Moshchalkov, Mariela Menghini, Taichiro Nishio, QH Chen, AV Silhanek, Vu Hung Dao, LF Chibotaru, ND Zhigadlo, and J Karpinski. Type-1.5 superconductivity. *Physical review letters*, 102(11):117001, 2009.

[39] Michael R Koblischka, Alex Wiederhold, Miryala Muralidhar, K Inoue, Thomas Hauet, Bruno Douine, Kévin Berger, Masato Murakami, and Uwe Hartmann. Development of mgb 2-based bulk supermagnets. *Magnetics, IEEE Transactions on*, 50(11):1–4, 2014.

[40] Cristina Buzea and Tsutomu Yamashita. Review of the superconducting properties of mgb2. *Superconductor Science and Technology*, 14(11):R115, 2001.

[41] Michael Eisterer. Magnetic properties and critical currents of mgb2. *Superconductor Science and Technology*, 20(12):R47, 2007.

[42] IN Askerzade and A Gencer. London penetration depth λ (t) in two-band ginzburg–landau theory: application to mgb 2. *Solid state communications*, 123(1):63–67, 2002.

[43] EW Collings, MD Sumption, M Bhatia, MA Susner, and SD Bohnenstiehl. Prospects for improving the intrinsic and extrinsic properties of magnesium diboride superconducting strands. *Superconductor Science and Technology*, 21(10): 103001, 2008.

[44] E Martinez, P Mikheenko, M Martínez-López, A Millán, A Bevan, and JS Abell. Flux pinning force in bulk mg b 2 with variable grain size. *Physical Review B*, 75 (13):134515, 2007.

[45] PC Canfield, SL Bud'ko, and DK Finnemore. An overview of the basic physical properties of mgb 2. *Physica C: Superconductivity*, 385(1):1–7, 2003.